Paul Falthansl-Scheinecker, BSc

Approaching Fundamental Resolution Limits of Focused Electron Beam Induced Deposition During the Fabrication of Gold Nanostructures for Terahertz Plasmonics

MASTER'S THESIS

to achieve the university degree of

Diplom-Ingenieur

Master's degree programme: Technical Physics

submitted to

Graz University of Technology

Supervisor

Ass.Prof. Priv.-Doz. Dipl.-Ing. Dr. techn. Harald Plank

Institute of Electron Microscopy and Nanoanalysis

Graz, May 2018

AFFIDAVIT

I declare that I have authored this thesis independently, that I have not used other than the declared sources / resources, and that I have explicitly indicated all material which has been quoted either literally or by content from the sources used. The text document uploaded to TUGRAZonline is identical to the present master's thesis.

Date

Signature

Abstract

Focused electron beam induced deposition (FEBID) is an additive, direct writing technique that enables the fabrication of sophisticated structures in the lateral sub-20 nm regime. Since FEBID does not comprise extensive pre- and post-growth processes, it presents a fabrication technique with incomparable high flexibility regarding the structure layout. For this reason and for the capability of depositing exceedingly precise structures, FEBID is perfectly suited for plasmonic applications. Plasmonic structures have the unique ability to manipulate phase, polarization and amplitude of electromagnetic waves in dependence on the structure dimensions opening the door for novel applications like super resolving lenses.

In the course of the present thesis, we developed a blueprint for the fabrication of quasi 2D plasmonic gold structures via FEBID. As the validation of the plasmonic response was conducted within a morphological cavity, the first part of this study was addressed to precursor dynamics in the proximity of elevations framing the patterning area. By evaluating atomic force microscopy height images of the deposits, a significant increase of vertical growth rates accompanied with a slight decrease of the structure widths could be revealed. Detailed analyses reveal, that the operation point was successfully shifted close to the highly desired reaction rate limited regime, where FEBID reaches its ultimate resolution. Furthermore, an unexpectedly strong lateral gradient of precursor molecules has been found close to the cavity corners, which might give first indications of a multilayer coverage.

Based on the insights into adsorbate kinetics within a cavity, we were able to create advanced patterning strategies resulting in exceedingly homogenous large-scale nano-pill arrays with height variation of ± rel. 2 %. Besides the satisfying in-field homogeneity, the dimensions of the pills showed astonishing values of 14 nm FWHM at a height of 21 nm representing a benchmark in the FEBID community. Since FEBID structures contain high content of carbon after deposition, a post-growth purification process was conducted resulting in highly pure metallic structures, which are inevitable for plasmonic applications. The successful transformation into pure gold pills together with the accurate array fabrication could be eventually verified via optical measurements.

Kurzfassung

Das additive Abscheideverfahren FEBID (Focused Electron Beam Induced Depositon) ist eine Direkt-Schreibtechnologie, welche es ermöglicht, komplexe Strukturen im lateralen Sub-20 nm Bereich zu fabrizieren. Die Abscheidung wird durch einen fokussierten Elektronenstrahl induziert und erfordert keine aufwendigen Prozessschritte vor und nach der Abscheidung, was eine hohe Variabilität bezüglich des Strukturdesigns ermöglicht. Aufgrund der außerordentlichen Flexibilität und der hohen Präzision eignet sich FEBID ideal für die Fabrikation von plasmonischen Strukturen, welche die einzigartige Eigenschaft haben, Phase, Polarisation und Amplitude elektromagnetischer Wellen in Abhängigkeit der Strukturgeometrie zu manipulieren. Diese Eigenschaft bereitet den Weg für bahnbrechende Anwendungen wie zum Beispiel Linsen mit einer Auflösung im Sub-Wellenlängen Bereich.

Im Zuge dieser Masterarbeit entwickelten wir eine Anleitung zur Fabrikation von quasi-zweidimensionalen plasmonischen Goldstrukturen via FEBID. Da die Validierung der plasmonischen Eigenschaften innerhalb einer morphologischen Kavität durchgeführt wurde, wurde zuvor der Einfluss einer Kavität auf die Precursor-Dynamik untersucht. Mit Hilfe von Atomkraftmikroskopie Messungen konnte eine deutliche Erhöhung der vertikalen Abscheiderate und einer gleichzeitigen Reduktion der lateralen Abscheiderate innerhalb der Kavität beobachtet werden. Die detaillierte Datenanalyse zeigte, dass der Operationspunkt nahe an elektronenlimitierte Bedingungen geschoben werden konnte, in welchen FEBID seine ultimative Auflösung erreicht. Darüber hinaus konnte in den Kavitätsecken ein unerwartet starker, lateraler Gradient der Precursor Bedeckung nachgewiesen werden, welcher erstmals auf Multilagen Bedeckungen hinweisen könnte.

Durch die fundierten Erkenntnisse der Precursor-Kinetik konnten wir im zweiten Teil dieser Arbeit Strukturierungsschemata entwickeln, welche die Fabrikation von großflächigen Arrays mit einer äußert homogenen Höhenverteilung (± rel. 2 %.) ermöglichten. Die einzelnen Nanostrukturen offenbarten eine Halbwertsbreite von 14 nm bei einer Höhe von 21 nm. Diese beachtlichen Werte stellen einen Benchmark für hochauflösende Nanostrukturierung mittels FEBID dar. Aufgrund des hohen Kohlenstoffanteils der Abscheidungen wurde ein Prozessschritt zur Aufreinigung der Materialien durchgeführt, welcher zu rein metallischen Strukturen führte. Dieser Schritt war unerlässlich, da plasmonische Resonanzen eine hohe Leitfähigkeit erfordern. Die erfolgreiche Durchführung des finalen Prozessschritts sowie die akkurate Fabrikation der Nanostrukturen konnte abschließend durch optische Messungen verifiziert werden.

Acknowledgements

I want to sincerely thank all persons who supported me during this thesis. At first, I want to express my gratitude to Prof. Ferdinand Hofer, the head of our institute, who provided the opportunity to write this thesis.

A special thank goes to Prof. Harald Plank, who supported me, challenged me and most importantly inspired me for working scientifically with a special view on the small details. With his enthusiastic and passionate character, he constantly fuelled my great interest in further exploring fundamental physical effects.

I greatly appreciate Dr. Robert Winkler, my co-supervisor, who shared his extraordinary knowledge by instructing me thoroughly on the dual beam microscope. Moreover, his scientific and personal advises made a precious contribution throughout the whole time at FELMI-ZFE.

My gratitude also goes to DI Ulrich Radeschnig for sharing his data, instructing me on the atomic force microscope and for sometimes interrupting the work with exciting conversations about non-scientific topics. As well, my thank goes to the whole FELMI team, who makes the institute a warm and comfortable place and a great environment to work.

I want to sincerely thank my wonderful girlfriend, Magdalena, who always supports me with her love, her advises and her encouraging words, especially in the final months, which were occasionally very challenging. I also want to thank my sincere friend, Paul, for providing valuable scientific advises as well as for always supporting and motivating me.

At last, I want to thank my whole family for their permanent support, patience and unconditional love. Especially my parents, Josef and Karin, who always support and encourage me with inspiring ideas and thoughts – thank you for always being there for me.

Table of Contents

1 Motivation and Introduction 7
2 Instrumentation 8
2.1 Dual Beam Microscope 8
2.1.1 Scanning Electron Microscopy 9
2.1.2 Setup of an Electron Column 10
2.1.3 Interaction of Electrons with Solids and Detecting Systems 11
2.2 Focused Electron Beam Induced Deposition 13
2.2.1 Basic Concept 13
2.2.2 Dissociation Mechanisms for Precursor Molecules 14
2.2.3 Continuum Model 16
2.2.4 Working Regime 17
2.3 Purification Process 17
2.3.1 Environmental Scanning Electron Microscope 18
2.3.2 Low Temperature Purification in Aqueous Environment 19
2.4 Plasmonics 20
2.5 Atomic Force Microscopy 20
3 Related Previous Work 25
3.1 Fabrication of Plasmonic Gold Nanostructures 25
3.2 Predictable Downscaling of Gold Nanostructures 27
4 Experiments and Results 30
4.1 Influence of a Morphological Cavity on Au Depositions 32
4.1.1 Deposition Behaviour Inside a Morphological Cavity 33
4.1.2 Lateral Precursor Coverage Gradient 35
4.1.3 Boosting the Local Precursor Coverage 38
4.1.4 Summary: Influence of a Morphological Cavity 40
4.2 Plasmonic Pill Arrays 41
4.2.1 Single Pills 43
4.2.2 Pills in a Line Array 45
4.2.3 Characterization and Prevention of Residual Depositions 47
4.2.4 Optimized Pills in a Line-Array 50
4.2.5 Pills Arranged in Block Arrays 52
4.2.6 Line per Line Patterning for Large-Scale Arrays 55

4.2.7 Achievable Feature Size 57
4.2.8 Pill Array Purification 59
4.2.9 Plasmonic Response 60
5 Summary and Outlook 63

List of Abbreviations

AE	….	auger electron	LLE	…..	low-loss electron
AFM	….	atomic force microscopy	LSPR	…..	localized surface plasmon resonance
BSE	….	backscattered electron	MTL	…..	mass transport limited
DBM	….	dual beam microscope	PE	…..	primary electron
DE	….	diffusion-enhanced	PoP	…..	point pitch
DT	….	dwell time	PSD	…..	positioning sensing detector
EDXS	….	energy dispersive X-ray spectroscopy	RRL	…..	reaction rate limited
ESEM	….	environmental scanning electron microscope	RT	…..	refreshtime
ETD	….	Everhart-Thornley detector	SE	…..	secondary electron
FEBID	….	focused electron beam induced deposition	S-TET	…..	specific total exposure time
FIBID	….	focused ion beam induced deposition	TEM	…..	transmission electron microscopy
FWHM	….	full width at half maximum	TET	…..	total exposure time
GIS	….	gas injection system	TLD	…..	through-the-lens detector
ITO	….	indium tin oxide			

1 Motivation and Introduction

The advances in nanofabrication during the last decades have been extraordinary, mainly driven by the electronic industry to meet the outraging demands of computing power. A novel and highly exciting method is analogue optical computing, which is based on plasmonic surfaces performing mathematical operations when illuminated by electromagnetic waves.[1,2] This recent research promises high-throughput and low-power consumption operation of analogue computers for specific computational tasks.[3] Generally, the flourishing science of plasmonic can be explained by the ability of fully manipulating phase, polarization and amplitude of electromagnetic waves[4], which opens the door to ground-breaking applications like super-resolution imaging[5] or invisibility cloaks[6].

Currently, our working group follows the unprecedented approach of fabricating plasmonic devices directly on the outlet of a light fibre allowing sub wavelength resolved Raman[7] spectroscopy. The plasmonic structures are produced via focused electron beam induced deposition (FEBID), a direct write technique that enables the fabrication of structures in the 10 nm range[8] on virtually any given morphology. Since FEBID does not comprise process steps involving masks or photoresists, it presents a fabrication technique with incomparable high flexibility regarding the structure layout. Thus, it is perfectly suited for prototyping plasmonic devices.

However, FEBID structures usually contain a very high carbon content of about 90 at. % after deposition.[9] Since plasmonic devices necessitate high conductivity for sufficient propagation of plasma waves, a post deposition purification step has to be conducted. Introduced by Geier et al.[10] the purification step results in highly pure metallic structures (platinum, gold) for which plasmonic resonances could be successfully verified.[11]

In this thesis, we will focus on establishing a blueprint for the fabrication of quasi 2D plasmonic structures in the nanoscale range. As a pre-step towards sophisticated integrated devices, we will fabricate filters in the optical range on test substrates. The single elements, which will be subsequently placed in large-scale arrays, have exceedingly small dimensions in the sub-20 nm range. In terms of fabrication accuracy, homogenously deposited structures throughout the whole array represent a major challenge. Therefore, we have to determine the distribution of the FEBID precursor molecules in the patterning area. The complex dynamic process of precursor adsorption can be strongly influenced by morphological obstacles in the proximity of the patterning spots. Since, the deposition was conducted inside a morphological cavity, the first part of this thesis was addressed to the determination of the precursor dynamics. Following this, we will develop and implement sophisticated patterning strategy for large-scale arrays of high fidelity nanostructures.

2 Instrumentation

2.1 Dual Beam Microscope

A dual beam microscope (DBM) incorporates a scanning electron microscope (SEM) and a focused ion beam (FIB) in a single device. This combination is a very powerful analysis and structuring instrument in which the ion beam can be used for processes such as sputtering, ion implantation and etching with the option of simultaneous non-destructive imaging with the SEM.[12]

The FIB at our institute is supplied with Gallium ions, which are generated by a liquid metal ion source. Most frequently the FIB is used for the preparation of transmission electron microscope (TEM) lamellas with the lift-out technique. With this technique the area of interest is cut out of the bulk material, mounted on a TEM grid and thinned by grazing ion bombardment until an electron transparent membrane is achieved.[13]

Generally, the SEM is applied in almost every scientific field such as biology, medicine and material science for high resolution imaging without the need of extensive sample preparation. Furthermore, it is a widely used analysis tool for determining material compositions and properties.[14]

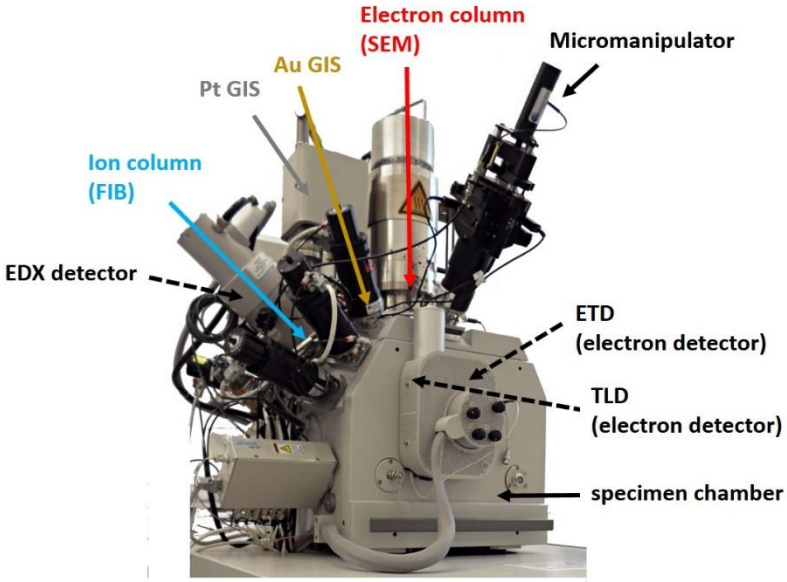

Figure 1: Dual beam microscope at the FELMI-ZFE (FIB Nova 200, Thermo Scientific Fisher). The electron column is illustrated in red, the ion column in blue. The columns are tilted 52° to each other. There are several available detectors for different interaction signals with the sample: ETD (electron signal), TLD (electron signal), EDX detector (x-ray signal). In order to generate a sufficient vacuum in the columns as well as in the specimen chamber, a roughing pump, a turbomolecular pump and an ion getter pump are utilized. The precursor molecules for the Gold depositions, which were performed during this thesis, were provided by the Au custom gas injection system (GIS) marked by the gold arrow.[15]

The DBM used in this thesis is additionally equipped with gas injection systems (GIS), which are generating a gas flux of functional molecules for the deposition of material and for selective etching.

If the deposition is induced by impinging ions, one speaks of focused ion beam induced deposition (FIBID), in case of electrons as the deposition activator it is called focused electron beam induced deposition (FEBID). FEBID has the great advantage that no ion implantation and no sputtering takes place. Moreover, the fabrication accuracy is better and the heating of the sample is lower compared to FIBID. That`s why the fabrication of novel plasmonic Au-structures in the course of this thesis was conducted via FEBID.

A requirement for DBM operation is the presence of high vacuum, which is sufficient for the generation of the electron and ion beam. Moreover the high vacuum is necessary since scattering of electrons and ions at gas molecules inside the chamber has to be avoided in order to achieve an adequate image contrast.[16] The ultrahigh vacuum in the electron and ion column, respectively, is generated by ion getter pumps. For the initial vacuum inside the specimen chamber roughing pumps are used followed by turbomolecular pumps for achieving the operating condition.

2.1.1 Scanning Electron Microscopy

The basic principles of optics, which state that the resolution is limited by the wavelength of the imaging beam, is also valid for electron microscopy. Whereas the optical wavelength is fixed by the light source, the wavelength of particles and hence also of electrons can be altered in dependence of the particle speed. The correlation between the wavelength and the particle speed, which is determined by the acceleration voltage, was first discovered by De-Broglie[17]:

$$\boldsymbol{\lambda} = \frac{\boldsymbol{h}}{\sqrt{\boldsymbol{2qmU}}}$$

with the wavelength λ, the relativistically corrected mass m, the acceleration voltage U and the Planck constant h. Typically, the acceleration voltage for a SEM is between 1-30 kV. In terms of wavelength for an electron this means 0.07 Å for 30 kV compared to optical wavelengths, which are approximately higher by a factor of 100 000. The theoretical resolution limitation is defined by the Rayleigh criterion[18]:

$$\boldsymbol{\delta} = \frac{\boldsymbol{0.61\,\lambda}}{\boldsymbol{\eta\, sin(\beta)}}$$

with δ the resolution limit, η the index of refraction (1 for vacuum) and β the semi divergence angle of the impinging beam (for electron microscopy 2-5 mrad). Speaking only in terms of wavelength, the distance between two points to be resolved would be decreased for the SEM by the same factor as the wavelength reduction. However, effectively the resolution is only improved by a factor of 1 000. This can be explained by a significantly smaller practical opening angle β. The influence of lens aberration for charged particles are significantly higher than for optical lenses. Since the aberrations are increasing with increasing opening angle, the desire is to keep the angle small in order to minimize the aberrations.[16]

To observe a finely focused electron spot at the specimen surface, the beam has to be focused by electron optics, mainly magnetic lenses. By rastering line by line over a specific sample area, the SEM

image is created. Higher magnification can be achieved by attenuating the beam deflection and hence reducing the scanned frame. This is only valid if the screen size of the output device, usually a computer screen, stays constant. The magnification of a SEM can be simply expressed by the ratio of the edge length of the screen to the scanning frame:

$$\boldsymbol{M = \frac{l_s}{l_f}}$$

with the magnification M and the edge length l_s and l_f for the screen and the scanning frame, respectively.[19]

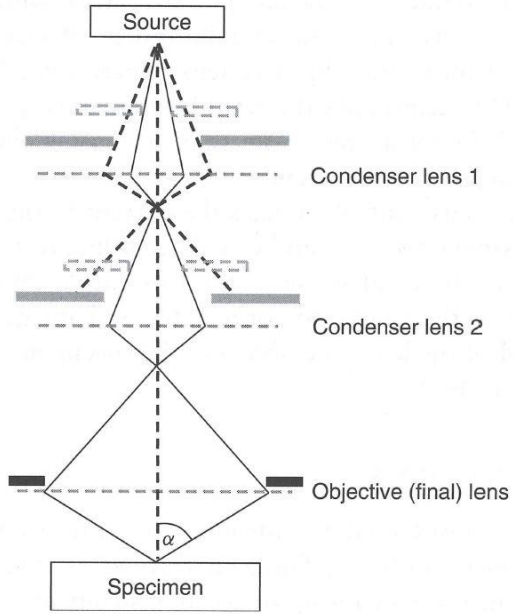

Figure 2: Scheme of a basic SEM column comprising an electron gun, condenser lenses and a final objective lens. Adjustable apertures indicated by the light grey bars are responsible for controlling the beam current and reducing the electron spread. The convergence angle α is determined by the final aperture illustrated by the dark grey bar.[21]

2.1.2 Setup of an Electron Column

As a first step towards a finely focused electron beam, the electrons have to be generated. There are three different types of electron sources, namely the thermionic emitter, the cold field emitter and the Schottky emitter. The thermionic emitter requires the lowest vacuum and provides the highest current. However, large energy spread, low brightness and short lifetime are major drawbacks. By utilizing the field emission at very fine biased tips, the cold field emitter produces an electron beam for which we observe the best resolution. The supreme beam parameters originate from the smallest beam diameter and the highest brightness. But major drawbacks such as low beam stability, limited beam current and a very high vacuum make the cold field emitter impracticable for many applications. The Schottky emitter, which is used in our DBM setup, combines high and stable beam current with

good brightness and low beam diameter. Heating of the filament and applying an electric field make the electrons overcome the reduced work function of 2.7 eV, which is induced by the ZrO coating[20].[14]

The electrons from the source are accelerated towards the sample and pass through a lens and aperture system on the way to the specimen surface. In Figure 2 a basic setup of a SEM column is depicted, which comprises the electron gun, condenser lens and objective lens. The aim of the electron optics is the demagnification of the image of the electron source to a very small spot.[17]

Firstly, the beam passes the condenser lens, which can be seen as a multiple lens system with an adjustable aperture to control the beam current. In accordance to the Rayleigh criterion, a big opening angle is favorable. Therefore, the multiple condenser lenses widen the opening angle. However, this increases the influence of the lens aberrations, which means that this trade-off has to be strongly considered when designing a SEM column. The objective lens eventually focuses the electron beam to the surface sample. By changing the working distance, the focal length of the objective lens has to be adapted which is realized by changing the magnetic field of magnetic lenses.[14]

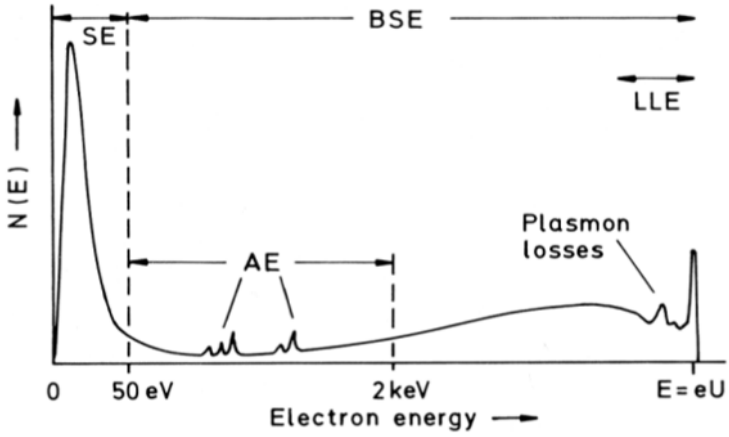

Figure 3: Number of electrons that are leaving the specimen in dependence of the electron energy. The energy scale can be roughly categorized into secondary electrons (SE) from 0 to 50 eV and backscattered electrons (BSE) from 50 eV up to the primary electron energy. Between 50 eV and 2 keV Auger electrons (AE) can be detected. In the range of low-loss electrons (LLE), the distinct peaks can be attributed to plasmon losses.[17]

2.1.3 Interaction of Electrons with Solids and Detecting Systems

When the impinging electrons called primary electrons (PE) hit the sample surface, they penetrate into the specimen and interact with the sample atoms. The interaction can be either elastic or inelastic leading to several possible signal types for detection. Due to the energy loss accompanied with inelastic scattering the electrons have a limited penetration depth, which depends on sample properties and acceleration voltage. The energy dispersive detection of electrons that are leaving the sample provide crucial information about the interaction processes of the electrons with matter (see Figure 3).[17]

Electrons that are scattered elastically (Rutherford scattering) are referred to as backscattered electrons (BSE) and have typical energy values between the primary energy and 50 eV. High energy BSE are called low-loss electrons (LLE). The elastic deflection is caused by the Coulomb force of the

nucleus point charge and lead to large scattering angles.[17]By interacting with the electrons of the atomic shell the PE are scattered inelastically which causes the emission of secondary electrons (SE), Auger electrons (AE) and x-rays. Also, the creation of quasiparticles such as plasmons and electron-hole pairs can be induced by inelastic scattering. The sample depth from which the SE can exit is highly dependent on the electron mean free path and hence of the sample material. Although they are generated inside the whole interaction volume, only SE that are very close to the surface are able to escape the sample. Also, high energy BSE produce SE on their path, which are then referred to as SE_2. The SE electrons generated by forward-scattered electrons are called SE_3. Die overall interaction volume generated by PE and BSE inside the sample can be illustrated with a Monte Carlo simulation as depicted in Figure 4[22].[17] The simulation shows strikingly the dependence of the penetration depth on the primary electron energy. Depending on the application the acceleration energy has to be adapted. For example, a low primary energy is preferential when aiming for surface information.

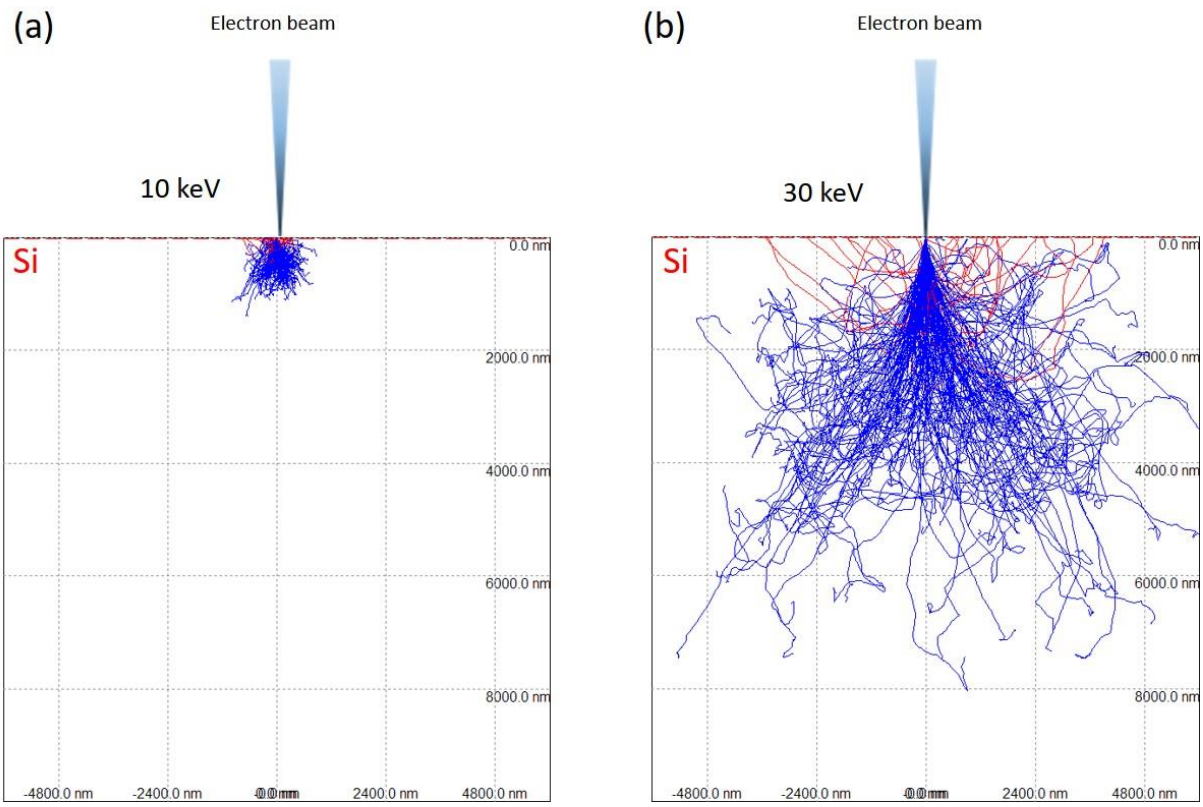

Figure 4: Monte Carlo simulation of 200 electrons penetrating with 10 keV primary energy (a) and 30 keV primary energy (b). The chosen sample material is Silicon as used during this thesis. The dependence of the penetration depth on the primary energy can be clearly seen as the 30 keV electrons clearly outnumber the penetration depth of the 10 keV electrons. In blue the trajectory of the electrons inside the specimen and in red the BSE.[22]

Due to the variety of the signals generated by the electron interaction with the sample, several detectors can be used for imaging and chemical analysis. The photons exiting the sample are collected with an EDX or WDX detector and can be used for the qualitative and quantitative chemical analysis of the sample. As depicted in Figure 3, a variety of crucial signals originate from the electrons, which are able to exit the specimen. In the DBM operated at FELMI-ZFE two electron detectors, the Everhart-

Thornley detector (ETD) and the through-the-lens detector (TLD), are used. The front part of the ETD is a Faraday cage, which can be biased on different potential. Low energy SE can be collected by applying a positive bias to the Faraday cage. By applying a negative voltage, only the high energy BSE will reach the detector as they are hardly deflected. However, the low energy SE are repelled by the electric field. When the electrons are sucked in the Faraday cage, they get accelerated by a strong voltage towards the scintillator. Once they hit the scintillator, the electrons generate many electron-hole pairs, which produce photons when they are recombining. The light pulses get transmitted through an optical waveguide to a photocathode generating photoelectrons, which are then amplified by an electron multiplier. The basic setup of the ETD is depicted in Figure 5.[14] The TLD, which is mainly used for ultra-high-resolution imaging, is located around the electron beam axis above the objective lens. For the attraction of the SE back into the electron column, a very high bias has to be applied. Since BSE are hardly influenced by the electric field, only SE are detected with a TLD.[14]

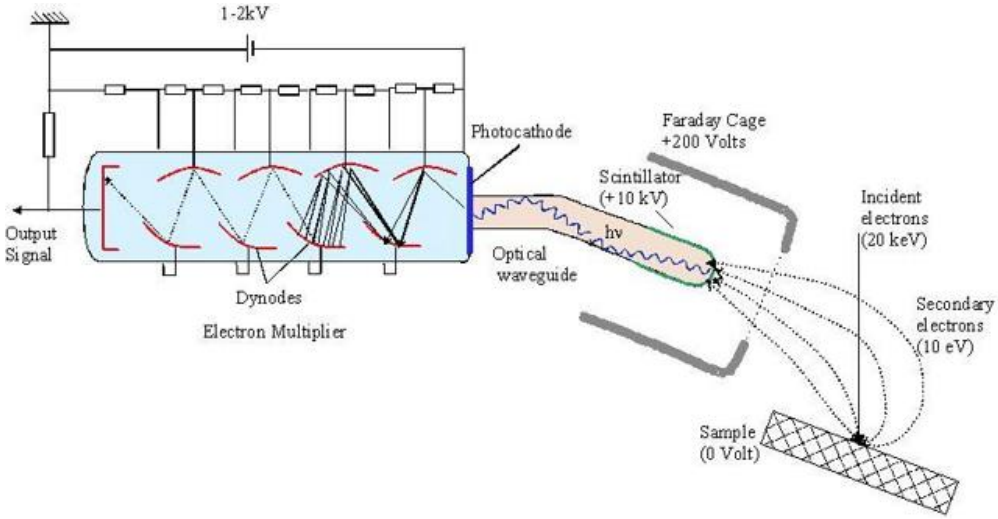

Figure 5: Scheme of an Everhart-Thornley detector (ETD) to visualize the working principle of electron detection. The detector is placed in a tilted position with respect to the sample surface. After being sucked in by the biased Faraday cage, the electrons generate photons at the scintillator. These photons induce an electron cascade by kicking out electrons at the photocathode, which then get multiplied by the electron multiplier.[23]

2.2 Focused Electron Beam Induced Deposition

2.2.1 Basic Concept

Focused electron beam induced deposition (FEBID) is a mask-less, direct writing technique that enables the fabrication of sophisticated structures at the nanometer-scale on virtually any morphology. The deposition is performed inside a SEM or FIB, in our case the DBM, and is based on the decomposition of molecules with the non-volatile part of the molecule remaining on the substrate as the deposit. A major advantage is the fact that generally no extensive pre-preparation of the sample and no post-growth processes are necessary.[24,25]

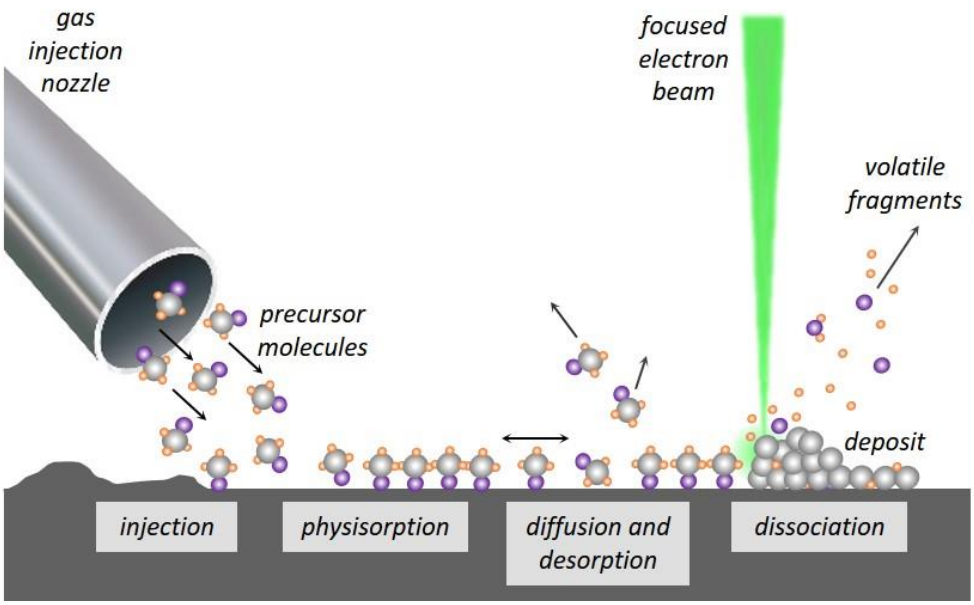

Figure 6: FEBID working principle. After the precursor molecules get injected through the GIS, they physisorb at the surface where they diffuse and partly desorb again. When the electron beam hits the precursor molecules, they get dissociated and the non-volatile fragments stay at the surface as the deposit.[15]

The principle of the technique can be seen in Figure 6 and is divided into 5 steps:[25]

1. Gas injection: The gas injection system (GIS) provides the precursor molecules, which will be decomposed. By constantly supplying the surface with gas, stable deposition parameters are established
2. Physisorption: After being injected, the precursor gas physisorbs at the surface.
3. Diffusion and desorption: The precursor molecules diffuse in accordance to the coverage gradient. They partly desorb due to thermal activation.
4. Dissociation: When the precursor molecules get hit by the impinging electrons, the molecule decomposes and the non-volatile part remains as the deposit.

2.2.2 Dissociation Mechanisms for Precursor Molecules

Since the precursor molecules contain the functional atom to be deposited, they are a crucial factor of FEBID. Various precursors for different central atoms (e.g. Pt ,Au ,Si ,W ,Fe) have been developed in order to provide a variety of functional materials fabricated via FEBID.[26] Generally speaking, a suitable precursor has to fulfil a number of requirements including high volatility, sufficiently long residence time at the surface, complete decomposition under electron exposure, high desorption rate of the volatile dissociation product, high stability during storage and supply. On top it should be preferably non-toxic and not too expensive.[27,28]

In many cases, the precursor molecules are metalorganic compounds, which will be also used in his thesis. Hereby, the central atom is surrounded by organic ligands, which are supposed to desorb after the dissociation. The used precursor for our experiments was $Me_2Au(acac)$ (dimethylgold^{III} acetylacetonate)[29], which is deployed for gold depositions.[30]

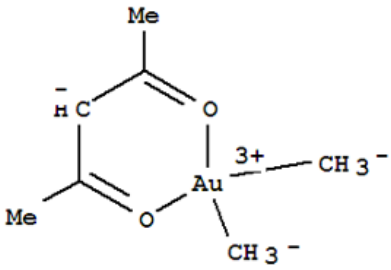

Figure 7: $Me_2Au(acac)$ precursor is an organometallic compound for the deposition of gold. The functional atom Au is surrounded by hydrocarbons.[29]

The composition of the FEBID structure heavily depends on the dissociation mechanism induced by the impinging electron. In order to fabricate pure deposits, all ligands must be removed from the metal atom and desorb. The dissociation cross section for different electron energies show that mainly electrons with a few eV (SE) are responsible for cracking up the precursor molecules.[31] However, due to the fact that energies for stripping the ligands cannot be narrowed down to distinct values and the SE have continuous energy spectrum, the bond dissociation is not selective. Hence, any bonds of the precursor can break up, possibly resulting in non-volatile intermediate dissociation products, which then contribute to the final composition of the deposit. For that reason FEBID deposits usually contain a high carbon content of 90 at % and more[26]. Figure 8 shows a TEM image of a Platinum FEBID deposit with a Platinum content of 15 %[32].[27]

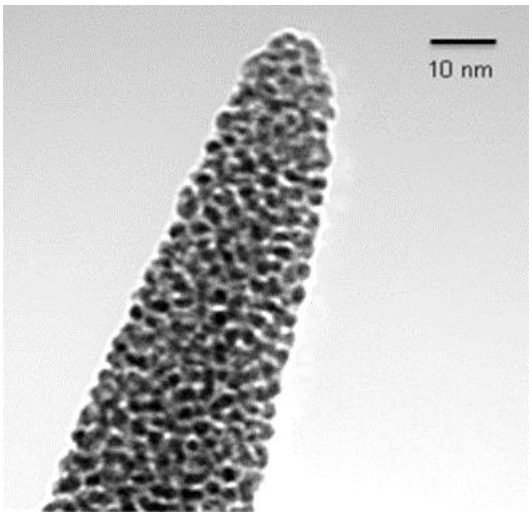

Figure 8: TEM bright field image of a Platinum FEBID deposit with a platinum amount of 15 %. The dark spots are Platinum grains, which are surrounded by carbon.[32]

2.2.3 Continuum Model

In order to describe and discuss the principles of growth rate and resolution of FEBID deposits, Utke et al. [27] introduced the continuum model, which describes the FEBID dynamics with analytical equations. The basic assumption is that the precursor molecules get injected via the GIS and get depleted due to dissociation induced by an electron beam. Further it can be assumed that no chemical bonding of the precursor molecules with the surface occurs. Hence, the adsorbates are able to spontaneously adsorb and desorb from the surface. Moreover, by heating and cooling the substrate and simultaneously observing the deposition rate, it could be determined that dissociation of molecules in the gas phase play a minor role on the growth rate.[33] Therefore, only the surface adsorbates are taken into account for dissociation processes.[27]

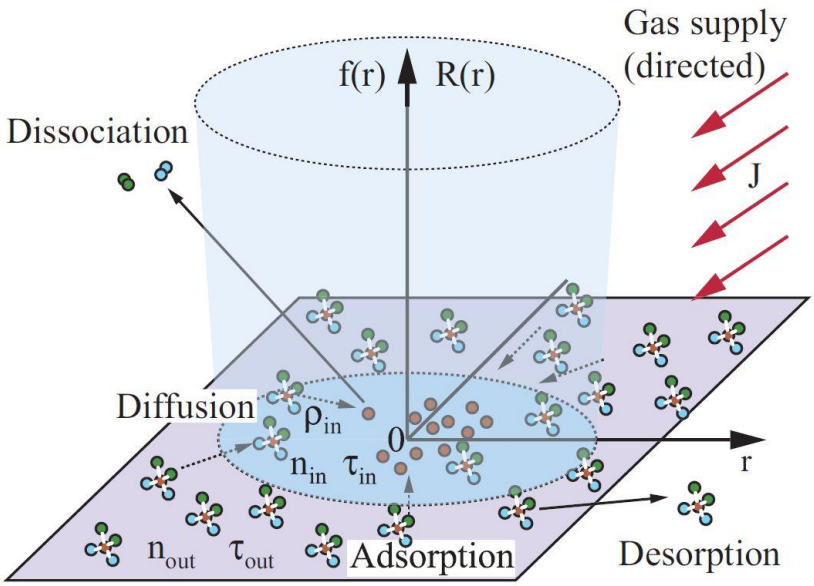

Figure 9: Scheme of the processes included in the continuum model to describe the FEBID deposition process. The adsorbate kinetics and coverage can be modelled with a constant gas supply (red arrows) and 4 processes: adsorption, diffusion, dissociation and desorption. The blue cone illustrates the area where deposition takes place.[34]

In order to determine the kinetics and coverage of surface adsorbates, a differential adsorption rate equation was introduced, which is determined by four key processes:

$$\frac{\partial N}{\partial t} = \underbrace{sJ\left(1-\frac{N}{N_0}\right)}_{Adsorption} + \underbrace{D\left(\frac{\partial^2 N}{\partial^2 r^2}+\frac{1}{r}\frac{\partial N}{\partial r}\right)}_{Diffusion} - \underbrace{\frac{N}{\tau}}_{Desorptiom} - \underbrace{\sigma f N}_{Dissociation}$$

N	*number of adsorbates at the surface*	*σ*	*dissociation cross-section*
s	*sticking coefficient*	*τ*	*average residence time*
J	*Molecule flux*	*f(r)*	*electron beam profile*
D	*surface diffusion coefficient*	N_0	*molecule number for a monolayer*

The adsorption term is restricted to the non-dissociative Langmuir adsorption, which is limited to a monolayer. In Figure 9 the adsorbate kinetic and depositions process is schematically illustrated. The blue cone schemes the interaction volume of the electron beam with the adsorbates, which is a function of the distance from the centre of the electron beam. The highest deposition rate can be observed in the centre of the electron beam in accordance to the Gaussian shape of the electron beam intensity distribution.[27]

2.2.4 Working Regime

The prevalent FEBID working regime is determined by the ratio of electrons and precursor molecules. This ratio is essential for the deposition behavior as it directly effects growth rate, deposition shape[35] and the chemical composition[36] of the deposit. The working regime can be divided into two major states:[27,36,37]

- Reaction rate limited (RRL) regime: This state is established if the available precursor outnumbers the dissociating electrons. Hence, the growth rate is limited by the number of electrons. In case of the RRL regime, the molecule coverage in the central area of the impinging electron beam is sufficient high and therefore the strongest growth rate is established around the focal spot. This leads to a deposition shape representing the Gaussian profile of the electron beam, which is also the thinnest possible structure shape. It is desired to achieve a RRL regime for fabricating high resolution FEBID structures.
- Mass transport limited (MTL) regime: This regime is characterized by a higher number of dissociating electrons in comparison to the precursor molecules. Therefore, the growth rate is limited by the number of precursor molecules at the patterning spot. Because the central deposition area is only replenished directly from the gas phase and the outer areas also from surface diffusion, the vertical growth rate decreases and the lateral growth rate increases. A flat-top deposition morphology can be observed.

In between these two extreme conditions a transition regime called the diffusion enhanced regime (DER) is established. The deposit shape turns out to be from flat-top shape to broad Gaussian-shaped depending whether it is closer to the RRL regime or MTL regime or exhibit an indent shape.

Since the combination of precursor coverage, dissociation mechanism and electron flux is all described by the FEBID working regime, it is the essential part of describing the deposition behavior. For example, we are able to get vital information about the precursor dynamics in different patterning areas by observing the deposit shape and growth rates and keeping beam parameters and GIS alignment constant.

2.3 Purification Process

FEBID deposited structures usually contain high carbon content of 90 at % and more[26] (see chapter 2.2.2). Since the requirements for many applications like plasmonics require highly pure materials, the purification process represents a crucial step towards the functionality of the FEBID

deposits. There have been few examples of pure materials after deposition.[38,39,40] However, these techniques often involve highly toxic and reactive inorganic precursor and are limited to a few materials. In 2014 Geier et al.[10] introduced the first post growth purification process resulting in highly pure and compact platinum structures. This process could be successfully transferred to the purification of gold based compounds by Winkler et al.[30] This purification step is based on electron irradiation in aqueous environment realized in an electron scanning environmental microscope (ESEM).

2.3.1 Environmental Scanning Electron Microscope

An environmental scanning electron microscope (ESEM) is a special SEM type where a gaseous environment in the specimen chamber is utilized. In comparison to a conventional SEM where the operation necessitates high vacuum, the pressure in the specimen chamber of an ESEM can be up to 2660 Pa. Typically, the ESEM is used for imaging insulating samples without any conductive coating. Since the impinging electrons cannot be discharged at non-conductive samples, a dipole field is induced, which strongly interferes with the imaging electron beam. Inside the specimen chamber of an ESEM the electron beam also generates positive gas ions that discharge the sample surface. However, the gaseous ambience also reduces the resolution due to scattering between the primary electrons and gas ions. Commonly, air or water are used as gases in an ESEM. But also other gases like He, Ar, N_2 or CO_2 are used depending on the experimental setup and the specimen.[21]

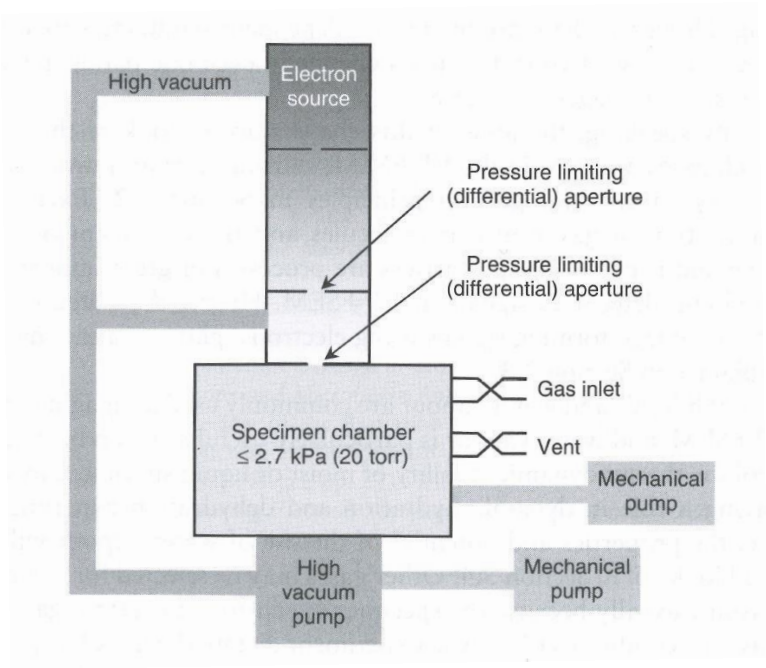

Figure 10: Simplified scheme of an ESEM. The different pressure zones represented by grey shades are induced by pressure limiting apertures. The gas inlet provides the molecules to establish a gaseous environment inside the specimen chamber.[21]

Next to many similar components to a conventional SEM like the electron source or the lenses, an ESEM also requires different technologies in order to maintain a gaseous environment inside the chamber. The pressure limiting apertures divide zones with different ambient pressure. By moving further upwards the electron column, the ambient pressure is decreasing. Moreover, a gas inlet is necessary for initially providing and keeping the gaseous ambience. A basic setup of an ESEM is depicted in Figure 10.[21]

2.3.2 Low Temperature Purification in Aqueous Environment

The post-growth purification method introduced by Geier et al.[10] was the first approach for obtaining fully purified and highly compact FEBID Platinum structures. The depositions were performed using the $MeCpPt^{IV}Me_3$ precursor. In the course of fabricating 3D plasmonic gold structures, Winkler et al.[30] successfully transferred to purification to gold based deposits fabricated by dissociating gold precursor molecules $Me_2Au(acac)$.

The purification process is based on the exposure of the deposits to an electron beam in H_2O atmosphere, which is realized in an ESEM. By providing the activation energy, the impinging electrons cause a reaction of the non-volatile carbon-metal compound with H_2O resulting in pure metallic structures and volatile products (CO, CH_4).[41] For verification, the chemical composition of the FEBID structure was simultaneously observed via energy dispersive x-ray spectroscopy (EDXS). Hereby, the theory could be successfully validated and the purity of the metallic structures was determined. Transmission electron microscope (TEM) images revealed that the grain size of the fully metallic structure increases compared to the carbon-metal compound. Moreover, significant volume losses of 69 % and structures without any cracks and pores could be spotted via atomic force microscope (AFM) measurements. The deposits experience minimal lateral shrinking and homogenous vertical shrinking, which is highly desirable.[10]

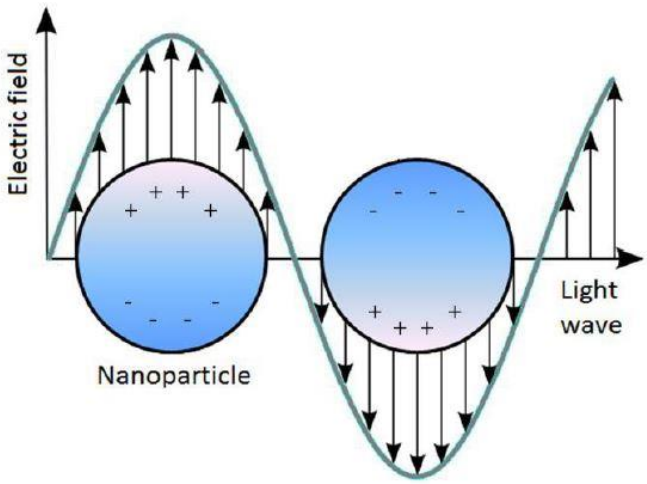

Figure 11: Scheme of LSPR where the mobile conduction electrons inside the metal are moved on either one side of the particle depending on the phase of the electromagnetic wave. Due to the wave nature of the exciter, the conduction electrons also exhibit periodic oscillations (plasmons).[45]

2.4 Plasmonics

With its positive ions and movable conducting electrons, a metal can be described as a plasma. When bringing the mobile charge carrier in collective oscillations induced by electromagnetic waves we speak of plasmons. The study of these plasmons is called plasmonics and has recently found great interest due to the ability of plasmonic structures to manipulate phase, polarization and amplitude of electromagnetic waves[4].[42] Localized surface plasmon resonance (LSPR) are of special interest since the resonance frequency of LSPR can be tuned from ultraviolet to infrared by changing the structural design.[42] The shapes can vary from stars[43] to crescents[44]; in this thesis the particles are shaped as pills. By increasing the particle size a shift towards higher LSPR frequencies is induced[42]. In order to observe LSPR in the visible range exceedingly small structures in the range of several-10 nm have to be fabricated as pursued in the course of this work.

2.5 Atomic Force Microscopy

Atomic force microscopy (AFM) is a scanning probe technique that generates 3D- maps of surfaces down to atomic resolution[46] by rastering a fine tip over a surface. The morphological information is extracted from the vertical movement of the tip, which is mounted on a cantilever. Besides the height information, a variety of further properties like magnetic properties, conductivity, temperatures and many more[47,48] can be obtained with specific AFM measurements techniques. Furthermore, it is possible to conduct measurements in vacuum, in gaseous or liquid environments which opens the door to time-resolved in-situ studies[49].

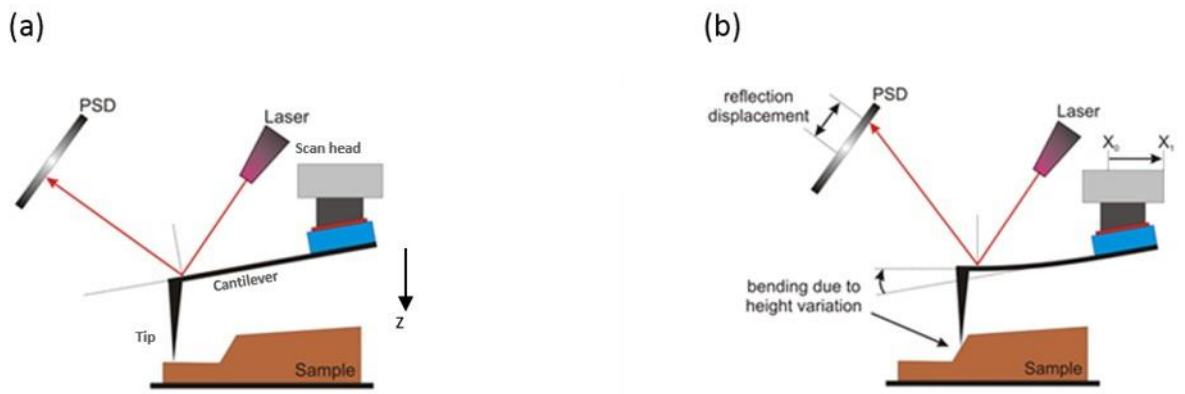

Figure 12: Scheme of a basic AFM setup consisting of a sample stage, a scan head with a tip mounted on a cantilever, and a detection system for the deflection of the cantilever, which comprises a laser and a Position Sensitive Detector (PSD). (a) The scan head gets lowered and the tip snaps to the surface. (b) The movement in the x-direction causes a bending of the cantilever to a sample height variation, which can be detected by the reflection displacement on the PSD.[17]

The operating principle of an AFM is based on rastering the sample line per line while recording the cantilever deflection, which is caused by the sample topology. By combining the 2D raster with the information about the cantilever deflection, a 3D map of the sample surface is created. The basic setup is depicted in cand consists of an sample stage, a scan head, a tip attached to a cantilever and a

detection system for observing the cantilever deflection. In our case the detection system comprises a laser and a positioning sensing detector (PSD). The laser points at the end of the cantilever at which the tip is mounted and is reflected onto the PSD. By moving the scan head over a morphological feature like in Figure 12 (b) the cantilever gets deflected and consequently the laser gets reflected to a different spot onto the PSD. A readout and control unit combines the information of the tip position together with the reflection displacement resulting in space-resolved surface information.[17] In order to perfrom the rastering and to place the tip onto the surface, the scan head has to be moved in the x-, y-, and z-direction. The movement is realized with mechanical means and piezoelectrical acuators for coarse and fine movement, respectively. The piezoelectrical actuators are placed within the scan head and are capable of performing shifts exceedingly precisly in the picometer precision. For performing vertical movements an elongated setup, which includes a piezoelectrical material contacted along the sides by a pair of electrodes, is used. Applying either a positive or a negative voltage will result in an expansion or contraction of the piezoelectrical material. Whereas for the movement in the lateral directions a tube scanner consisting of 4 pairs of electrodes is sufficient Figure 13 (b)). In order to shift the cantilever laterally, the opposite electrodes have to be exposed to an opposite bias, which will lead to a contraction on the one side and an expansion on the other side. Hence, the tube scanner will bend and a lateral shift is achieved.[17]

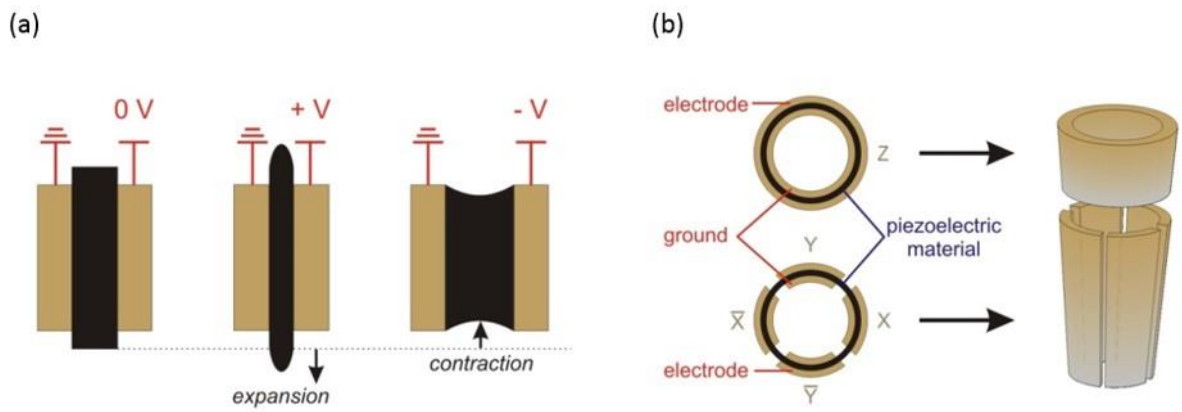

Figure 13: Setup and mode of operation of piezoelectric actuators responsible for the fine movement of the scan head. (a) A pair of electrodes contacting the piezoelectric materials along the sides designed for expansion and contraction in the z-direction. (b) Tube scanner consisting of 4 pairs of electrodes used for the lateral movement of the scan head in the x-, and y-direction.[17]

As previously mentioned the surface topology can be deduced from the cantilever deflection, which is determined by the interaction between the tip and the surface. In close proximity to the sample two competing forces can be identified: the attractive Van-der-Waals force and a repulsive force caused by the Pauli exclusion principle. For distances between 10 nm – 0.5 nm the Van-der-Waals force is dominant and consequently the tip experience attraction towards the surface. Whereas for distances smaller than 0.2 nm the Pauli repulsion prevails.

The potentials caused by these two forces can be summed up to the Lennard-Jones-Potential:

$$V_{Lennard-Jones} = V_{Repulsive} + V_{Van-der-Waals} = \frac{a}{r^{12}} - \frac{b}{r^{6}}$$

In Figure 14 (a) the force curve and the Lennard-Jones potential, which are depicted by the black and the blue line, respectively, reveal two major regimes. While following a tip approaching the surface, the change between these regimes can be can clearly followed (Figure 14 (b), (c)). Firstly, the far reaching attractive forces (highlighted in green) dominate. At a certain distance between the sample and the tip the attraction towards the sample forces the cantilever to bend over and snap onto the surface (C). This position correlates to the minimum of the Lennard-Jones-potential at which the acting forces are zero. By further lowering the tip the repulsive regime becomes prevalent leading to a positive cantilever deflection. The two curves in Figure 14 (b) show the difference between the downward and upward movement. While moving upwards the tip stays longer in contact with the surface due to additional adhesion forces (D-E).[17]

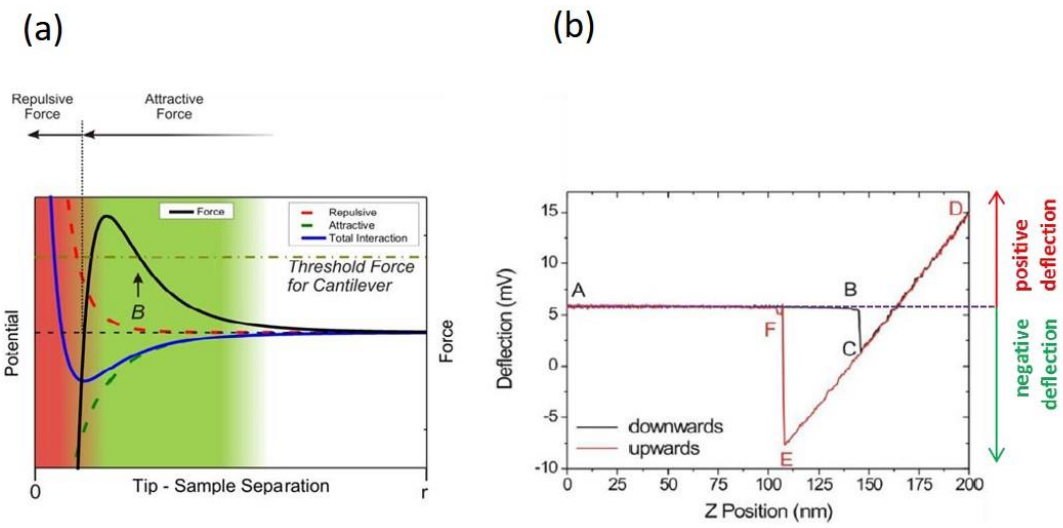

Figure 14: Interaction between the tip and the surface represented by the force curve and the Lennard-Jones-potential in (a) by the black and the blue line, respectively. Two major regimes are revealed: the attractive highlighted in green and the repulsive in red. By approaching the surface we are able to observe the prevalent regime by the correlating cantilever deflection (b,c). After snapping to the surface due to the attractive forces (C), the cantilever gets repelled when the tip-surface distance is further decreased. While moving upwards, the adhesion forces hinders the tip from lifting (C-E).[17]

Numerous AFM modes have been developed since the invention in 1986[50] : contact mode , non-contact mode, peak force mode, conductive AFM, chemical AFM, to only name a few. In this course we will concentrate on the tapping mode (intermittent-mode), which is shown in Figure 15. In the tapping mode the cantilever oscillates in very close proximity to the surface at its resonance frequency driven by an excitation piezo. By interacting with the surface due to the forces mentioned above, the oscillation amplitude and oscillation phase changes. The amplitude change is used as the input variable for a feedback loop, which re-adjusts the tip-surface distance in a way to maintain a set cantilever oscillation amplitude. Consequently, the height profile can be deduced from the readjustment of the

cantilever. Moreover, the phase shift provides information about the surface properties. The prevalent forces on the tip, are highly dependent on the surface properties and therefore determine the cantilever deflection (Figure 14). Attraction induces a negative oscillation phase shift whereas operating in the repulsive regime results in a positive phase shift. By evaluating the phase shift information, crucial material properties like elasticity can be extracted.[17]

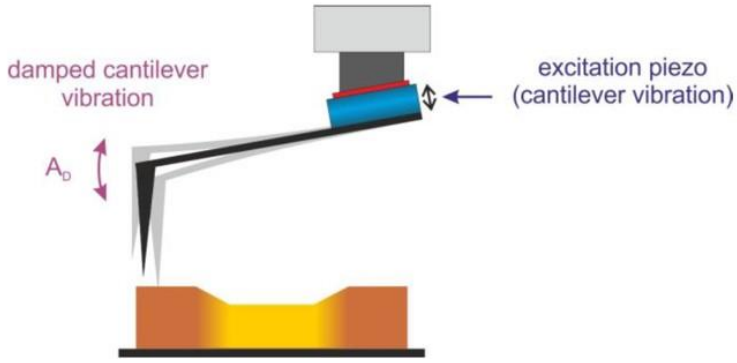

Figure 15: Operation principle of the tapping mode. The cantilever gets excited at its resonance frequency with an excitation piezo placed on the scan head. When the tip hits the surface the cantilever vibration gets damped. The damping magnitude is used as the input variable for the feedback loop.[17]

Especially at ambient conditions the tapping mode can make use of its inherent advantages. Due to the humidity in the ambience most samples develop a fluid film on the surface, the so called wetting layer. This fluid film presents a major problem for a contact-mode measurement as the tip is likely to stick to the surface due to adhesion forces induced by this layer, which can distort the measurements. The oscillating cantilever prevents the tip to stick in the fluid. However, we also have to take the wetting layer into account while operating in the tapping mode. As the requirements on the measurement precision in this thesis are exceedingly high, it is inevitable to operate in the repulsive working regime. This comes along with higher oscillation energy and therefore less influence of the fluid layer on our measurements.[17]

Another big advantage of the intermittent operation mode, is the generally less damage done to the surface. Compared to the contact-mode, the interaction time between the tip and the surface is shorter and the lateral forces between the tip and the surface are considerably decreased. Some possible surface damages during AFM measurements can be seen in Figure 16 (a). In conclusion, the tapping mode combines the surface sensitivity of the contact mode with a low damage related to the non-contact mode.[17]

Although the height resolution of AFM measurements is incomparably high, the lateral resolution might be impaired by the shape of the tip as the measurement is a convolution of the present sample morphology and the tip geometry (Figure 16 (b)). Most importantly, the requirement on the tip radius is to be as fine as possible to resolve even very fine particles. Having a dull tip results in an additional intrinsic broadening, which is highly unwanted. Moreover, impurities, which are stuck to the surface, lead to an impurity relate convolution. These broadening effects have a particularly high impact on structures with a high aspect ratio.[17] During this exercise all measurement were conducted with a Bruker Dimension Fastscan using the tip model OTESPA-R3 from Bruker.

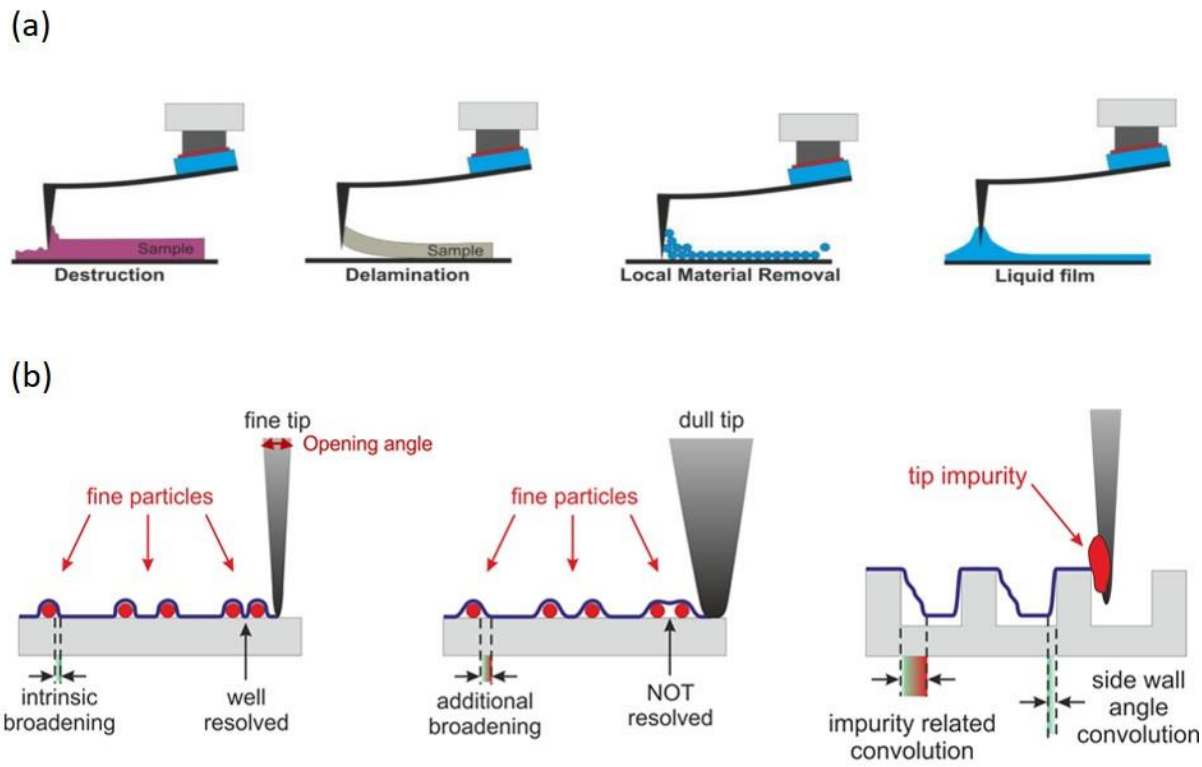

Figure 16: Possible problems during AFM measurements. (a) Sample destruction caused by the interaction of the tip with the surface. The very right scheme shows additional adhesion forces, which can manipulate the exact morphology determination. (b) Tip related lateral broadening due to dull tips or impurities stuck on the tip. As the lateral resolution is a convolution of the tip and the sample morphology a fine tip is essential.[17]

3 Related Previous Work

This master thesis was built on several previous findings of members of the work group around Prof. Harald Plank at the FELMI-ZFE. The aim of this thesis is the on-demand fabrication of gold nanostructures for plasmonic filters in the THz range. The proof-of-principle of the fabrication of plasmonic active gold structures in the nanometer scale via FEBID was already made by U.Haselmann[51].

In a consecutive work, U. Radeschnig was able to further understand the fundamental growth dynamics of FEBID gold deposits. He achieved a predictable downscaling of the deposited structures, which is highly demandable because the dimensions for plasmonic applications are very challenging.[52] These results will be summarized shortly in the following, as they are relevant for this thesis as well.

3.1 Fabrication of Plasmonic Gold Nanostructures

During his master thesis U. Haselmann successfully proved the feasibility of fabricating pure gold nanostructures via FEBID using the Me_2-Au(acac) precursor.[51] After deposition, the structures using the Au precursor $Me_2Au(acac)$ still contain up to *95 at. % carbon.*[26] In order to fabricate pure metallic structures a post-growth purification process is needed. Introduced by Barbara Geier et al.[10] in 2014 for the Platinum precursor $MeCpPt^{IV}Me_3$, this crucial process step (see chapter 2.3) was successfully applied for gold deposits as well. By analysing fully purified Au disks via TEM-based nano-characterization, surface plasmon resonances could be clearly revealed. This fundamental insight unfolds the perspective of further plasmonic Au depositions via FEBID. The emphasis was put on bi-ring shaped structures, which are expected to perform plasmonic response in the visible range. The underlying simulations were conducted by the work group around Prof. Roskos at the Goethe University in Frankfurt. The aimed structure had a line width of 25 nm and a height of 5-15 nm of fully purified gold. At this point these dimensions were considered to be close to the fundamental resolution limits of FEBID[53] and the question emerged whether it is feasible to fabricate complex structures with dimensions close to this limit. The optimum configurations for high resolution depositions, which included a beam current of 21 pA, a beam voltage of 30 kV and a carefully adjusted GIS, were already found in foregoing findings by Winkler et al.[54]

A very important aspect concerning FEBID depositions is the influence of the point pitch (PoP), which is defined as the distance between two consecutively irradiated points, and the specific total exposure time (S-TET). Haselmann revealed that a PoP of 10 nm is more controllable due to the linear growth behaviour and has a more uniform height distribution along the ring compared to shorter PoP. Moreover, it could be shown that the height accuracy is widely independent of the S-TET. With a height deviation of ± 1 nm, the accuracy was highly remarkable considering that the RMS surface roughness of the substrate already had a value of 0.6 nm. In order to achieve conductivity, the upmost substrate layer was chosen to be indium tin oxide (ITO). The subsequent purification process at 5 kV, 5 nA and a chamber pressure of 10 Pa H_20 lead to pure gold structures, which kept their footprint and most importantly did not show any cracks or disruption. In Figure 17 the highly satisfying results of the bi-ring morphology is shown before and after purification.[51]

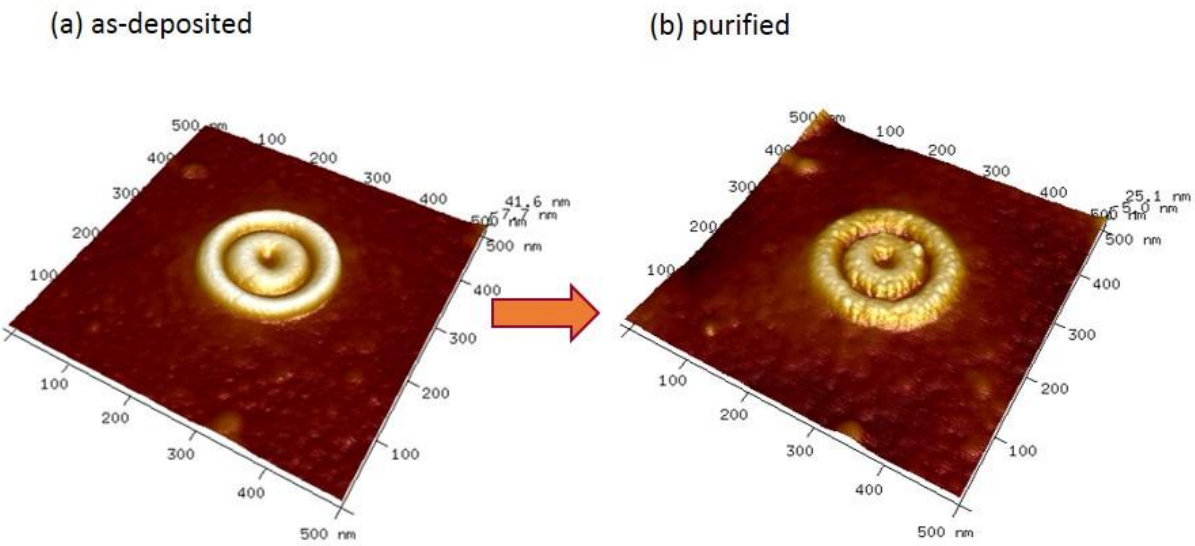

Figure 17: AFM height image of an as-deposited bi-ring (a) and a bi-ring after purification (b) within a cavity. It can be clearly seen that the bi-ring kept its footprint and does not show any cracks or disruption after the purification process.[51]

The expected plasmonic response of the bi-rings will only be exhibited if the bi-rings are placed in a large-scale array. Hence, U. Radeschnig proceeded with the deposition of a 12 x 12 array of bi-rings. In order to conduct subsequent optical measurements, the array was placed inside a morphological cavity (Figure 31) on a transparent substrate (glass-ITO stack). The location inside the cavity exposed systematic height variations of the deposits, which can be seen in Figure 18 (a) by the brighter areas. The heights varied from 8 nm to 13 nm which is summarized in a 3D surface plot in Figure 18 (b). This indicates a significant precursor distribution gradient, which has not been further investigated at this point. By comparing deposits inside and outside the cavity, another remarkable effect could be revealed. The favoured morphology of the cavity concerning gas accumulation led to an increase of the vertical growth rate by a factor of 3-4[51].[52]

However, the dimensions of the purified bi-rings showed a height of 2-4 nm and line widths of 35 nm (FHWM). These specifications did not coincide satisfyingly with the required heights of 5-15 nm at widths of 25 nm (FWHM). In summary, the successful purification process of structures for plasmonic THz-applications had been achieved, which is an essential step towards further research in this field. Nevertheless, the desired structure dimensions couldn't be reached. Therefore, further in-detail understanding of growth dynamics and the resulting deposition shapes was gained by U. Radeschnig[52] whose findings will be summarized in the following chapter 3.2.

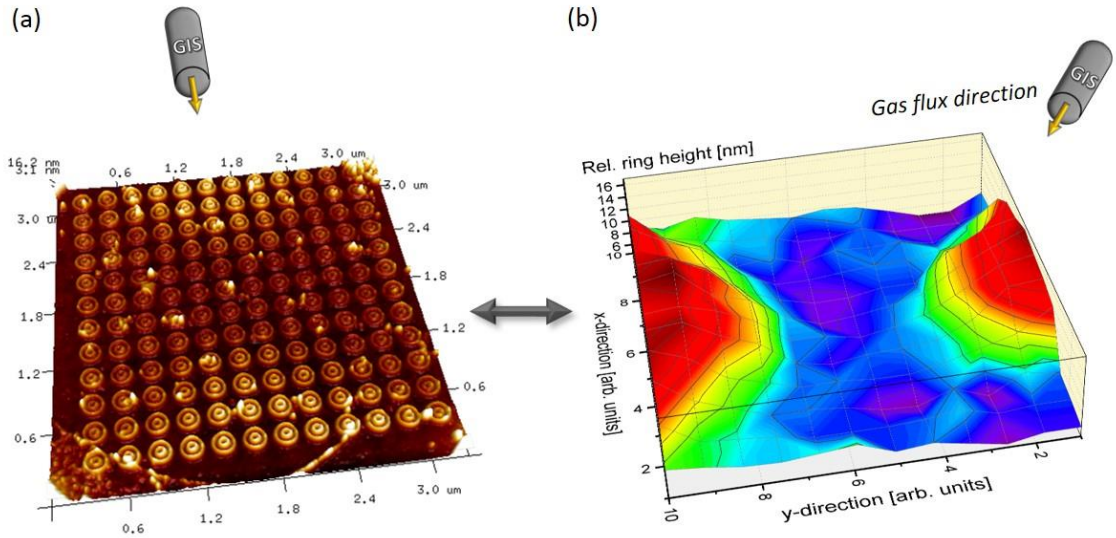

Figure 18: (a) AFM image showing the inhomogeneous height distribution throughout the cavity. (b) 3D plot to emphasize the present height variations. This distribution is expected to give conclusions on the precursor coverage inside the cavity.[52]

3.2 Predictable Downscaling of Gold Nanostructures

In order to control the deposition behaviour, it is irremissible to be fully aware about the prevalent deposition working regime. For obtaining the thinnest possible structures, RRL working regime conditions must be prevailed. The emergence of such regimes strongly correlates with the precursor density at the patterning point. Consequently, a test structure was chosen at which the prevalent regime can be classified for numerous deposition lines, which are expected to experience different rates of gas replenishment. This test structure consists of 7 nested “L”-shaped lines as shown in Figure 19 and can be divided in three different types of lines.

The “single line” is laterally exposed to two sides and is expected to have the highest precursor coverage as the replenishment via precursor diffusion takes place from two sides and from top down. For the “L” on the very bottom, which is called “outer line”, the replenishing process takes place laterally from one side and from top down. This results in a lower gas replenishment rate compared to the single line. The two lines in between the “single line” and “outer line” referred to as “inner lines” are expected to have the lowest precursor replenishment rate as the “outer line” represent a diffusion barrier and hence the gas replenishment mainly occurs from top down. The goal was to establish a RRL regime throughout the whole structure to obtain the thinnest possible and at the same time homogenous and similar developed lines in terms of height and widths.[27]

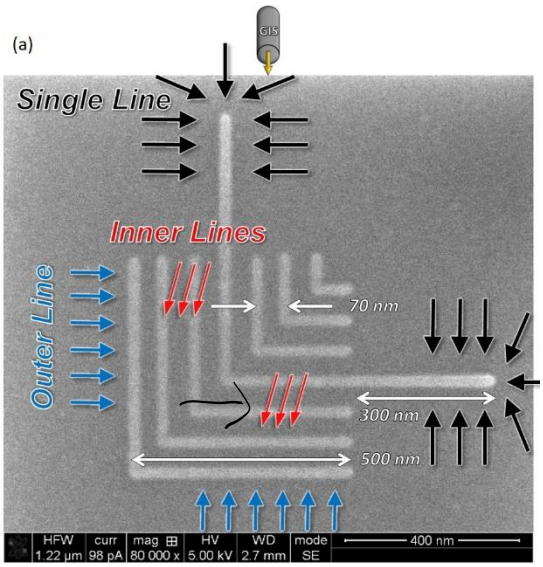

Figure 19: SEM image of the test structure, which consists of 7 nested "L"-shapes. The arrows indicate the precursor replenishment in dependence of the line type. There are three different line types: The single line (black) experiencing gas replenishment from two lateral directions and from top down. The outer line (blue) with gas replenishment coming from one lateral direction and from top down, and the inner lines (red) for which the gas replenishment occurs from top down only.[52]

As a first step, the distance between the GIS and the surface was strongly reduced to boost the local precursor density at the substrate and therefore the replenishment rate. Initially having a distance of 500 µm, which is the "eucentric height" in our DBM setup, it was reduced to 50 µm. Moreover, the prevalent working regime highly depends on the parameter pair dwell time (DT) and patterning cycles. By increasing the DT, the local precursor density in the proximity of the patterning point decreases. Subsequently, an unwanted shift towards the MTL regime takes place, which induces a broader line profile. By keeping the S-TET constant, the DT and the patterning cycles were varied to narrow down to optimum parameter set. For gold, this was found to be 100 passes at a dwell time of 100 µs. Using this setting, the line width could be decreased to a remarkable value of 12.5 nm at a height of 8 nm (Figure 20).

However, the profiles in terms of height and width between the line types showed significant variations. This inhomogeneity can be explained by the introduction of multi-pass depositions. The step by step increase of the structure height during every patterning cycle represents an incrementally increasing diffusion barrier for the precursor molecules. Due to the geometric constraint of the test structure, which reveals that the inner lines are surrounded by L-shaped lines placed further outside, the molecules have to overcome a longer diffusion path to reach the inner of the structure compared to a flat substrate. This hindrance of precursor replenishment towards the structure centre led to lower precursor coverage in the central areas of the L-structure accompanied with reduced vertical growth rates of the inner lines.

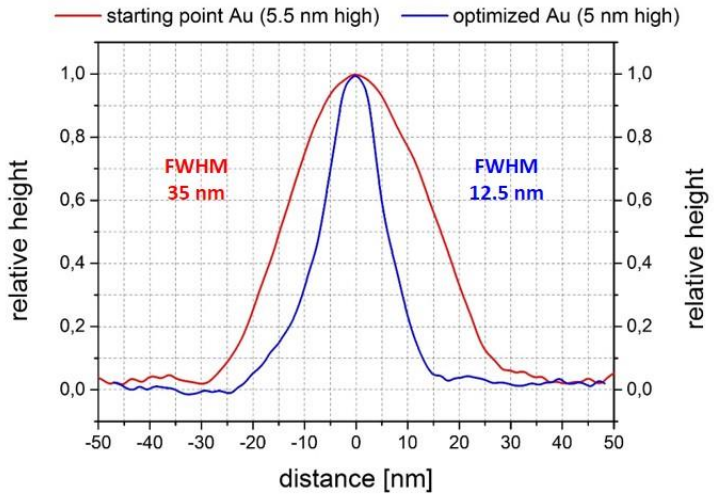

Figure 20: Comparison of the line profiles of an as-deposited bi-ring from (red line) and the vertical single line of the Au L-structure with the optimized parameter set (blue line). The lowered nozzle-to-surface distance and the introduction of multi-pass depositions show a significant improvement in the deposition accuracy.[52]

In conclusion, the previous master thesis provided a comprehensive insight of the deposition behaviour of high resolution gold structures via FEBID. The feasibility of fabricating pure gold deposits, which exhibit plasmonic resonances and the predictable downscaling to values, which seemed to be beyond the resolution limit could be achieved. However, there are still major challenges on the way to perform on demand fabrication of plasmonic nano-applications. Firstly, a strong influence of morphological cavities on the deposition behaviour was observed, which could not be explained thoroughly so far. And secondly, the benchmark in terms of widths and heights that was achieved by Ulrich Radeschnig (12.5 nm and 8 nm, respectively) has to be successfully transformed to plasmonic active designs. The solution of these challenges set up the subject of this thesis.

4 Experiments and Results

The aim of this thesis was the fabrication of plasmonic Au pill arrays, which act as filters in the THz range. Due to the highly challenging dimension of the aimed structures (see. Figure 32 (a)), gaining further knowledge of the deposition behaviour of the $Me_2Au(acac)$ precursor during FEBID was inevitable. Moreover, it was sufficient to develop sophisticated patterning strategies to fabricate homogenous nanostructure arrays. All depositions were conducted in a dual beam microscope (DBM), which consists of a scanning electron microscope (SEM) and a focused ion beam (FIB). After the deposition, the structures were further purified using an environmental scanning electron microscope (ESEM). The subsequent analysis was performed via atomic force microscopy (AFM).

For the optical measurement executed by the working group around Prof. Roskos, the pill arrays had to be placed in 10 x 10 μm^2 Au-windows on a glass-ITO stack (see Figure 31). In the course of previous works (see chapter 3) a massive change of the deposition behaviour comparing structures inside and outside a morphological cavity of 300 nm depth could be observed.[51] Hence, the first part of the experiments was addressed to the exploration of the gas distribution inside a cavity.

As a first step, the same "L"-structures as introduced in chapter 3 were fabricated inside the cavity and compared to the ones fabricated outside. This comparison provided a clear picture of the significant increase of precursor density inside. In order to work in an RRL regime, the optimum parameter set of DT and patterning cycles had to be derived while holding the S-TET constant (see chapter 4.1.1). The consecutive experiments revealed the presence of a lateral gas coverage gradient inside the cavity. The inhomogeneous distribution could be referred to effects originating from the accumulation of precursor molecules at the corners and borders of the edges discussed in chapter 4.1.2. To further boost the local precursor coverage, the distance between the gas injection nozzle and the substrate was reduced from 50 µm to 5 µm. However, this led to a stronger gas gradient within the cavity as depicted in Figure 28. Because homogenous deposition conditions in the whole patterning area are highly desired, this approach was discarded for the consecutive deposition of the pill arrays.

By starting with the deposition of each pill individually, we gained improved fundamental understanding of FEBIDs working regime influences on the fabrication of nano-structures with exceedingly small dimensions. In order to provide enough time for the precursor molecules to replenish and therefore operate in a RRL regime, we had to introduce the deposition of pills in line arrays, which included several structures during one patterning cycle. However, this approach caused residual depositions between the pills, which's prevention was addressed with the installation of a beam blanker. Although the issue with the residual deposition could be satisfyingly resolved, the installation of the new component led to slightly deformed pill shape due a beam drift induced by the beam blanker. Nevertheless, the optimized fabrication resulted in drift-corrected pill dimensions with an astonishing FWHM of 14 nm at a height of 21 nm. This results in an aspect ratio of 0.7 representing a worldwide benchmark in the FEBID community. To perform the expected plasmonic response, the pills had to be arranged in large-scale patterns. The main task was to achieve homogeneously distributed pill heights throughout the array, which could be realized with the introduction of a line per line patterning strategy. This approach led to remarkable small in-field variations of ± rel. 2 %. But, the splitting of the pattern into lines also resulted in marginal first shot effects and a periodic increase of the inter-line distance. Although the deviations within the large-scale array are not ideal

from a plasmonic point of view, any optimization was technically limited which means that we achieved the best possible results from a FEBID point of view. After the successful chemical transfer in pure gold structures without disrupting the morphology, plasmonic excitation could be experimentally verified. However, we identified a reduction in peak sharpness and intensity, which again could be addressed to technical limitations. The flowchart seen in Figure 21 illustrates the different issues that were faced during this thesis.

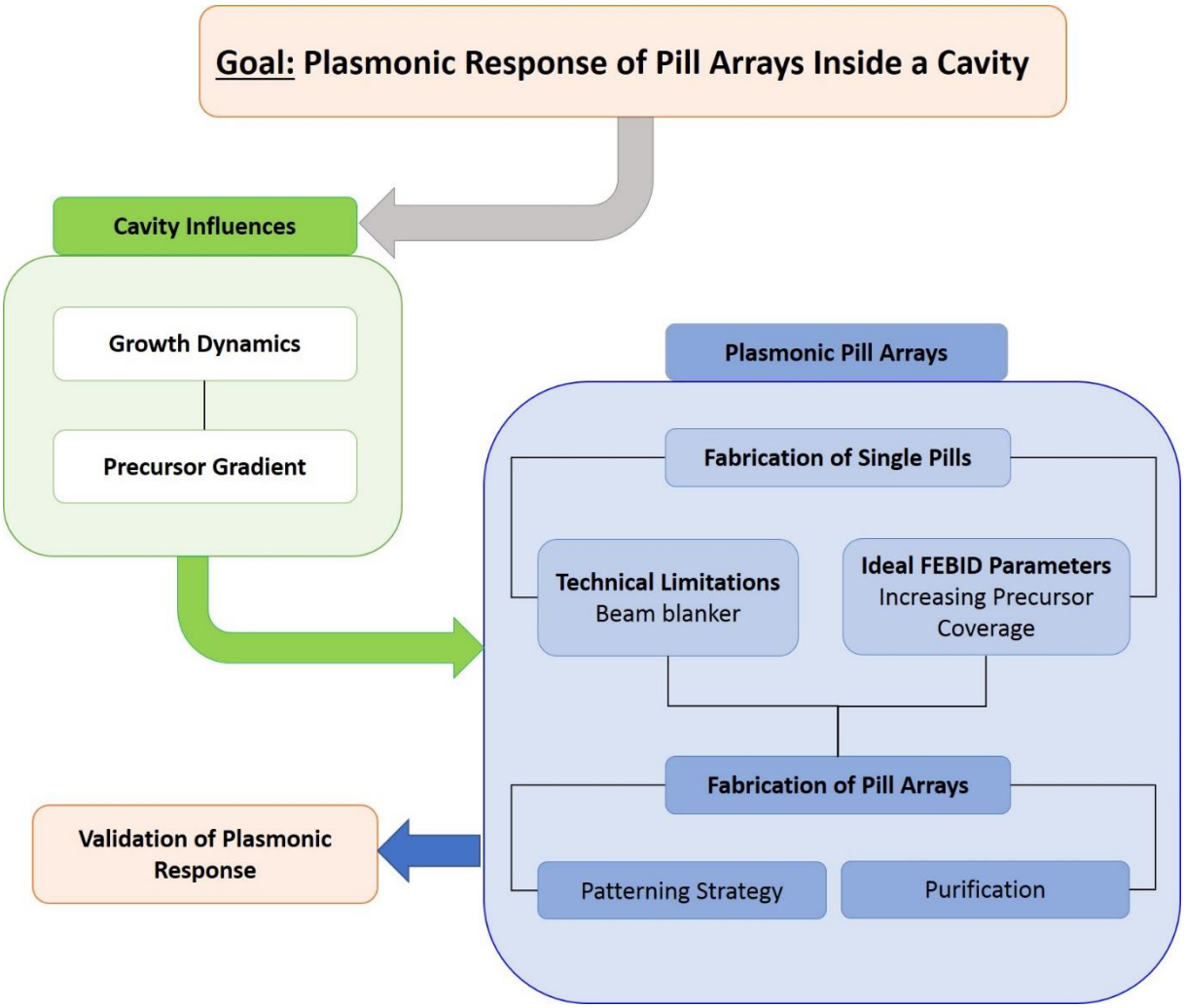

Figure 21: Schematic overview of the steps towards the goal of observing plasmonic response of pill arrays, which were placed inside a morphological cavity. Firstly, the influences of the cavity on the deposition behaviour were addressed. Subsequently, large-scale pill arrays could successfully be fabricated and purified which could be validated by optical measurements.

4.1 Influence of a Morphological Cavity on Au Depositions

The main idea of this section was to gather a comprehensive insight of the change of precursor dynamics induced by a morphological feature. More precisely, we wanted to gain knowledge about the gas dynamics inside a cavity. This knowledge about the gas distribution is inevitable to fabricate exceedingly homogenous arrays of plasmonic active nanostructures which is necessary for a maximum plasmonic response. The deposition inside a cavity is required to confine the light beam for subsequent optical measurements via near field microscopy[55].

The chosen test layout for the following experiments was the 7-fold "L"-structures, which we explained in detail in chapter 3. The main advantage is the profound understanding of the deposition behaviour of this structure from previous findings[52,56]. For data analysis, we deduced the values of line heights and line widths (FWHM) from the vertical outer line in the middle area if not explicitly mentioned differently. We conducted all depositions inside 10 x 10 μm^2 Al-windows with a height of 170 nm, which we fabricated via electron beam lithography on a Si-SiO_2 substrate. A special focus was put on the areas close to the borders and corners assuming a higher precursor density at these positions indicated by the orange frame in Figure 22 (a).

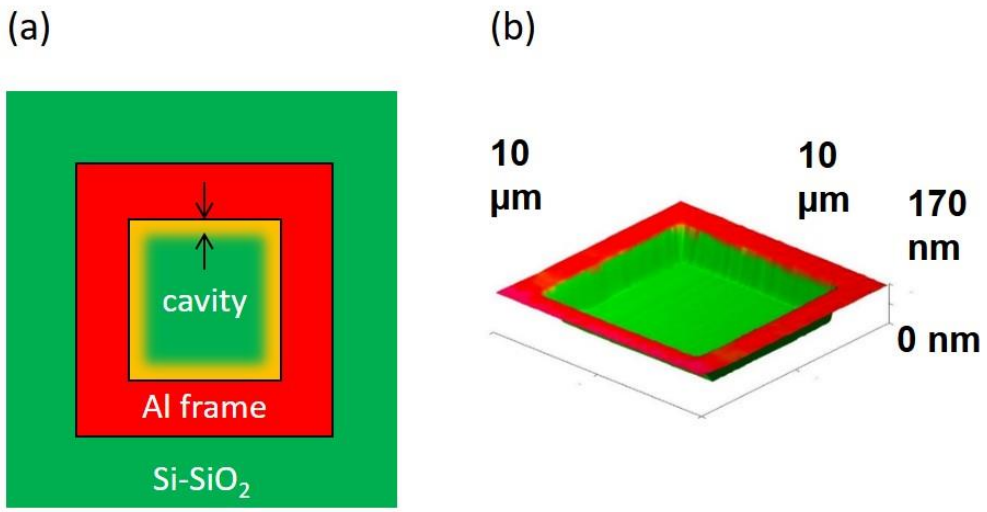

Figure 22: Sketch of an Al frame on a Si-SiO_2 substrate shaping a morphological cavity. The blurry orange area close to the Al frame indicates the assumption of higher precursor density at these areas. b) 3D AFM height image of a 10 x 10 μm^2 cavity. The Al frame has a height of 170 nm and was deposited on a Si-SiO_2 substrate.

The highly challenging dimension of the aimed pill structures close to FEBID's resolution limit[53,52] determined the framework configurations, which were kept identical throughout all following experiments. This includes a beam current of 21 pA, a primary electron energy of 30 keV and a carefully adjusted GIS, which was already found in foregoing findings by Winkler et al.[54] In order the rule out any influence of a possible stage drift, the stage was not moved for 5 minutes prior to deposition.

Moreover, the S-TET was kept constant at 1 µs/nm and the PoP was chosen to be 9 nm as the foregoing experiments by Ulrich Radeschnig et al. showed remarkable results with these values[52].

Firstly, we will compare deposits inside and outside the cavity with different deposition parameters to achieve a fundamental understanding of the impact of a changed proximal morphology. We will show that a shift towards the RRL working regime takes place leading to a significant increase of the vertical growth rate together with a decrease of the horizontal growth rate (chapter 4.1.1). For approaching the fundamental resolution limits, highest possible precursor coverage is desirable. Since the distance between GIS and substrate strongly correlates with the gas coverage, the distance will be varied to find the optimum GIS setup (chapter 4.1.3). Moreover, experiments using deposition positions with varying distances to the cavity borders and corners will reveal the present gas gradient inside the cavity (chapter 4.1.2). This knowledge will be vital for the consecutive deposition of large-scale pill arrays to ensure a homogenous height distribution.

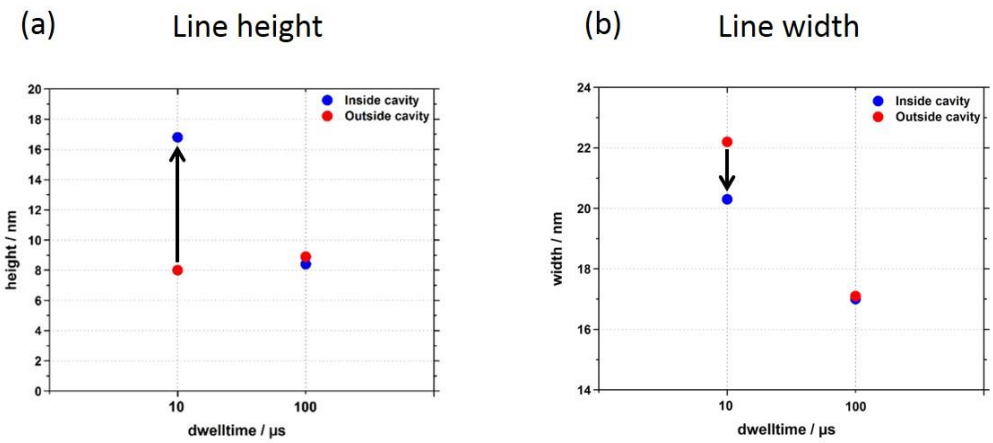

Figure 23: Dependence of the line height and line width on the dwelltime and on the deposition position for Au L-structures. a) For a DT of 10 µs the line height strongly increased by changing the deposition position from outside the cavity to inside the cavity, whereas for longer DT of 100 µs no significant changes in height were observed. b) The line width (FWHM) could be slightly reduced inside the cavity at a DT of 10 µs. On a flat surface, the change of proximal morphology didn`t cause a distinct change of the deposition geometry.

4.1.1 Deposition Behaviour Inside a Morphological Cavity

For obtaining the thinnest possible structures, the goal is to work in a RRL working regime (see Figure 24). The prevalent working regime strongly correlates with the duration of the beam pulse, and the present gas density. On flat surfaces the optimum DT was determined to be 100 µs[52].

In order to determine the ideal parameter for the changed proximal morphology, we chose two different DTs of 10 µs and 100 µs, respectively, and compared L-shapes inside and outside the cavity. The number of passes had to be adapted to the DT to ensure a constant TET of 10 ms at a PoP of 9 nm. For all further depositions of L-shapes the TET and PoP were kept at the same value. For short beam pulses of 10 µs we could find a tremendous increase of line heights from 8 to 17 nm together with a slightly decrease of the FWHM from 22 to 20 nm when moving from outside to inside the cavity as depicted in Figure 23. This clearly confirmed the assumption of higher gas coverage within the window

inducing a RRL working regime. As a result of the lower precursor density outside, a state of electron excess is reached within 10 µs inducing a shift towards the MTL regime, which leads to the undesired increase of the width to height ratio. In Figure 24 the deposition shape in dependence of the molecule coverage is demonstrated. Small deviations in the precursor coverage can lead to significant changes in the deposition behaviour, which makes a big impact especially for ultra-high-resolution depositions. In particular, the vertical growth rate decreases and the lateral growth rate increases at lower gas coverage (see chapter 2.2.4). We also have to take into account that a shorter pulse duration comes along with a reduction of the replenishment time until the next patterning cycle starts; in our case by a factor of 10. However, the pass by pass accumulation for gas replenishment was in the case of the L-shaped test structure with 515 patterning points and a DT of 10 µs adequate to provide optimum conditions for the consecutive pulse. By changing the DT to 100 µs, the line profiles of the test structures within and also next to the Al-window did not show big deviations as shown in Figure 23. This can be explained by an early precursor depletion during the beam pulse in both cases, inside and outside. After this initial local molecule consumption, a shift towards the MTL regime is established for the remaining DT. The better precursor situation prior the beam pulse inside the cavity has a less dominant influence on the deposition behaviour when the DT is extended. In previous works we could observe that a further decrease of the DT to values lower than 10 µs causes problems with the patterning accuracy for high resolution depositions[52]. The reduced contour accuracy can be explained by the limited speed of the electron beam that consequently cannot follow the patterning sufficiently fast. Therefore, the beam pulse duration for all further experiments was chosen to be 10 µs.

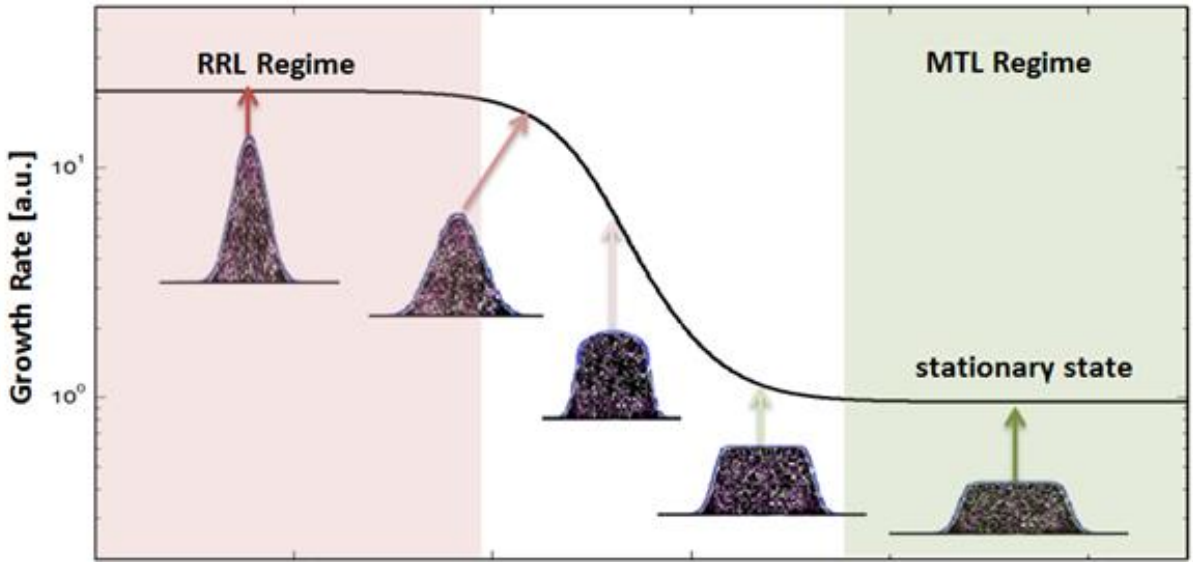

Figure 24: Change of the deposition shape on the prevalent working regime. The red area represents the reaction rate limited (RRL) regime, which leads to the highest vertical and simultaneously smallest horizontal growth rate. On the right side of the graph the mass transport limited regime (MTL) regime is depicted. The shortage of precursor molecules around the deposition spot causes an increase of the lateral growth rate together with a reduction of the vertical growth rate.[17]

4.1.2 Lateral Precursor Coverage Gradient

The requirements on the fabrication of plasmonic nanostructure arrays are extremely challenging and demand upmost accuracy. This necessitates homogenous precursor coverage within the whole patterning area. In previous works a strong lateral precursor gradient inside a morphological window was identified[51]. For this reason, it is vital to understand the underlying reasons of this phenomenon to counteract possible deviations in the deposition behaviour at varying patterning position.

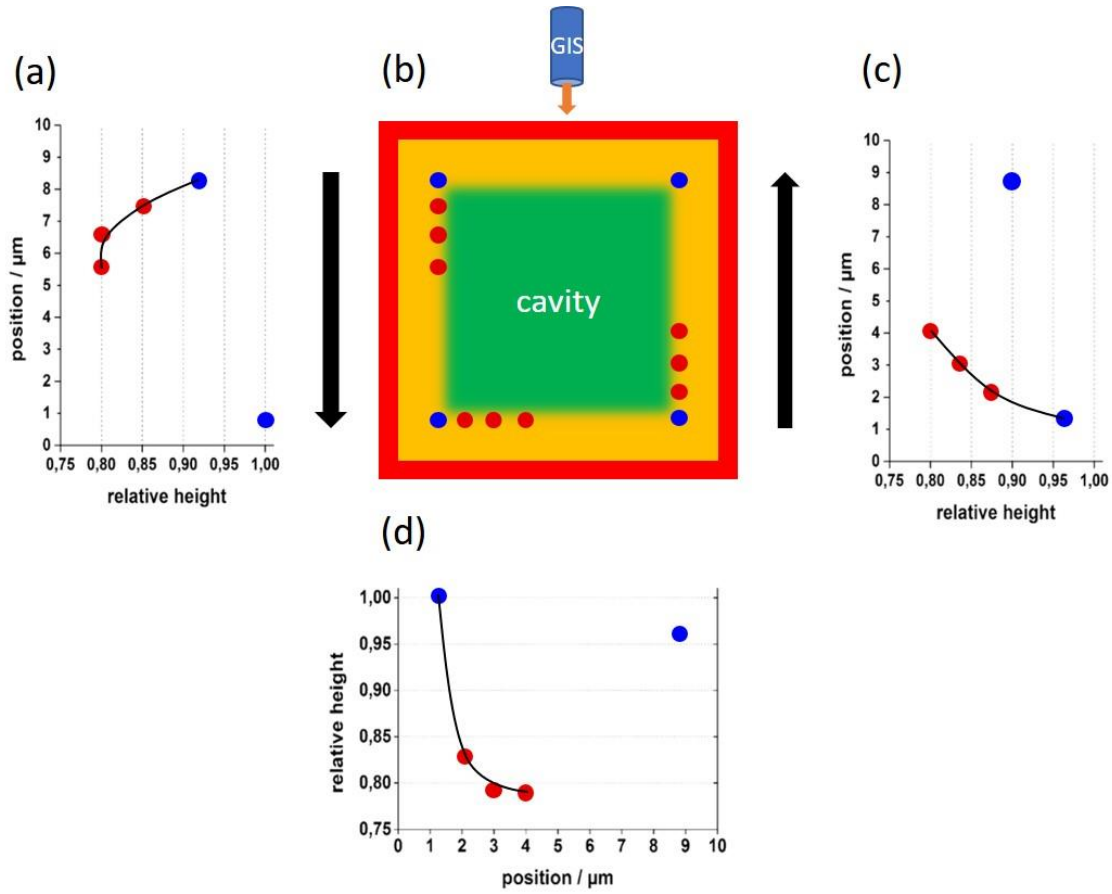

Figure 25: Dependence of the relative height on the position within a morphological cavity. b) True to scale sketch of the structure positions correlating to the position axis of the graphs in a), c) and d). The distance to the cavity borders is 1 µm for all deposits and the gap between the structures along each edge is increasing from 50 to 80 and finally to 200 nm. The deposition direction along the vertical borders is symbolized by the black arrows. As indicated by the orange frame, a gas gradient in the patterning areas close to the edges and corners is expected.

The following experiment, which can be seen in Figure 25 (b), was set up to determine possible effects, which might induce the precursor gradient as well as to put light on the influence of the patterning direction. For this purpose, we deposited 5 test structures along the bottom, right and left edge with a distance of 1 µm to the cavity border. The deposits were placed with increasing distances to each other. Starting with the deposit in the corner, we increased the inter-structure distance from 50 to 80 and finally to 200 nm. Due to the fact that we always referred to the same outer line for all L-shapes, the length of the 7-nested L-structure has to be added to the inter-structure distance to obtain the

distances between the measurement points. We changed the pattern by removing the tail of the single lines resulting in a structure length of 500 nm (see Figure 19). With the adapted pattern, the area that could possibly induce any proximal effect for the neighbouring structure can be increased. The black arrows indicate the fabrication sequence of the L-shapes meaning for the left edge that we started depositing with the L-structure at the top corner continuing towards the bottom and vice versa along the right edge. The test structure at the bottom left corner represents the reference height for calculating the relative heights having an absolute value of 20 nm. By comparing the corner deposition, which are represented by the blue marks, in Figure 25 (a) und (c) we can identify a height reduction of 5-10 % from the top to the bottom deposits. This means that there are favoured deposition conditions at the bottom of the cavity. The only difference between those two patterning spots is the position of the Al frame of the cavity in relation to the GIS outlet and the patterning spot. At the top, the Al frame strikes a shadow for the precursor molecules leading to a reduced precursor density in the proximity of the frame (shadowing effect). Whereas at the bottom the Al frame act as mirror for the molecules resulting in a higher precursor coverage. We call this phenomenon a bouncing effect.

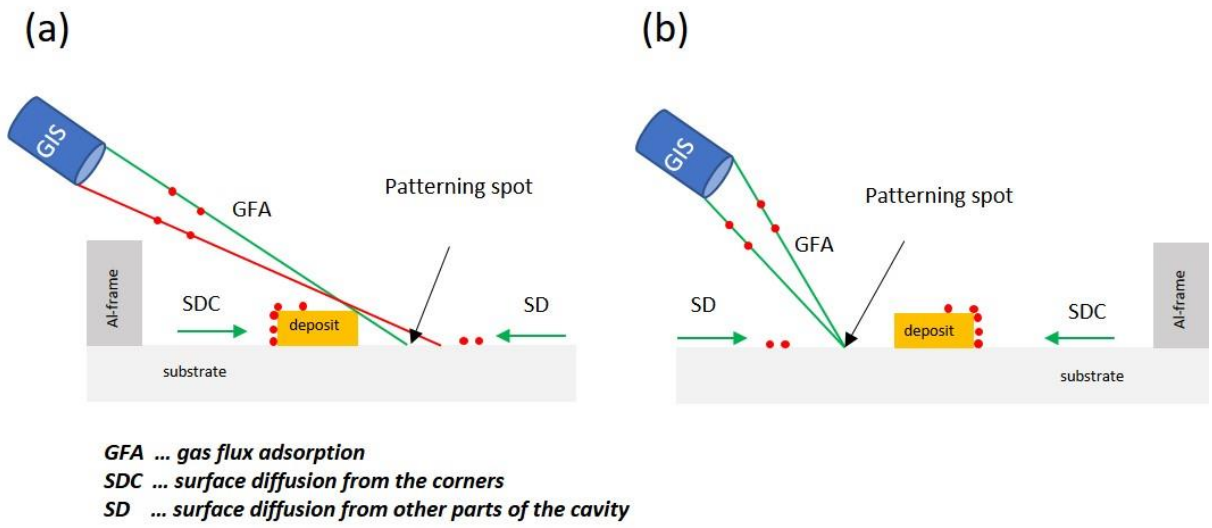

Figure 26: Schematic explanation to demonstrate the impact of different patterning strategies on the precursor replenishment mechanisms. a) patterning away from the GIS inducing a shadow for the precursor molecules emanating from the GIS; b) patterning towards the GIS to avoid a shadowing effect.

Moreover, we can observe a significant height decrease along the edges by increasing the distance to the corners, which can be clearly seen in Figure 25 (a), (c) and (d). The rapid height decrease indicates a significantly stronger precursor accumulation in the corners than along the edges considering that the distance of the measurement points of the corner deposition and the one next to it is only 550 nm. Furthermore, a distinct split of the height reduction from 17 % (Figure 25 (d)) to 7 % (Figure 25 (a)) between the edge deposit and the one next to it could be identified in different areas of the cavity. The decrease from the second nearest to the third nearest from the corner is very similar along all edges having a value in the range of 3-5 %. By further increasing the distance to the corner a height convergence can be identified leading to identical values for the fourth deposits from the corner independently from the alignment within the cavity. Consequently, we can deduce that the precursor situation along all edges is similar and that the bouncing effect is locally confined to the corners

(Figure 25 (d)). By comparing the heights of the structures having the biggest distance to the corner with a deposit in the middle of the cavity (chapter 4.1.1) we can spot negligible variations of ± 1%. Therefore, we can conclude that the prevalent precursor gradient is originating mainly from the favoured accumulation in the corners and that the influences from the edges only play a minor role.

In previous works Winkler et al.[54,57] demonstrated the decisive impact of the patterning sequence on the precursor replenishment and consequently on the deposition behaviour. Before discussing the impact of the patterning sequence, we have to take a closer look on the replenishing mechanism in our experimental setup, which can be mainly separated into three parts: 1) Gas flux adsorption, 2) Surface diffusion from the corner, 3) Surface diffusion from other parts of the substrate. By changing the deposition direction along the two vertical borders indicated by the black arrows in Figure 25 (b), the influence of different patterning strategies on the replenishment should be revealed. On the left side the top structures were deposited first, representing a possible barrier for the directly impinging precursor molecules from the GIS (Figure 26). However, we were not able to observe a significant difference in the declining curve in Figure 25 (a) and (c). Consequently, we can deduce that the geometric shadowing effect of an L-structure with a height of around 20 nm does not have a strong impact on the replenishment mechanism for a structure distanced 50 nm or further away.

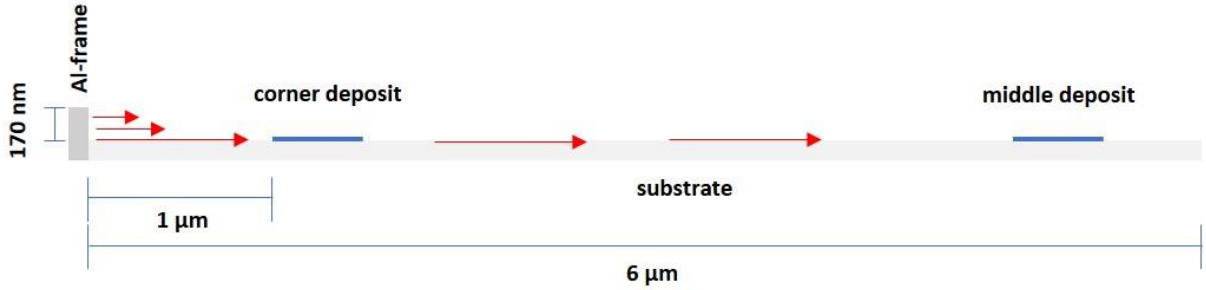

Figure 27: True to scale scheme of a sectional view of the cavity. On the left we can see the Al-frame with a height of 170 nm. The substrate in this scheme protrudes 6 µm towards the centre to highlight the geometrical proportions. As discussed above the source of the gas gradient is close to the Al-frame indicated by the red arrows.

The geometrical constraints for the replenishing mechanisms based on surface diffusion are identical for both deposition directions. Subsequently, we expect that the predominant precursor supply within a morphological cavity originates from surface diffusion from the corners. However, further experiments have to be conducted to provide a clearer picture on the share of each replenishment mechanism in patterning areas with a morphological induced precursor boost, like a cavity.

Summarizing, we can conclude that there is strong lateral gas gradient inside a morphological cavity and that the gradient can be assigned to two effects: 1) Distinctively higher precursor accumulation in the corner regions; 2) Favoured precursor situation in front of the cavity wall that face the directed gas flux. In order to counteract the inhomogeneous patterning conditions these effects have to be taken into consideration by adapting the number of pattering cycles in areas with higher precursor coverage or by completely avoiding these areas.

For the purpose of visualizing the extraordinary nature of the above described phenomenon, a real in-scale sectional view of a scheme comprising parts of the Al frame and the substrate, and two deposits are shown in Figure 27. Compared to the lateral expansion of the cavity, the dimensions of the Al-frame seem to be negligible. It seems very likely that the precursor density close to the edge is of such an exceptional high magnitude that multilayer adsorption processes have to take place.

Sanz-Hernández et al.[58] have profoundly discussed precursor adsorption beyond the Langmuir model and stated that on heterogeneous substrates the probability of multilayer adsorption is favoured. Possible reasons for heterogeneity close to the frame are residues of the photoresist, which was used during the cavity fabrication, discontinuous layers of Aluminium that protrude from the frame towards the centres, which were generated while the Aluminium evaporation process or simply the morphological edge. However, a closer investigation of that phenomena would go beyond the scope of this thesis.

4.1.3 Boosting the Local Precursor Coverage

In order to further shift the FEBID working regime towards the RRL regime, we tried to boost the precursor coverage by reducing the distance between the GIS and the substrate from 50 µm to 5 µm. As a result of lowering the GIS, we expected a stronger precursor flux on the substrate and an increased share of the gas flux adsorption on the precursor replenishment mechanism (see Figure 26) involving a higher and more uniform gas coverage across the cavity.

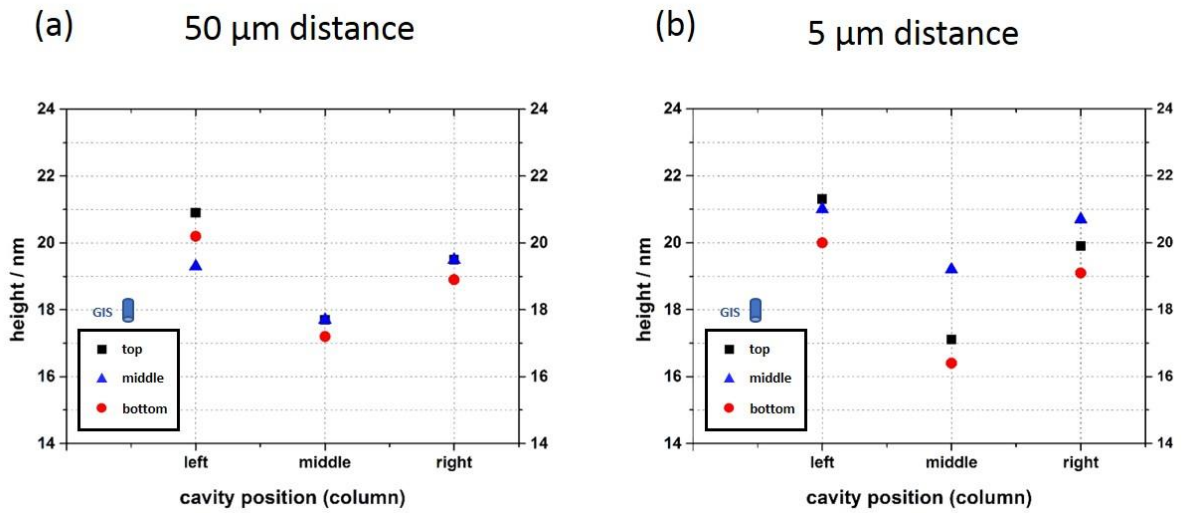

Figure 28: Structure heights at varying positions within a morphological cavity for different GIS to substrate distance: a) 50 µm distance; b) 5 µm distance. A significant split of the heights within the middle column can be observed in b) indicating a less uniform precursor distribution within the cavity.

The experimental design comprised nine L-shaped test structures placed symmetrically in a matrix of three rows and three columns and keeping a minimum distance of 1 µm to the Al-frame. This design was chosen to achieve a reliable statement on the overall gas situation within the morphological

window. The reference deposition was carried out at a distance of 50 µm as in the previous experiments.

For a distance of 50 µm we can again observe a distinct gas gradient throughout the cavity, which is depicted in Figure 28 (a). On the left, we can identify higher deposits in the bottom and top row, which coincides with the stronger precursor accumulation in the corners that could be already found in the previous chapter 4.1.3. Especially noteworthy is the uniformity of the structure heights within the right columns. This signifies an akin accumulation preference along the edges and in the corners, which could not be spotted in 4.1.3. However, the middle column does not follow this trend as the middle deposits, which is missing the edge influence, shows a similar height than the deposits further outside.

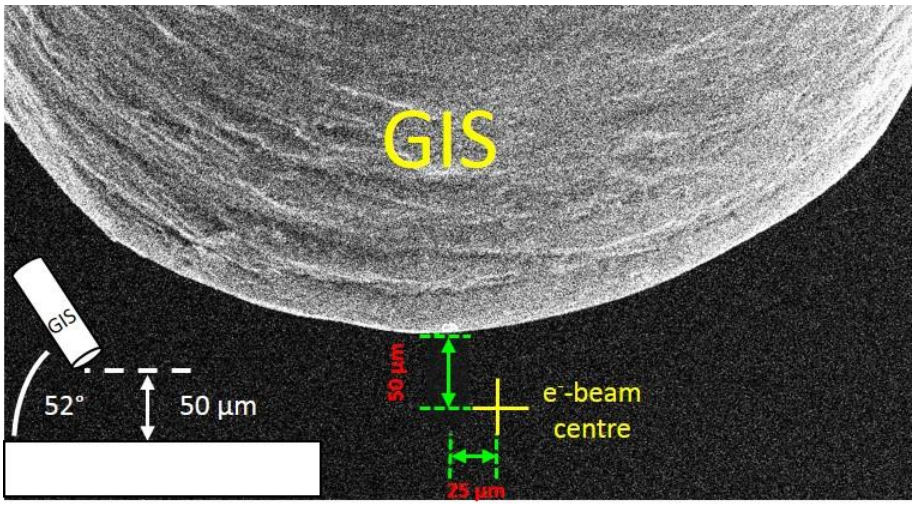

Figure 29: Top-view SEM image of the GIS alignment including side-view schematic of the setup at the bottom left corner. The GIS distance was varied between 50 µm and 5 µm.

By comparing Figure 28 (a) with (b), we can identify a significant splitting of the structure heights in the middle column when the GIS is lowered towards the surface. However, this finding could not be verified with the gas flux simulator introduced by Friedli et. al[59,60], which is simulating the laterally resolved precursor adsorption from the GIS in dependence of various parameters like the nozzle diameter, the angle and distance to the surface and parameters related to the precursor properties. By using the parameters from our GIS arrangement shown in Figure 29 with varying substrate distances, a representation of the patterning conditions should be achieved. In contrast to our assumption, the simulations do not point out a significant difference of the laterally resolved flux ratio J/J_{TOT} as depicted in Figure 30 (a) and (b). This outcome encourages the very complex gas dynamics inside a morphological cavity. To provide simulation results with a closer correlation to the real deposition situation, a more comprehensive approach with an adapted substrate morphology has to be followed.

Apart from the deposit in the middle, no other structures do experience a strong deviation compared to the larger distance. So, we couldn't achieve any improvement of the overall uniformity. We assume that this result can be assigned to the vast share of the precursor replenishment from surface diffusion from the corners and edges. So, the impact of the increased gas flux density is confined to a relatively

small centre area. Consequently, the overall gas gradient couldn't be lowered by compensating the higher density in the corners by an additional accumulation spot in the centre. Furthermore, the expected boost of the precursor coverage leading to a distinct increase of the vertical growth rate failed to appear.

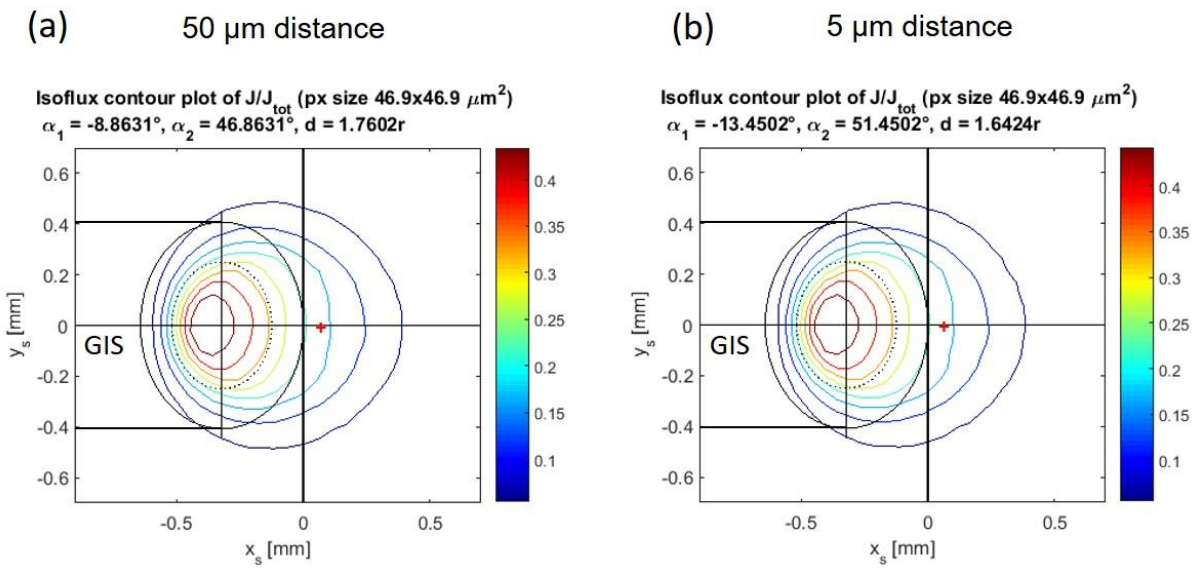

Figure 30: 2D-Precursor surface distribution obtained with the gas flux simulator 59 with varying GIS to substrate distances: a) 50 µm; b) 5 µm. The projection of the GIS outlet is indicated by the black ellipse; the red cross symbolizes the centre of the electron beam.

We have learned that a smaller GIS distance counteracts with our primary goal of achieving better uniformity of the gas density. Also, the desired boost of the vertical growth rate could not be found. As a further reduction of the GIS-substrate distance would enhance the undesired effects due to the geometrical constraint, we decided to stick to the distance of 50 µm for all following depositions since it appeared to be a good trade-off of high and uniform contribution of the gas flux adsorption to the overall precursor coverage.

4.1.4 Summary: Influence of a Morphological Cavity

So far, we gained comprehensive insight of the precursor dynamics inside a morphological cavity. We successfully confirmed the increased vertical growth rate inside the window already found by Haselman[51] in previous works. The precursor coverage enhancement led to the desired shift towards the RRL regime, which is necessary for fabricating the aimed plasmonic structures with highly challenging dimensions.

Beyond that, by observing structure heights at different positions in the cavity we were able to assign the strong gas gradient to the precursor accumulation in the corner regions. A reduction of the vertical distance of the nozzle to the substrate from 50 µm to 5 µm did not distinctively improve the vertical

growth rate and led to an overall less uniform precursor coverage. Hence, we decided on a GIS to substrate distance of 50 µm for the following experiments.

However, by looking at the dimensions of the cavity, the massive change on the deposition behaviour induced by the modified morphology in the proximity of the patterning area still provides some ambiguities. A more detailed insight on the proximal influence on the precursor dynamics due to varying morphologies will be subject for further investigation in future works.

By taking the findings of the cavity influences into consideration, we will be able to create patterning strategies in a way that we can achieve homogenously high deposits across the whole patterning area. In particular, we can change the number of patterning cycle dependent on the position or completely exclude the regions with non-uniform precursor coverage.

4.2 Plasmonic Pill Arrays

Plasmonic structures reveal the perspective of manipulating phase, polarization and amplitude of electromagnetic waves in dependence of the structure dimensions[4]. Following this motivation, we fabricated pill arrays, which are supposed to act as filters for light in the visible range. In order to experimentally validate the predicted plasmonic activity, subsequent optical measurements via near field-microscopy[55] were conducted. Since these measurements record the amount of transmitted light, opaque substrates were necessary. To confine the testing light beam and to reduce background noise, an Au-mask framing the pill array was introduced. For the purpose of preventing electrical charging induced by the impinging electron beam during the deposition, the substrate surface requires electrical conductivity. Therefore, the opaque substrate was built up out of a glass body covered by an ITO layer (15-25 Ω/sq.). A schematic overview of the deposition setup is depicted in Figure 31.

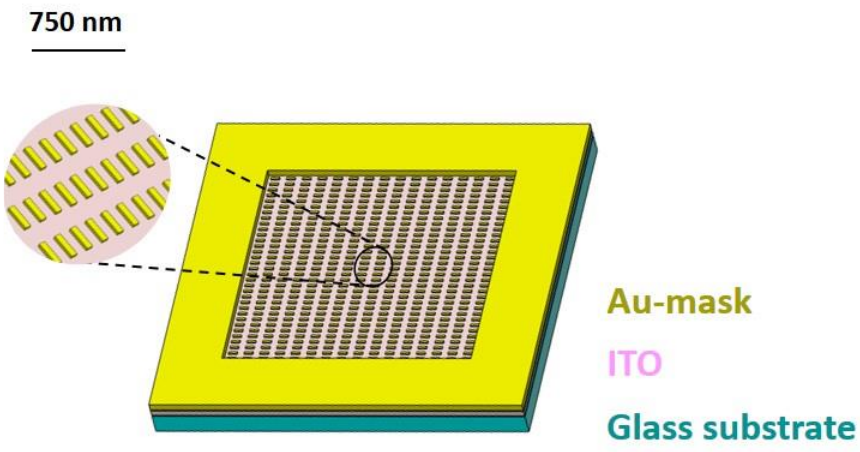

Figure 31: Schematic overview of the 10 x 10 µm² patterning area framed by an Au-mask with a height of 140 nm. The transparent substrate material comprises a glass body covered with an ITO-layer to provide electrical conductivity. Inside the cavity a pill array is deposited, which act as a filter for wavelengths in the optical range.

By simulating the optical response of different pill geometries by the work group of Prof. Roskos at the Goethe University Frankfurt, the dimension shown in Figure 32 (a) turned out to coincide with the desired filtering behaviour. The requirements on the pill dimension included a length of 65 nm, a width of 25 nm and a height between 5-10 nm after purification. Since the purification process is accompanied with a height loss of about two thirds[51], the desired pill height after deposition is above 15 nm. Due to the intrinsic Gaussian deposition shape in the RRL regime, which is accompanied with rounded top edges, the accurate deposition shape was included as an input parameter for the underlying simulations. As the pill dimensions demand upmost precision throughout the whole array, the knowledge about the precursor dynamics gained in chapter 4.1 emerged to be crucial. Considering that the fabrication of plasmonic structures with similar dimension could not be achieved during earlier works of our working group[51,52], this task turned out to be highly challenging.

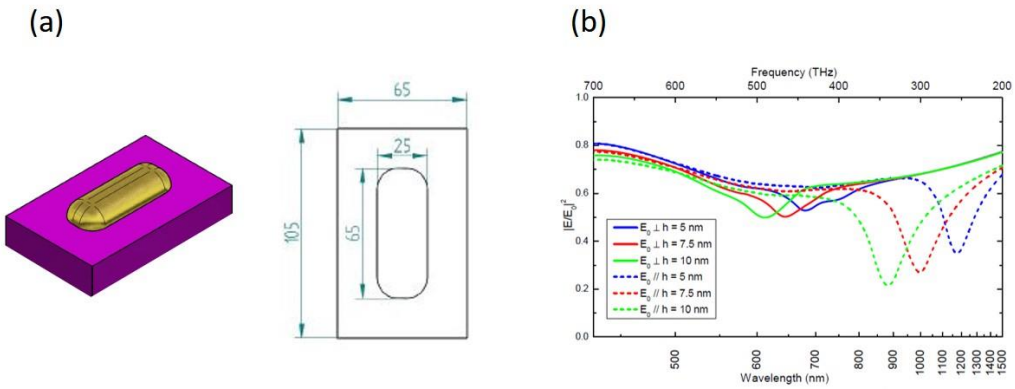

Figure 32: (a) The aimed dimension of the pure gold pills includes a structure length of 65 nm, a width of 25 nm and a height between 5-10 nm with rounded edges with a curvature of 10 nm. (b) The simulations conducted by the group of Prof. Roskos revealed a strong plasmonic resonance for these pills arranged in a large-scale array. Due to the rectangular shape of the structure, the amplitude and positions of the resonance changes significantly by varying the polarization direction of photons. Moreover, the pill height strongly correlates with the resonance behaviour.

The position and amplitude of the adsorption peaks shown in Figure 32 (b) exhibit a strong dependence on the polarization direction. This polarization dependence can be explained by the asymmetric pill shape, which induces different transverse and longitudinal plasmon modes[61]. Moreover, the resonance peaks experience a significant shift by small height deviations. Consequently, the pill height distribution demands maximum uniformity throughout the whole array in order to observe a sharp resonance behaviour.

As an initial step towards the large-scale array, we will start with the fabrication and optimisation of single pills. This will be followed by developing advanced patterning strategies to achieve in-field height variations of ± 1 nm. All depositions, expect those in chapter 4.2.8 determined for subsequent optical measurements, were conducted on a Silicon test substrate inside an Aluminium cavity as described in Figure 22. The pill arrays for plasmonic validation (chapter 4.2.8) were fabricated on a transparent glass-ITO substrate as depicted in Figure 31.

4.2.1 Single Pills

After the successful shift of the process parameters towards an RRL regime and getting a profound insight of the precursor dynamics inside a morphological window (see chapter 4.1), we inherited this knowledge for the fabrication of single pills. Therefore, the DT was kept at 10 µs for 1000 exposure cycles resulting in a TET of 10 ms. In order to reach the required dimensions of the high-fidelity deposits, we chose a patterning design, which is shown in Figure 33 (a), consisting of 6 points with a distance of 10 nm from each other. The marginal change of the PoP from 9 nm for the L-structures in chapter 4.1 to 10 nm for the pills is a result of the structure size and not based on considerations about the deposition behaviour. By adding half width of the outer deposition points to the distance of 50 nm between the patterning points, we except to meet the targeted pill size of 65 nm.

Following the suggestions by Winkler et al.[62], who demonstrated that the vertical growth rate is highest when patterning is performed towards the GIS, the patterning direction was aligned towards the nozzle, which is indicated by the blue arrow in Figure 33 (a). For the purpose of decoupling the in-pill deposition performance from any proximal impact of neighbouring structures, we chose an inter-structure distance of 200 nm. Moreover, we conducted the patterning in the centre of the cavity to neglect the impact of precursor gradients. The results are depicted as an AFM height image in Figure 33 (b). For closer investigation, we took a cross section of one pill across the vertical and the horizontal directions indicated by the blue and black arrows, respectively, in Figure 33 (b).

Firstly, we identify a significant reduction of the height compared to the L-structures in Figure 23. While an equally positioned L-structure with the identical patterning parameters is having a height of 17 nm, the pills reveals vertical dimensions of 7-9 nm (Figure 33 (c)). Since the patterning parameters were inherited from the previous chapters, the change of the vertical growth rate can be attributed to the structural design itself. Whereas the L-structure is built up of 515 patterning points, the pills are composed of only 6 points. During one pass the numbers of patterning points is scanned by the electron beam. Consequently, this leads to a decrease of the time between two electron beam pulses at a particular deposition point from 5140 µs to 50 µs and hence, to a dramatically shortened duration for the precursor molecule replenishment. The shortage of precursor molecules is accompanied with a shift to the MTL regime leading to decreased vertical growth rate (Figure 33 (c)) and increased lateral growth rate visualized by changes of the FWHM from 27 nm to 21 nm (Figure 33 (d)).

Secondly, a significant height asymmetry was spotted in Figure 33 (c) that could be assigned to the first shot effect. This effect describes an increased growth rate at the position where the electron hits the surface first since the highest precursor density is present before patterning starts. Furthermore, the outer patterning spots experience favoured precursor replenishment as the geometrical constraints enable direct diffusion from the substrate from three sides whereas for the inner patterning spots the diffusion is limited to two spatial directions.

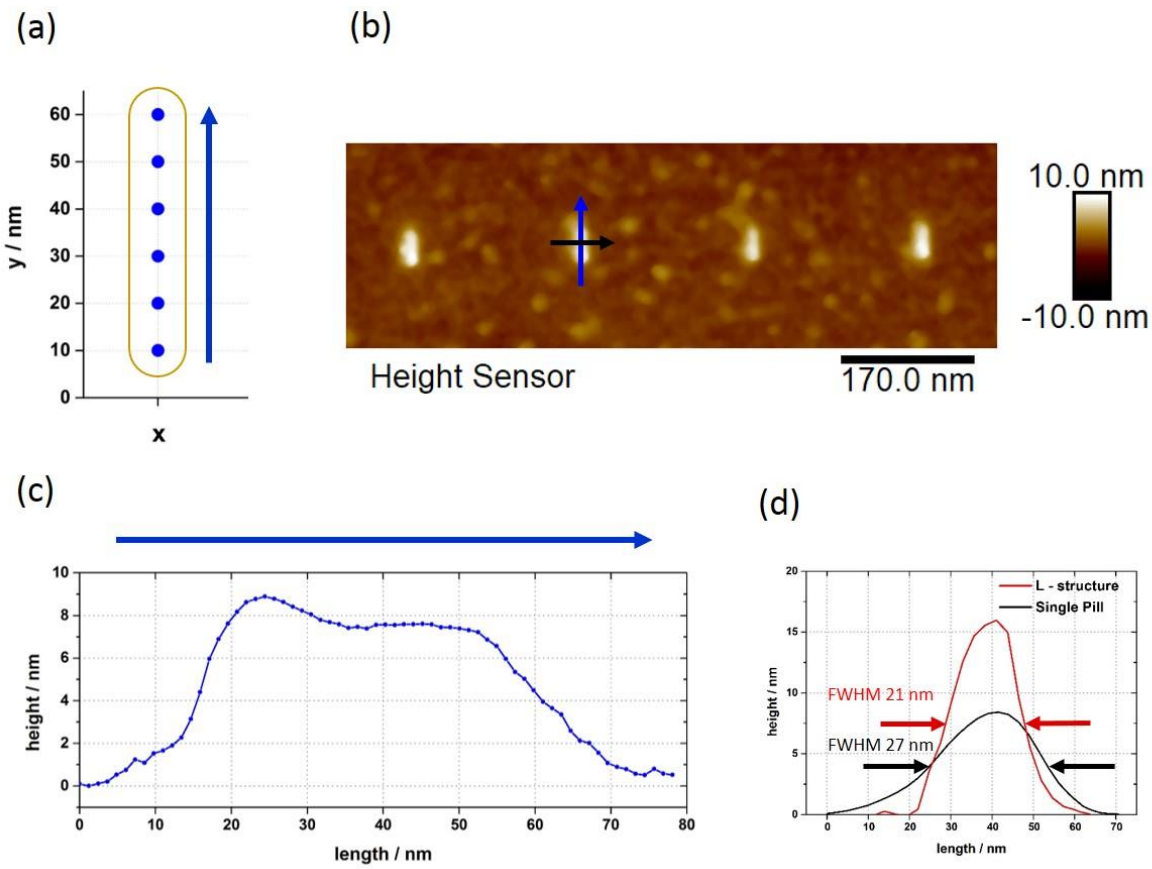

Figure 33: (a) Schematic patterning sequence of a single pill consisting of 6 points distanced 10 nm from each other. The framing gold line is indicating the dimensions of the deposited pill. The blue arrow shows the patterning direction, which is aligned towards the GIS. (b) AFM height image of 4 pills with a distance of 200 nm from each other. Foreign particles can be spotted unevenly distributed across the surface. The blue and black arrows specify the direction of the cross sections depicted in (c) and (d), respectively. (c) Cross section along the blue arrow in (b) revealing a pill height of 7-9 nm and an asymmetric height distribution. The asymmetry is caused by higher precursor coverage at the first deposition point (first shot effect). (d) Cross section along the black arrow in (b) (black line) and along the outer line of a L-structure deposited with a DT of 10 µs inside a cavity (Figure 23) (red line). Due to the small number of patterning points coming along with a low refresh time, the vertical growth rate of the pill is drastically reduced compared to the L-structure, which is revealing a height of 17 nm. By comparing the width (FWHM) of the pill and the L-structure, an increase from 21 nm to 27 nm can be seen. The increase of the lateral growth rate portends a shift towards the MTL regime.

We confronted the pill asymmetry with a change to oscillating patterning directions as depicted by the blue arrows in Figure 34 (a). After the first pass towards the GIS, the following pass was carried out averted to the nozzle. As anticipated, the cross section turned out to show the desired symmetry (Figure 34 (b)). Although we can recognize a bowl shape attributed to a first shot effect at both tails, we followed the strategy with oscillating directions since the elevations at the structure ends are less distinct than in Figure 33 (b). Beyond that, a symmetric shape is accorded top priority. Nevertheless, with a pill height of 8 nm the vertical growth rate still does not show the necessary extent. Therefore, we targeted a different patterning approach, which will be discussed in the following chapter.

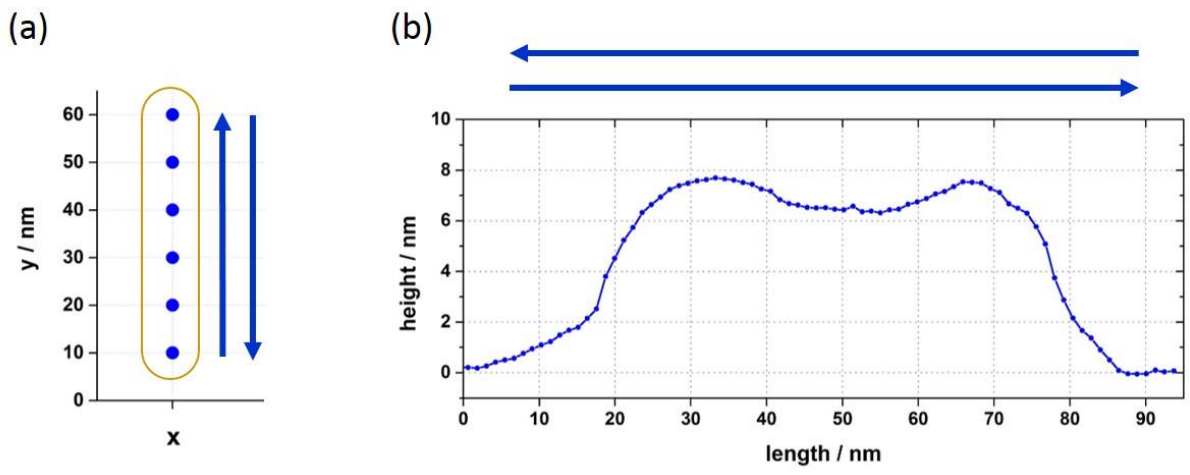

Figure 34: (a) Schematic patterning sequence of a single pill with an oscillating patterning strategy, which is indicated by the blue arrows facing to opposite directions. (b) Cross section along the longitudinal side of a pill deposited with the oscillating sequence. This approach led to a bowl-shaped height distribution with an overall improvement of symmetry.

4.2.2 Pills in a Line Array

The goal of this chapter was to develop a patterning strategy, which enables the increase of the vertical growth rate together with supreme lateral resolution. Hence, the irradiative depletion of precursor molecules within a beam pulse has to be minimized to ensure a shift towards the RRL regime. The total precursor coverage is a convolution of the coverage related to the pulse duration and coverage related to the refresh time. By increasing the refresh time, which is the time between two passes at a particular patterning spot, the number of replenishing molecules and consequently the precursor coverage is raised. As we have already determined the optimum DT in chapter 4.1.1, we introduced a patterning sequence, which ensures a rise of the refresh time. To do that, we increased the number of patterning points during one pass meaning that we expanded the number of pills and hence the number of points, which were irradiated in the course of one patterning cycle. By choosing a line array of 80 pills for one pass, we are able to extent the number of points from 6 points of a single pill to 480, which is close to 515 patterning points of the L-structures where to deposition results were highly satisfying. A section of 3 pills of the line array can be seen in Figure 35. For symmetry reasons, we chose this oscillating patterning strategy for the line array and all coming experiments if not explicitly mentioned differently.

Starting the patterning cycle with the first pill, the electron beam moves to the second pill before the patterning of the second pills starts. The solid and dotted arrows in Figure 35 represent pill patterning and the fast electron beam movement to the consecutive pill, respectively. After the first cycle where the direction is aligned towards the GIS (blue arrows), the second cycle is performed oppositely (green arrows). The inter-pill distance of 65 nm was chosen in accordance to the simulation results for a large-scale array shown in Figure 32.

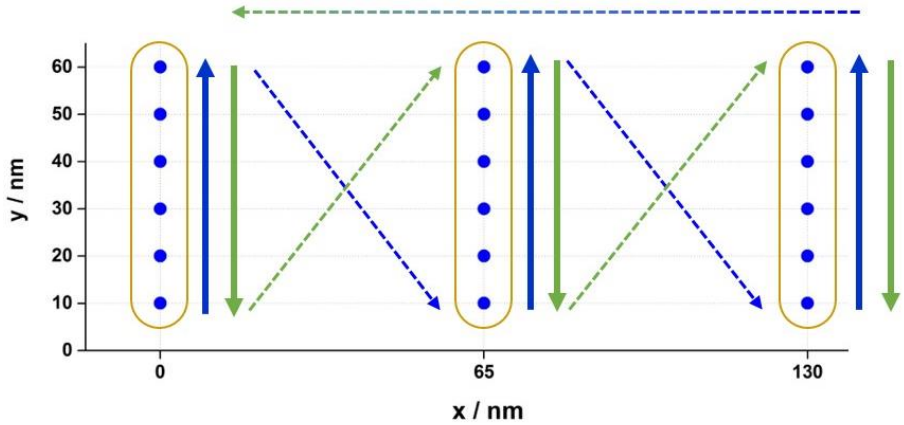

Figure 35: Scheme of a section of a line-array patterning sequence for the deposition of nano-pills. The blue and green colours represent the first and second patterning cycle, respectively. After the first patterning cycle from bottom to top the beam jumps back to the first pill where the patterning is directed from top to bottom. The jump between the cycles with different directions is symbolized by the arrow having a colour gradient from blue to green. As one pass includes the deposition of numerous pills, the electron beam has to move between the structures indicated by the dotted arrows. The solid arrows indicate the alignment of the deposition direction towards the GIS.

The repetition of 1000 passes results in pills arranged in a line array, which is depicted as an AFM height image in Figure 36 (a). By taking a closer look at the cross section along the blue arrow, a tremendous height increase from 8 nm in chapter 4.2.1 to 18 nm (Figure 36 (b)) can be spotted. Moreover, the first shot effect could be resolved due to a homogenously strong precursor coverage within the pill induced by the raised refresh time. However, the cross section along the red arrow in Figure 36 (a) reveals highly undesired residual deposition with a maximum height of 7 nm shown in Figure 36 (c). By comparing Figure 35 and Figure 36 (a) we can identify a conformity of the dotted lines with the shape of the residues in the AFM height image. Therefore, the X-shaped deposits in between the pills can be clearly attributed to the movement of the electron beam between the pills for every pass. While the beam is deflected to the next pill with limited speed, the beam induces dissociation of the precursor molecules and hence, deposition takes place. Since the beam traces between the pills might establish electrical conductivity throughout the array and hence, severely affect the plasmonic resonance, we had to further investigate this issue.

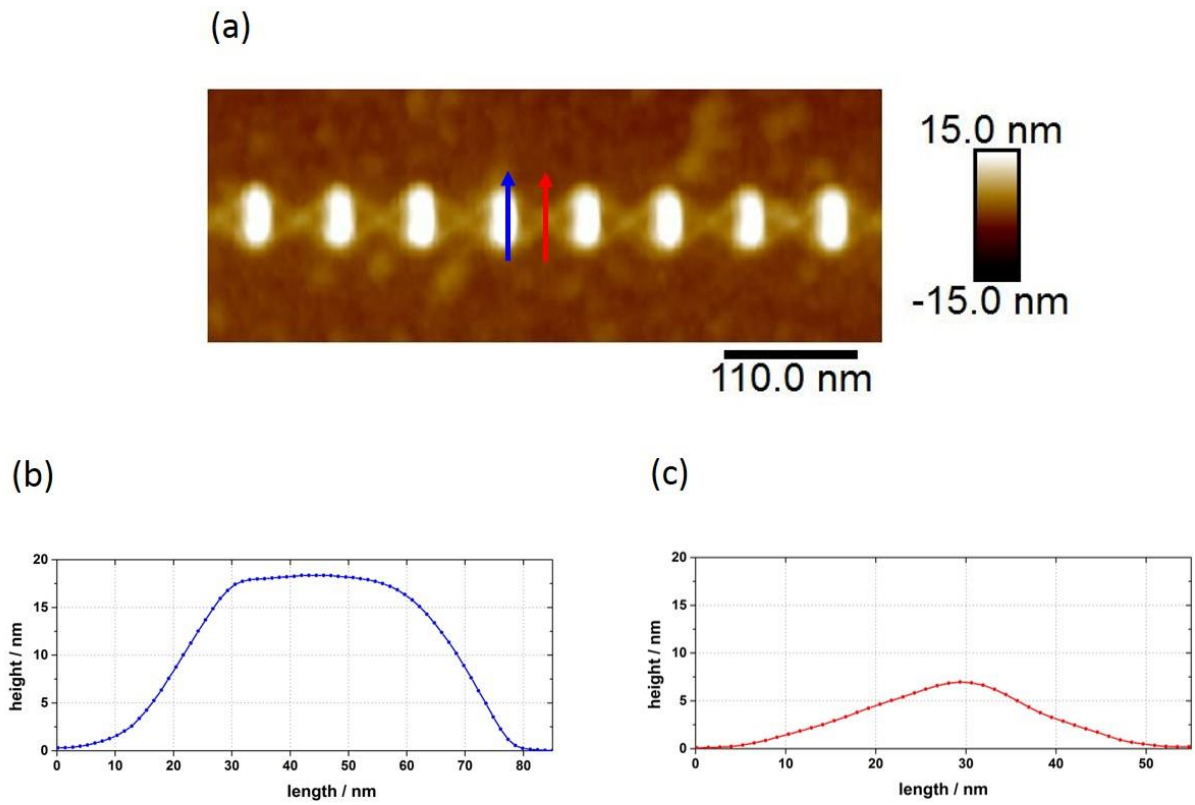

Figure 36: (a) AFM height image of pills arranged in a line-array. The well-defined pills are interrupted by highly unwanted residues for which the cross section along the blue arrow is depicted in (c). By taking a cross section along the red arrow, we can identify a symmetric height distribution with the desired height of 18 nm (b).

4.2.3 Characterization and Prevention of Residual Depositions

To get a profound insight of the unwanted residual depositions, we first chose a patterning layout whose only aim was to clarify the phenomenon of the beam traces. Therefore, the patterning direction in this chapter was kept constantly aligned towards the GIS. Moreover, the patterning layout was arranged in a matrix of 12 pills per line and column and the beam followed an ascending path with changing the direction after every line. The AFM height image of the resulting pill array shows distinct residual depositions between the pills, both within the line and at border of the array when jumping between the lines (Figure 37 (a)). In Figure 37 (b) we can see a close up view of two lines, which were patterned in the opposite direction, namely the lower line from left to right and the upper line vice versa. By taking a closer look, the pills in each line are revealing a lateral twist in the opposite direction according to the in-line patterning direction. Consequently, we can reconstruct the beam movement by considering the lateral twists. Starting at the bottom left corner, the sequence aims to the right bottom corner and continues with the second line aiming to the left and so forth.

The pills in Figure 37 (c) reveal an asymmetric distortion at the bottom, which is highlighted by the black dotted ellipse and by the schematic overlay of the patterning points and patterning direction. In order to move from the left to the right pill, the electron beam first has to be accelerated and

afterwards decelerated when reaching the aimed position. As the shape deviation is only prevalent at the bottom and is tilted towards the prior structure, we deduce that the residence time of the beam is higher at the lower end of the pill compared to the top of the previous while moving from one to the next. Consequently, we can conclude that the beam deceleration time exceeds the acceleration time.

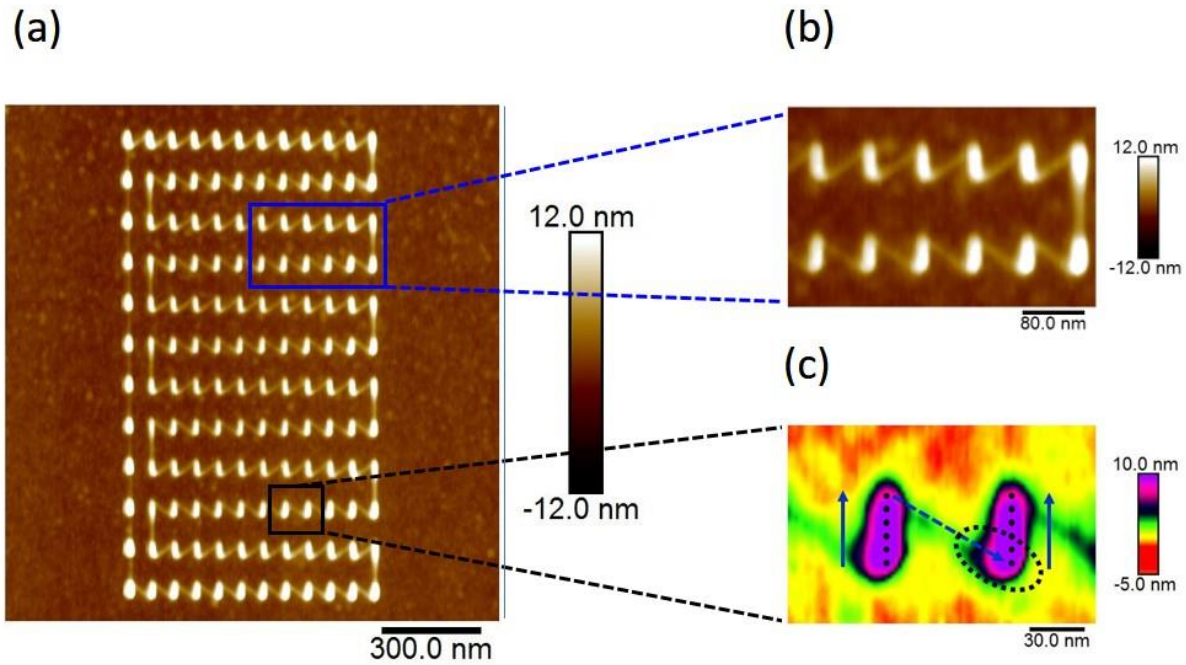

Figure 37: (a) AFM height image of a 12 x 12 pill matrix, which expose a predominant tilt direction of the pills in dependence of the patterning sequence. (b) Close up view of two lines to highlight the lateral twist in accordance to the patterning direction. (c) The pills reveal a distorted pill shape, which can be traced back to a lower beam deceleration than acceleration time. By adding the schematic patterning points and patterning direction the observed deviation is highlighted.

Due to the possible influence of the asymmetric pill shape and the residues on the plasmonic resonance, we had to find a way to fully prevent the secondary deposition during the movement between the pills. Therefore, we installed the beam blanker model PM BEAMBLANKER XL-FEG (VDL Enabling Technologies Group) in our DBM setup. We can think of our beam blanker as a plate capacitor that deflects the electron beam by its electrostatic field. The setting of the beam blanker determines the distance between the capacitor plates. Since the electron beam might be slightly influenced by the blanker while passing the device even though it is not active, we chose the setting where the plates are having maximum distance (blanking position 2). As the charging time of a capacitor is finite, it takes a certain time until a state of full deflection is obtained. We implemented a blanking strategy where the beam was deflected at the top patterning point of the pill and started irradiating the surface again at the bottom of the following pill. Due to the finite time until full blanking is reached, we added an additional pausing/breaking time at two patterning points of interest. So, after sending the blanking signal, the electron beam parked for a predefined time at the top of the first and at the bottom of the following structure where the deposition continued.

We started with a pausing time of 1 µs per blanked patterning point to get a sense of the added component. The AFM height image in Figure 38 (a) still revealed a distinct trace of residual depositions shown by the yellow line between the nanostructures. This means that the time until full beam deflection exceeds the pausing duration. Thus, we increased the blanking time to a significantly higher value of 30 µs to guarantee the absence of residues, which was indeed achieved as depicted Figure 38 (b).

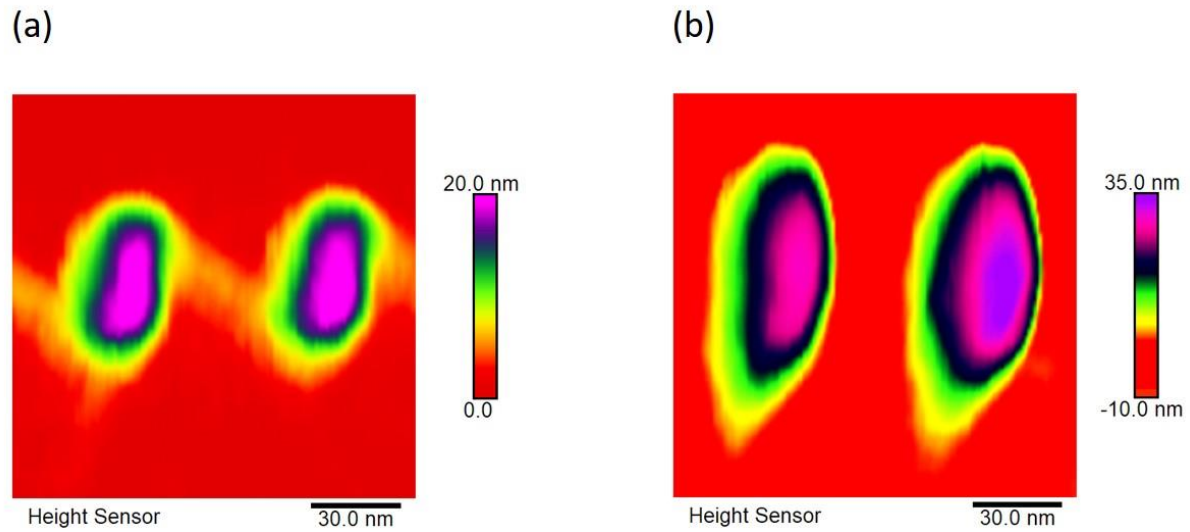

Figure 38: AFM height image of two pills for which the beam was blanked at the top and the bottom patterning point to counteract the residual deposits caused by the beam movement. (a) A pausing time of 1 µs turned out to be too little in order to move the beam in a fully blanked condition from one pill to the next. The still present residues can be spotted by the yellow line connecting the structures. (b) Although, no residual depositions can be identified for a pausing time of 30 µs, the electron beam experiences a significant drift resulting in a distorted pill shape.

However, by getting rid of one problem, the next issue pops up. The nanostructures fabricated with the adapted blanking parameters showed a serious deviation of the expected shape. More precisely, the overall size is drastically enlarged and a drift with a predominant direction to the left is present. Reminding the working principle of the beam blanker, the shape deviation can be explained by a rest charging of the capacitor during the deposition.

For the purpose of receiving a clear picture of the blanking behaviour, we determined the maximum residues height and the deviation of the pill width in dependence of the pausing time. The width deviation was calculated by comparing the pills that were deposited with varying pausing times, with the ones fabricated without any use of a beam blanker (Figure 37 (c)). The variation of the pausing times discloses antidromic graphs for the width deviation and the residues height as shown in Figure 39. By following the blue ascending slope, we can identify an increasing drift of the electron beam with the pausing time. Hence, we deduce that the beam blanker is charging very slowly and keeps charging at least 30 µs. The increasing capacitor charge together with the slow discharging characteristic results in rest deflection when the deposition of the next pill starts. Consequently, the pill shape is steadily worsened at increased breaking times. We expect the capacity and thus the drift

to reach saturation at even longer pausing times. Next to the shape deviation, the slow charging behaviour causes an incomplete deflection accompanied with significant residues for low pausing times. For our purpose, the best trade-off between acceptable residue heights and accurate pill shapes appears to be at 10 µs. Thus, this value was chosen as the blanking parameter for the following depositions.

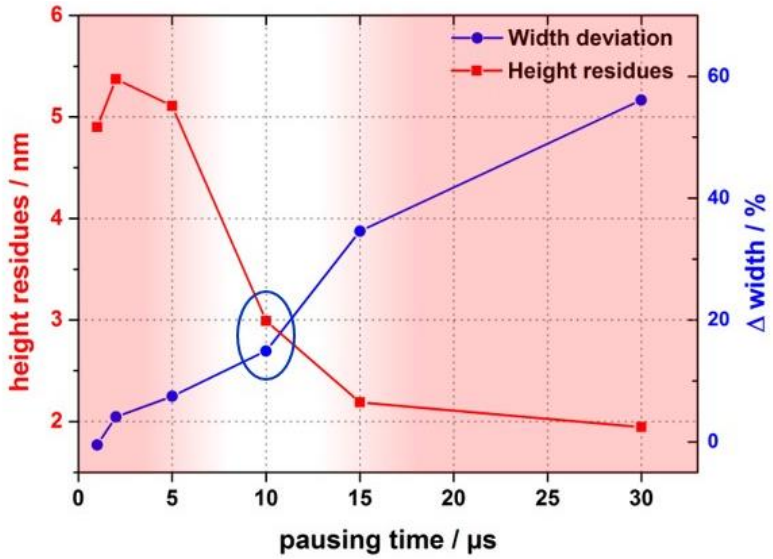

Figure 39: Width deviation and residues height in dependence of the pausing time. Here, the width deviation is defined as the difference of the width of pills that were deposited with varying pausing times, with the ones fabricated without any use of a beam blanker. By increasing the pausing time, the distortion from the initial pill shape with using a beam blanker gets bigger. This can be explained by an ongoing charging of the plate capacitor and a slow charging-discharging characteristic. Moreover, the slow response characteristic of the beam blanker results in distinct residual depositions for short pausing times.

4.2.4 Optimized Pills in a Line-Array

So far, we have identified three major challenges concerning the pill fabrication: 1) Asymmetry due to a single-edge first shot effect; 2) Reduced vertical growth rate caused by shortage of precursor molecules; 3) Residual deposition induced by the movement of the electron beam between the pills. To overcome these issues, we have introduced oscillating patterning directions, we have developed a patterning strategy, which includes numerous pills during one patterning cycle to work in an RRL regime and finally we have installed a beam blanker. By applying all these strategies, we were able to fabricate extraordinary nanostructures, which are depicted in Figure 40. The optimized pill array reveals accurately fabricated nano-pills with highly challenging dimensions. Due to the optimized beam blanking parameters, we managed to prevent severe residual depositions and maintain shape fidelity at the same time. Moreover, Figure 40 (a) highlights the proper repeatability of the pill deposition process since the degree of homogeneity within the shown array segment is apparently very high.

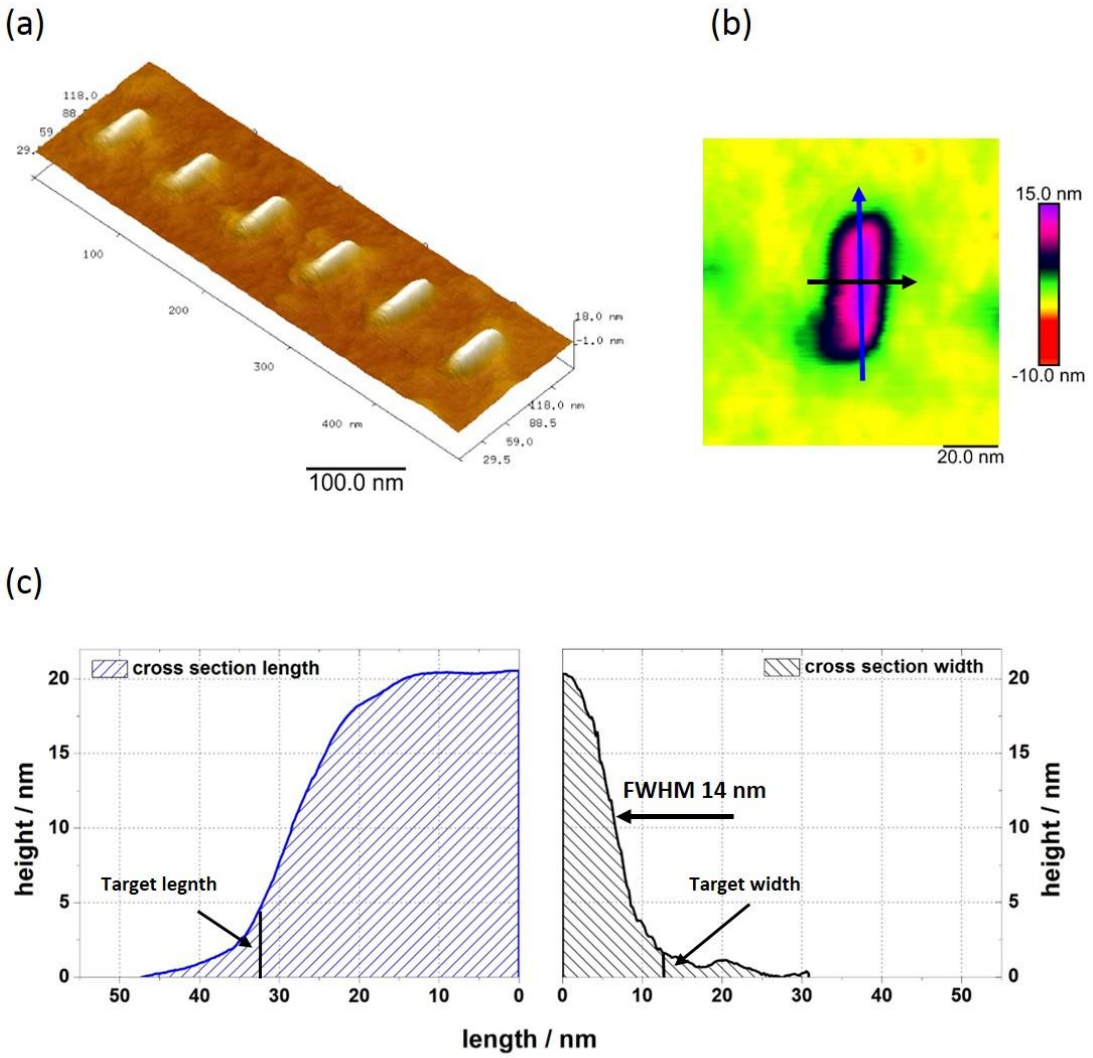

Figure 40: (a) 3D-AFM image of a pill line-array. No distinct residual depositions can be spotted for a 10 µs pausing time of the blanked beam. (b) reveals an accurately shaped pill with a slight drift-related deviation from the desired pill geometry at the bottom left corner. The cross sections to determine the length and width profile is indicated by the blue and black arrows, respectively. (c) Cross section along the blue and black arrow in Figure 40 (b) to determine the length (left) and width profile (right), respectively. The graphs only show half of each cross section. The not shown half of the width is slightly deviated by the instrumentation induced drift. Hence the read-out values for length and width have to be doubled to observe the values for the full structure without deviations through instrumentational limitations. The length profile shows a homogenous distribution with the vast share of the pill volume inside the desired length of 65 nm. The right graph reveals dimension very close to the target width. Furthermore, the FWHM suggests an astonishing value of 14 nm FWHM at 21 nm height.

Nevertheless, the beam drift induced by the rest charging of the beam blanker could not be fully resolved. The left-directed distortion at the bottom of the pill in Figure 40 (b) makes the drift evident. To get a clearer picture on the pill dimensions, we took cross sections along the black arrow to determine the width and along the blue line for the length (Figure 40 (b)). The accuracy of the structure

can be confirmed by the supremely homogenous height distribution along the pill as shown in Figure 40 (c, left). Furthermore, we were able to meet the requirements on the pill length, which can be visualized by plotting the targeted length of 65 nm in Figure 40 (c, left). We can clearly see that the vast share of the total deposited material is within the requirements. The marginal tails, which are exceeding the desired length are owed to the intrinsic Gaussian deposition shape of FEBID.

The cross section of the pill widths shown in Figure 40 (c, right) emerged to be in high accordance with a Gaussian shape indicating RRL conditions for which the highest-resolving structures can be obtained. In our case, the drift-corrected FWHM has an astonishing value of 14 nm at a height of 21 nm which results in an **aspect ratio of 0.7**. Although this value is utterly impressive, setup adaptions are necessary to confirm this result experimentally since the summation of the not shown half, which is widened due to drift issues, and the shown half results in a FWHM of 22 nm. The drift-corrected base width highly coincides with the aimed base width of 25 nm. Although, the pills still show small deformations, we brought out the best possible result as the beam drift is induced by technical limitations and hence, can't be optimized at this point with our current instrumentation.

4.2.5 Pills Arranged in Block Arrays

After optimizing the fabrication of small-scale pill arrays, the next task concerned the development of sequencing strategies for large-scale arrays, which are supposed to perform the plasmonic resonances illustrated in Figure 32. The main focus was put on achieving homogenously distributed pill dimensions throughout the whole array as this is a major requirement for observing a maximum plasmonic response. The targeted 8 x 8 μm^2 pill array was divided into blocks with a size of 1.3 x 0.8 μm^2, with each block comprising 144 pills arranged in a 12 x 12 matrix (Figure 41 (b)). The patterning direction faced the GIS and went upwards in serpentines. In Figure 41 (a), we can see a segment of the large-scale array subdivided into blocks. The motivation of the chosen layout was to minimize the influence of a potential stage drift since this would cause additional widening of the pill width. On the one hand, it is favourable to increase the loop time in order to deposit in RRL regime. On the other hand, the impact of a stage drift is vastly enhanced by longer pass times. That's why multipass strategies often have been avoid for high-resolution depositions[53]. However, due to the desire to fabricate in RRL regime, the aim was to decrease the duration of one patterning cycle to a value where the effect of the stage drift is marginal and where the loop time is sufficiently high to ensure deposition in RRL regime. By dividing the whole array into smaller parts, the duration of one patterning cycle was strongly reduced. Depositing a block of 144 pill with a DT of 10 µs results in a patterning cycle with a duration of 1440 µs. In contrast, the fabrication of the whole array without the partition leads to a pass duration which is the product of the block patterning time multiplied by the number of blocks. In order to investigate the patterning performance with the changed sequence, we first deposited a single block.

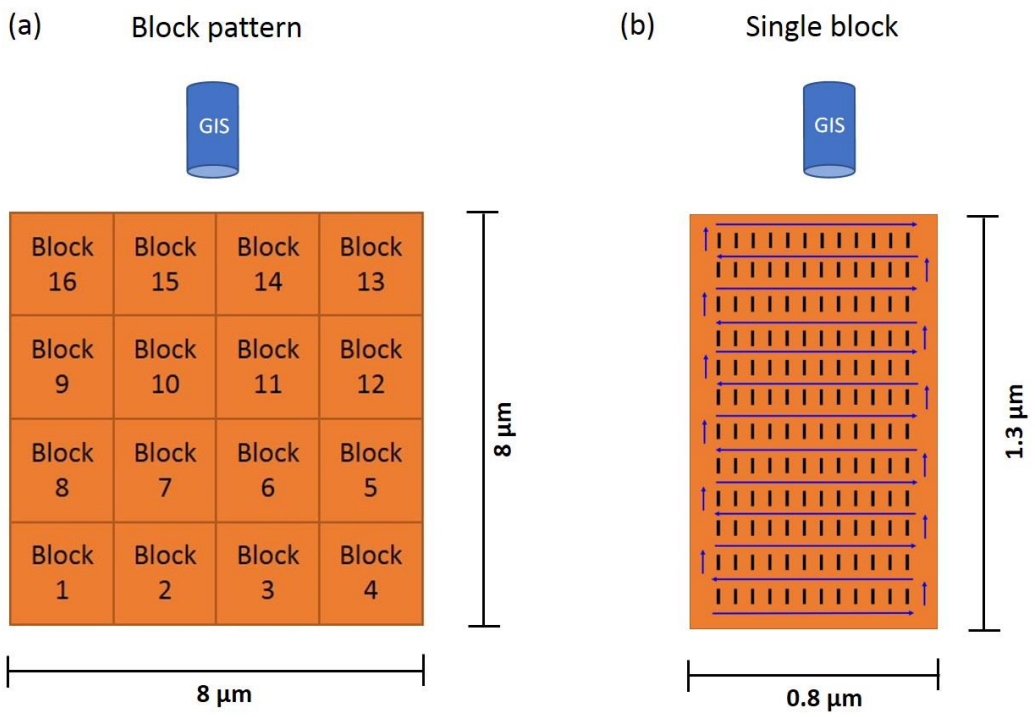

Figure 41: (a) Schematic large-scale array, which is divided into blocks to minimize the influence of a potential stage drift. (b) True to scale single block consisting of 144 pills arranged in a 12 x 12 matrix resulting in a block size of 1.3 x 0.8 µm^2.This block is used for experimentally validating the approach of dividing the large-scale pattern into blocks.

The 3D-AFM height image is depicted in Figure 42 (a) and reveals a clearly pronounced bowl-shaped height distribution. Since the aimed plasmonic behaviour demands high degree in-field homogeneity, the observed distribution is not acceptable. Surrounded by the tallest pills, the heights are constantly falling while moving to the centre of the pattern. The quantitative analysis was conducted by taking a cross section along the blue arrow. Hereby, a height drop of 35 % between the first outer pills and the 5th- 7th pill from the left can be disclosed (Figure 42 (b)). This effect can be assigned to the fact that during multi-pass deposition the lines deposited further outside present a hindrance for the precursor molecules to diffuse to the central pattern areas. However, we did not expect that the morphological border of the deposits further outside have such a tremendous impact on the inner structures as the pill dimensions are marginal. To get a further insight in the precursor dynamics we correlate the increase of the surface distance induced by the nano-structures with the change of the deposition performance. As seen in Figure 42 (b) the distance that an adsorbate has to diffuse in order to reach the second pill from the left is raised by 3 nm due to the presence of the left-most pill. To move all the way to the centre of the patterning area, the molecules have to overcome additional 20 nm. The height drops 10 % from the left-most to the following pill and even 35 % to the central structure. Considering these vanishingly small changes in diffusion distances, it is very unlikely that the bowl-shaped-height distribution is exclusively morphologically induced.

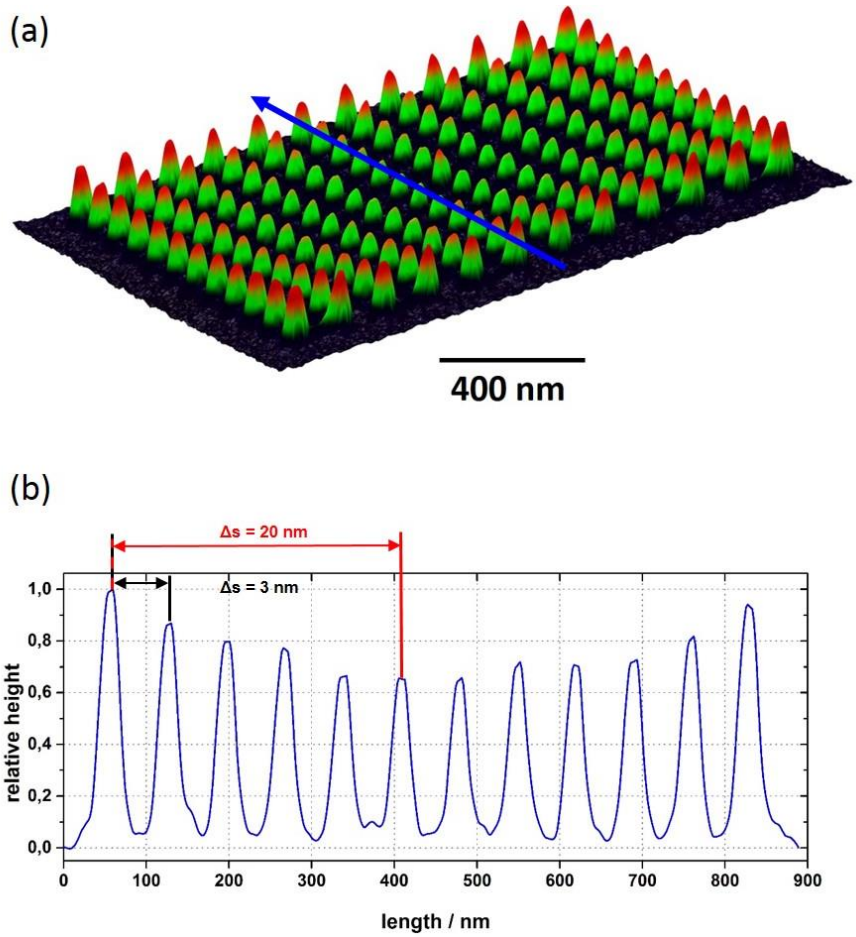

Figure 42: (a) 3D-AFM height image of the 12 x 12 pill pattern revealing a significant bowl-shaped height distribution. The fence of outer pills experiences favoured precursor replenishment, whereas the outer pills represent a hindrance for the precursor surface diffusion which leads to smaller heights in the centre. (b) By taking a cross section along the blue arrow in (a), a height drop of 10 % from the left-most to the second furthest outside placed pill and a drop of 35 % to the central structures is spotted. The increase of the surface distances for the diffusive precursor molecules is only 3 nm to the second pill from the left and 20 nm to a central deposit compared to a flat surface without any structures. Hence, the inhomogeneous height distribution can not only be attributed to the morphological barrier.

Winkler et al. have found a diffusion length of the Platinum precursor $(CH_3)_3$-Pt-$CpCH_3$ on Silicon, which is less than 25 nm[62]. An exact value for the diffusion length of the $Me_2Au(acac)$ precursor for gold deposits was not determined in literature. However, we assume a value in similar range to the Platinum precursor since the growth dynamics of the Gold precursor is similar to the Platinum precursor. Moreover, the framework conditions are identical to the ones used during the determination of the diffusion length for the Platinum compound. Hence, we presume that the extenuated precursor coverage in central areas are partly provoked by a changed sticking coefficient on the deposit compared to the substrate. This could lead to heavily changed diffusion length and therefore, could induce the observed height distribution, which is highly unwanted for the aimed plasmonic application. Therefore, a different patterning approach resulting in homogenously distributed arrays has to be found.

4.2.6 Line per Line Patterning for Large-Scale Arrays

In the following section, we went one step further back and applied the approved line-sequencing used in chapter 4.2.2 for large-scale pill arrays. The challenge was to outlay the patterning strategy in a way that the number of pills per patterning cycle is high enough to ensure an adequate refresh time in order to deposit in the RRL regime and to keep the cycle duration sufficiently low at the same time to minimize the impact of a potential stage drift, which is increasing with the cycle time.

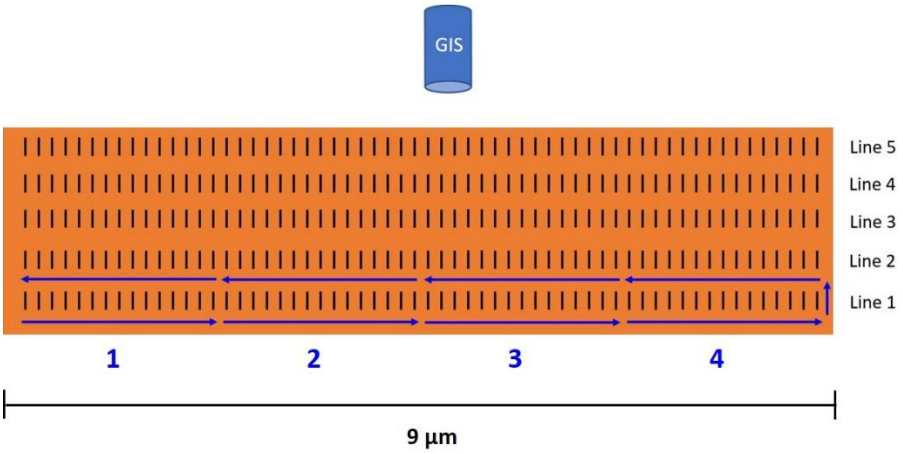

Figure 43: Patterning strategy for a large-scale pill array, for which a single line is divided into four parts. Each part is represented by a blue arrow. The patterning direction is facing the GIS and proceeding towards to GIS in serpentines. Since the pill geometry is utterly small, the scheme dimension is not true to scale.

Therefore, we decided to divide a single line having a length of 8 µm and consisting of 120 pills into four parts. Considering 6 patterning points per pill and 30 pills per cycle, the total number of patterning points per cycle was 180 which means a reduction of 300 points compared to chapter 4.2.2.

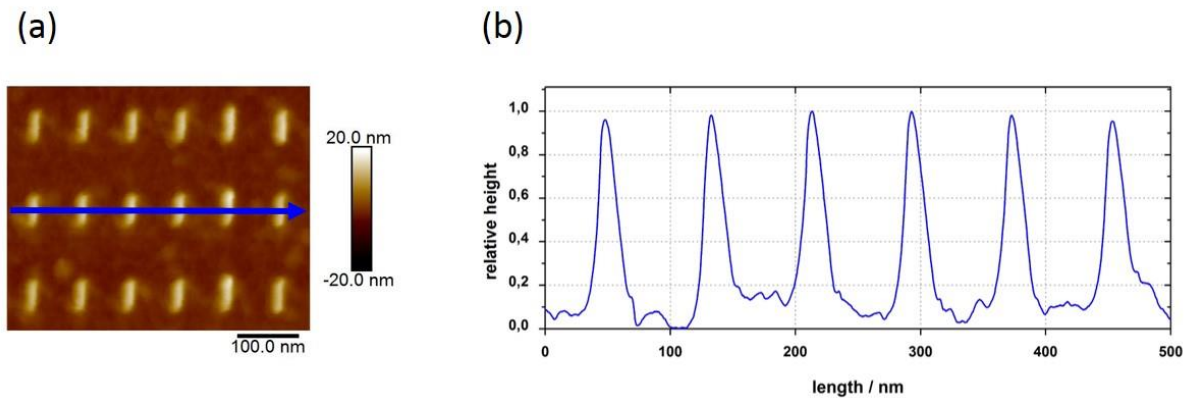

Figure 44: (a) AFM height-image of a large-scale pill array section to experimentally validate the above introduced patterning strategy. (b) The cross section along the blue line in (a) reveals remarkable in-field height homogeneity with variations of ± 2 % at an absolute height of 15 nm.

Nevertheless, the time for precursor molecules to replenish was sufficiently with an adequate pill height of 15 nm. Furthermore, the cross section reveals an extraordinary height homogeneity with a negligible in-line variation of ± 2 % at 15 nm height within a section as illustrated in Figure 44 (b).

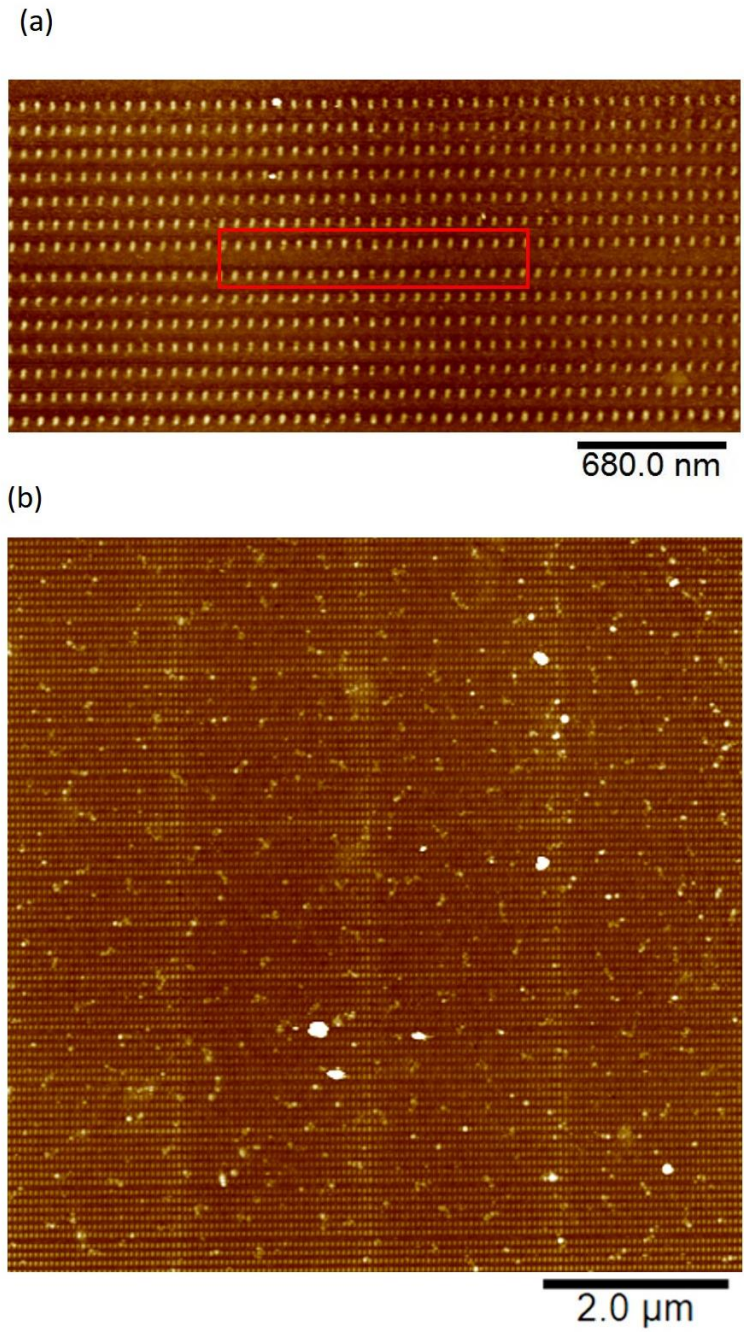

Figure 45: (a) AFM height image of a segment of (b), which reveals a significant jump of the inter-line distance after 7 lines (red frame), which is attributed to the upload of a new set of stream files. (b) 8 x 8 µm² pill array comprising 8800 pills illustrated as an AFM height-image. We can spot periodic irregularities within a horizontal line, which separate the line into four parts. The deviation coincides with the separation of a single line into four segments and can be attributed to favoured precursor coverage of the first pill of a segment. Moreover, irregularities after every seven lines are revealed as changing inter-line distances or as line with taller pills. The bright spots across the unformed bright spots throughout the substrate are foreign particles.

However, by taking a closer look to the deposition in Figure 45 (a), we can spot a jump of the inter-line distance indicated by the red frame. The deviation after seven lines coincides with the upload of new stream files after every seven lines. The upload is necessary since the DBM software cannot store more data to its volatile memory. Hence, the change of the inter-line distance is technically limited by our equipment.

After the successful test depositions, we applied the line-per-line patterning strategy to the aimed 8 x 8 μm^2 array. The deposition of the pill matrix with 8914 pills that are depicted in Figure 45 (b), took around 12 min. Hence, the averaged deposition time per pill is 80 ms. We observed unevenly distributed bright spots, which visualize foreign particles on the surface. Furthermore, there are periodic height irregularities that vertically divide the pattern into four parts according to the separation of the lines into four sections. We have noticed that effect within a single pill in chapter 4.2.1 and accredited the height variation to the favoured precursor replenishment of the first patterning point (first shot effect). In Figure 45 the height differences emanate for similar reasons; only at a higher level. So, the first pill of every section experiences favoured precursor replenishment resulting in a higher vertical growth rate. Moreover, irregularities after every seven lines, which we already spotted in Figure 45 (a) can be also seen in the large-scale pattern. In Figure 45 (b) the uploading of a new set of stream files results not only in a jump of the inner-line distance but also in lines with taller pills. Yet these deviations do not occur in the same periodicity than those induced by the segmentation of each line into four parts.

Although the deviations within the large-scale array are not ideal from a plasmonic point of view, the achievements that lead to the fabrication of the array shown in Figure 45 (b) are highly remarkable from a FEBID point of view. Any optimization of the observed results is technically limited and can be resolved with adapted equipment.

4.2.7 Achievable Feature Size

The key to fully control the shape of FEBID deposits is the awareness of the prevalent working regime, which is determined by the ratio of available precursor molecules for dissociation and the amount of electrons at the patterning spot.[27] Especially for high fidelity structures, as fabricated during this thesis, small changes in the working regime can have significant impact on the deposition behaviour and thus on achievable feature sizes. Since the beam parameters were kept constant throughout the key experiments discussed in previous sections, the parameter of interest was the refresh-time (**RT**) as it strongly influences the precursor coverage and thus the working regime. The RT is the time between two patterning cycles and is linearly proportional to the number of structures deposited during a single cycle. By changing the patterning approach (block array, single line array, and large line array) we also changed the number of structures and consequently the time between two cycles. To make a statement on the working regime, we compared vertical and lateral growth rates, represented by structure heights and widths, respectively, in dependence on the patterning approach. Since the pills showed slight one-sided deviations induced by the stage drift and by the influence of the beam blanker as already discussed in chapter 4.2.4, we measured the unaffected pill side and doubled the value. With this approach, we were able get an insight into the intrinsic deposition behaviour rather than on setup limiting factors. The results are shown in Figure 46 (a), grouped by the above mentioned

experimental conditions (see legend). First important details are the widely homogeneous width values (FWHM) for each experimental block, independent on the achieved heights (see in particular the block array). This in-array width-homogeneity clearly indicates a constant working regime within each array. However, the volume growth rate within the arrays is changing, which is visualised by the varying pill heights, ranging from 12 nm over 14 nm to 16 nm for the different experimental series (see legend). The *changing vertical growth rate at constant lateral growth rate in each block* can be understood as a different operating point within a regime without leaving the regime. This different operation point ultimately depends on the surface coverage which finally affects the achievable feature widths. Hence, we have to correlate FWHM values with the applied RTs for different experiments. The change of the patterning strategy from block arrays (chapter 4.2.5) to single line arrays (chapter 4.2.4) and eventually to large line arrays (chapter 4.2.6) resulted in a reduction of the RT from 8.6 µs to 4.8 µs and finally to 1.8 µs, respectively. Figure 46 (b) now correlates lateral features sizes (FWHM) with the applied RTs, which gives an almost linear decrease with increasing RTs. The main implication of this finding is the non-saturating character for higher RTs, which clearly indicates non-RRL conditions. The trend to broader features for shorter RTs, is in well agreement with the general cross-section evolution in FEBID as depicted in Figure 24.

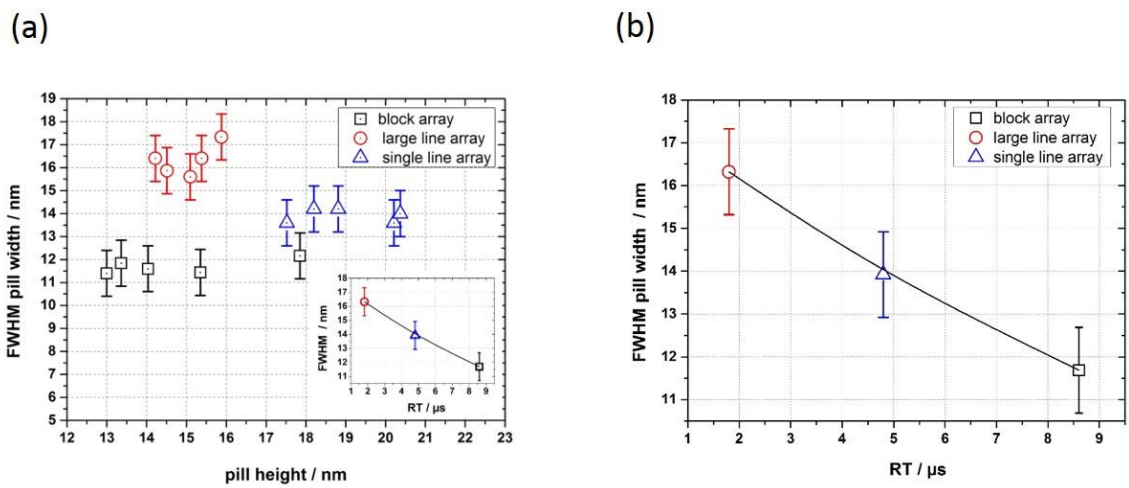

Figure 46: (a) pill widths (FWHM) vs. pill heights for different experimental settings (see legend). Main finding in this graph is the widely homogeneous width distribution for different heights (see in particular black squares). (b) shows a correlation of the averaged pill widths with the applied refresh time RT, which reveals a linear decrease. Particular importance is the non-saturating tendency, which clearly indicates that none of the experiments have been conducted in perfect reaction rate limited regime conditions (see main text).

To interpret, how close the individual settings approach real RRL conditions, two aspects has to be mentioned: ***1)*** the cross-sectional shapes reveal neither flat tops or central indents, which exclude strong MTL regime and DER conditions, respectively. ***2)*** the lateral feature widths within each experimental setting were found very similar, although heights clearly changed (e.g. 13 nm → 18 nm). This suggests that DER conditions have not fully emerged. Hence, we currently assume the operation point of our experiments in DER conditions, very close to the RRL regime. To clarify the situation, further experiments will be done, which in particular include gas flux increase by new geometrical arrangement and / or lower the substrate temperature to increase surface coverage. The main

motivation for these experiments is again the non-linear dependency in Figure 46 (b), which means that lateral feature sizes could go below 10 nm for feature heights > 15 nm.

4.2.8 Pill Array Purification

The requirements for plasmonic resonances is a highly electrical conductive material since the formation of electron oscillations depends on the ease with which an electron can move inside a material. FEBID deposits fabricated from organometallic precursors generally contain very high carbon content of about 90 at. %.[9] The resistivity of the deposits increases with the amount of carbon. Therefore, a post growth purification process is essential to transform the pills into highly pure Au-structures. The purification process was conducted in a QUANTA 200 ESEM (Thermo Scientific Fisher). Firstly, introduced by Geier et al.[10] for platinum-carbon compounds, the purification step was successfully transferred to gold deposits in this institution by Haselmann et al. (see chapter 3.1), where process parameters were elaborated, inherited for the purification of the pill arrays.

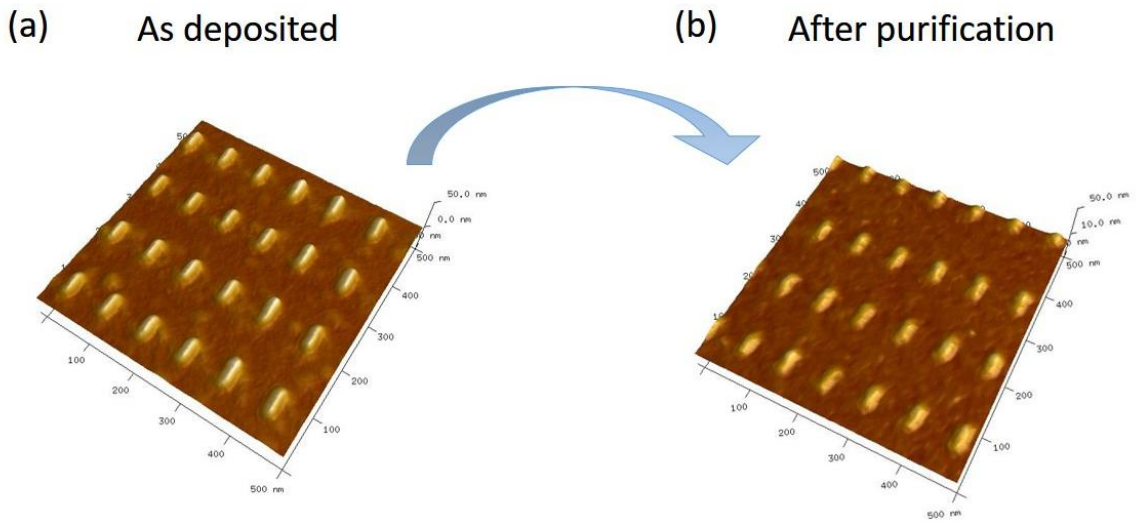

Figure 47: 3D-AFM height image of a pill array in the as deposited state (a) and after purification (b). The crack-free morphology together with the maintained geometry in (b) illustrates the successful application of H_20 post deposition purification to nano-pills. Moreover, height reduction, which comes along with the carbon removal, can be observed by comparing the arrays before and after purification.

The proven and tested parameters include 40 C/cm^2, 5 keV, 5 nA, 1 µs DT at ambient conditions of 10 Pa H_20 on a size of 8 x 8 µm^2. As illustrated in Figure 47 (b) and Figure 48 (a), the purification process resulted in compact and crack free morphology, which is crucial for plasmonic applications.[30] The cross section in Figure 48 (b) reveals the expected height loss of about 60 %, which is a strong indicator for the structure purity; in terms of heights this means a reduction from 15 nm (Figure 44(b)) to 6 nm. Most importantly, the pill shape could be accurately maintained. Considering that simulations in Figure 32 were performed at heights between 5 – 10 nm, the optimized and purified pills are in strong agreement with the requirements. However, as already mentioned in chapter 4.2.4 , the pill geometry did not show completely satisfying results due to the influence of the beam blanker. The aimed bottom width was 25 nm, however this value was already reached at FHWM. Nevertheless, the obtained

outcome of the purification process is highly satisfying since the structure dimensions are in close proximity to the aimed geometry and the pills sustained highly compact.

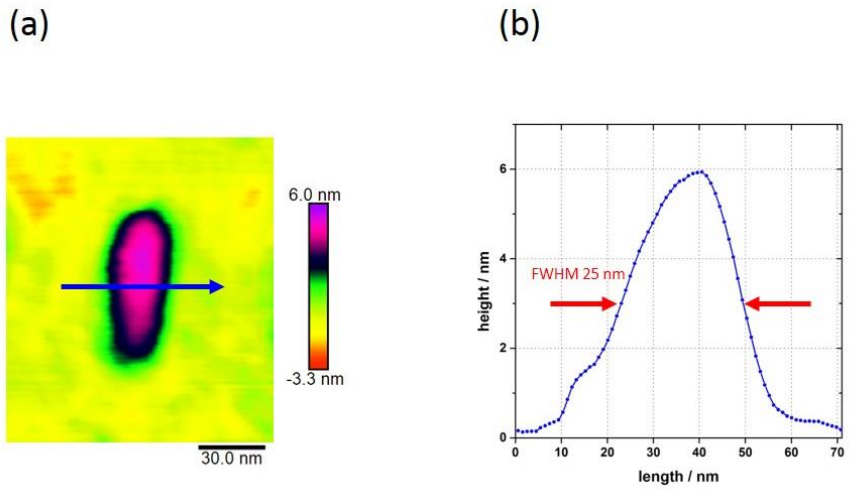

Figure 48: Close-up AFM height image of a single pill after purification (a) confirming the crack-free and highly compact morphology. The cross section (b) along the blue arrow in (a) discloses an FWHM of 25 nm. The height drops to 6 nm, which coincides with the expected drop of 60 % compared to the as-deposited structures.

While the successful nano-synthesis in Figure 47 and Figure 48 (a) were performed on Silicon, the purification step on glass-ITO substrates discloses major deviations of the morphology as seen in Figure 49 (b). The buckling of the ITO layer with height variations up to 60 nm were attributed to delamination of the ITO layer during electron beam exposure during purification. To overcome this issue, different substrates, which are transparent and conductive at the same time can be applied. Consequently, the buckling of the substrate does not fundamentally compromise the FEBID deposition performance and can be confronted with novel substrate solutions.

4.2.9 Plasmonic Response

As the final step, optical measurements via SNOM[55] were conducted by the work group around Prof. Roskos at the Goethe University Frankfurt in order to evaluate the plasmonic response of the large-scale pill arrays. To make a statement on the gold purity, the transmission curves in dependence on the wave length were recorded for as deposited arrays (Figure 49 (a)), for the array after purification (Figure 49 (b)) and for the substrate without structures as a reference measurement. The excitation of the substrate without structures and with as deposited pills do not result in collective plasmon oscillations as visualized by the negligible drop in transmission of the black and red line in Figure 50 (a). The lower transmission of the red line compared the black one might origin from marginal plasmon excitation of the carbon-gold matrices or simply from the additional path of the measurement beam through opaque material. For the incident measurement beam being perpendicular to the substrate, the expected resonance peak of the simulations was between wavelengths of 600 – 700 nm as seen in Figure 32 and as indicated by the blue dotted line in Figure 50 (a).

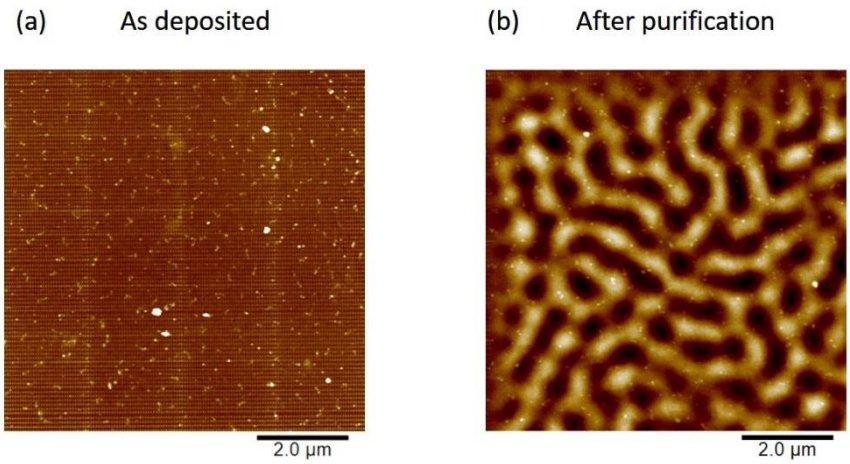

Figure 49: AFM height image showing the delamination of the ITO substrate (b) while being exposed to the electron beam during the purification process. Compared to the as-deposited array (a) the ITO substrate shows height deviation up to 60 nm.

This clearly coincides with the reduced transmission starting from 750 nm downwards to smaller wavelength for the sample with fully purified structures in Figure 50 (a). Contrary to the simulation results, the transmission curve does not show a positive slope while decreasing the testing wavelength from 600 nm to lower values. Moreover, the peak for the fully purified pills was expected to be sharper than the observed one. According to the simulations, the wavelength that excite the collective free electron oscillations are increasing by decreasing pill heights.

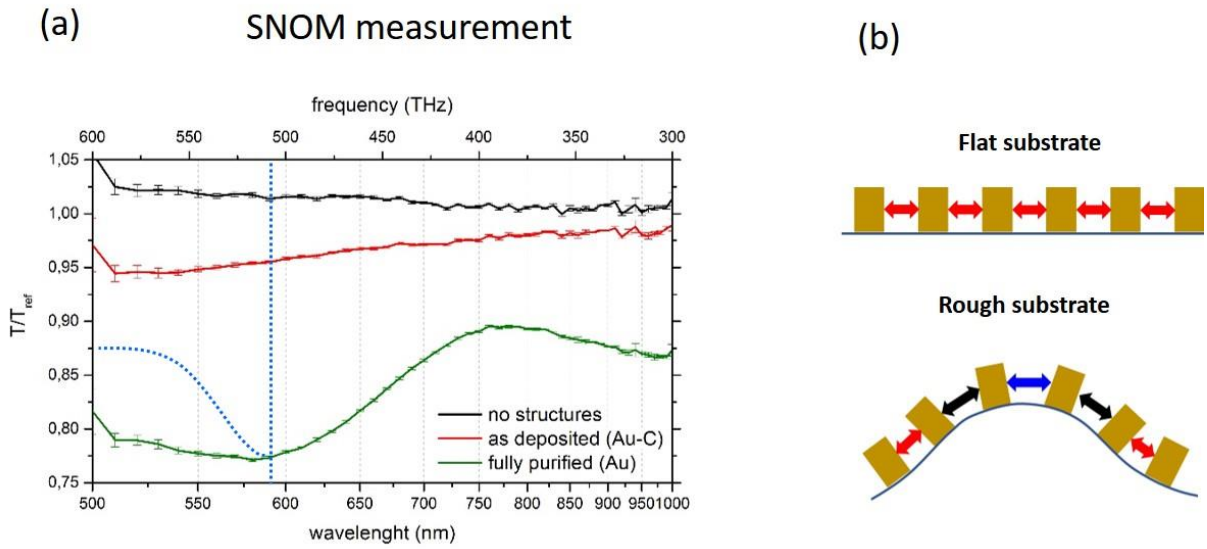

Figure 50: (a) SNOM measurement revealing a distinct drop of the transmission for a fully purified array at wavelengths lower than 750 nm (green line). Compared to the simulation, the resonance peak turned out to be smeared out and less intense. Contrary to the expectations, the transmission of the purified pills is not increasing for wavelength lower than 600 nm. The expected characteristic is illustrated by the blue dotted line. The test samples with as deposited structures (red) and without any deposit (black) do not exhibit a distinct plasmonic excitation. (b) Scheme of the influence of a buckled substrate on the inter-pill distances, which are essential for the plasmonic resonances.

Considering a buckled substrate after purification like in Figure 49 (b) and schematically shown in Figure 50 (b) the path of the incident beam through the pill is constantly changing for pills at different position on the substrate morphology. For the individual excitation of the pills this means that a superposition of the simulation results for different heights is prevalent due to the distorted surface morphology leading to a smeared out peak. Furthermore, the plasmon interaction between the pills strongly contributes to plasmon oscillations as schematically represented by the arrows between the structures in Figure 50 (b). The buckling and also the roughness of the ITO surface induces varying inter-structure distances leading to less pronounced and smeared out resonance peaks.

Moreover, the transmission of the SNOM measurement is significantly higher than the theoretical calculation. As a result of the superposition of changing path lengths through the pills because of the buckled substrate, the number of pills with a particular effective height is lowered, which results in a reduced filtering behaviour. In previous works on plasmonic FEBID structures, Winkler et al. already identified a reduction in peak sharpness and intensity of purified FEBID structures in comparison to identical structures fabricated via electron beam lithography, which coincides with the observed plasmonic behaviour in this study.[30]

Summarizing, the plasmonic activity was exhibited in an expected but also alleviated way. Possible reasons for the unexpected deviations from the underlying simulations are listed below:

- Slightly deformed pill shape induced by the slow charging/discharging behaviour of the beam blanker. As a result of changed pill dimension, the plasmonic excitation is deviated and not fully predictable.

- Lacking precision of stacked pattern due to the necessity to split the pattern in order to minimize the impact of the sample stage drift. First shot effect could be minimized but not entirely removed as it is still evident in multi-arrays. Moreover, the limited data storage of the patterning engine results in marginal shifting of the patterning position after uploading a new set of stream files.

- Substrate buckling due to the delamination of the ITO layer during the purification process causes superposition of effective pill heights for the penetrating light beam and induces changing inter-pill distances, which results in significant peak broadening.

- Different inner grain structure of purified FEBID materials compared to EBL structures might induce deviations from simulations.[30]

- Conductive substrate (glass-ITO) possibly effects the interaction between the plasmon oscillations. The simulation was conducted on a fully insulating substrate representing the optimum constraint for plasmonic resonances.

The crucial insight that can be extracted from the above list, is the fact that deviations from the simulations are mainly originating because of equipment constraints and not from fundamental limitations of FEBID itself. Therefore, we can state at this point that on-demand and direct write fabrication of quasi 2D plasmonic structures with highly challenging dimensions is feasible with FEBID.

5 Summary and Outlook

The motivation for this thesis was to develop a universal blueprint for the deposition of quasi 2D plasmonic structures in the lateral sub-20 nm regime for on-demand direct-write fabrication of novel functional filters on glass fibre. Along the way, we faced several challenges in two previous master theses. The remaining challenge was subject of this thesis and concerned the precursor dynamics in proximity of morphological obstacles, which lead to unwanted variation in spatial expansions. The main approach to overcome these limitations were the application of different patterning strategies for individual single elements as well as for large-scale pill arrays.

During the first part of the thesis, we investigated precursor dynamics inside a morphological cavity. The fabrication inside the cavity was chosen to minimize lateral scattering effects and maximize signal to noise ratios during subsequent optical measurements. By depositing test structures inside the window, we identified a significant increase of vertical growth rates accompanied with a slight but important decrease of the structure widths. This clearly indicates a shift towards the RRL regime, which reflects a boost of the precursor coverage.

In order to further understand this yet barely explored cavity effect, we arranged several test structures with different distances to the border and determined their growth dynamics. The aim was to determine the density gradient of the adsorbed molecules across the patterning area. Hereby, a favoured accumulation in front of the cavity wall that faces the gas flux was spotted, which can be plausibly explained by the reflection of gas molecules at the cavity wall. What is even more striking, however, is the massive precursor gradient around the window corners. A height drop up to 17 % between a pill placed at the corner to a structure 550 nm further away from the corner could be identified. Combining the findings of the strong precursor gradients at the corners with the cavity dimensions, we can assume that the precursor accumulation around morphological obstacles of certain shapes is extraordinary high. By utilizing this effect, intentional deposition of obstacles, which will act as precursor booster, can be considered. This would open the possibility to further control the adsorbate density and hence the FEBID working regime without changing beam parameters or the GIS alignment.

Based on these results, we were able to determine the area with a high precursor gradient. Consecutively we could exclude this area in order to fabricate large-scale pill arrays with a homogenous height distribution. Before depositing the pill arrays, we started with the deposition of single pills in order to gain fundamental understanding of the growth dynamics of exceedingly small structures. However, by depositing the pills individually, the refresh time was too short for providing sufficient number of molecules around the patterning spot to work in the RRL regime. Therefore, we introduced the deposition of numerous structures in line arrays during one patterning cycle, which is accompanied with an increase of the refreshtime by the number of structures. Although we approached RRL conditions by this approach, it also caused residual depositions in between the pills, which we could trace back to the limited beam movement capabilities of the used instrumentation. To counteract the highly unwanted residues, we installed a beam blanker, which could significantly reduce the height of the co-deposit with the drawback of slight pill deformation due to rest deflection of the beam blanker. By neglecting the one-sided widening of the pill, which was exclusively induced due to technical limitations of our setup, we observed drift-corrected pill dimensions with an astonishing FWHM of

14 nm at a height of 21 nm. This results in an aspect ratio of 0.7, which represent a worldwide benchmark in the FEBID community.

Eventually, the pills were arranged in large-scale arrays to achieve the objective of filtering parts of the optical wavelength by collectively exciting the plasmon oscillations of the whole array. In order to minimize the influence of the prevalent stage drift of our DBM system, the duration of one patterning cycle had to be minimized. But at the same time, it was necessary to provide a sufficient precursor coverage, which can be increased with longer loop times. Thus, the 8 x 8 μm^2 pattern was split into smaller arrays with optimized dimensions to meet the conflicting requirements. By placing the structures into rectangular arrays, we noticed a significant height drop of 35 % from the very outer to the inner deposits. Although shadowing effects are widely known, the tremendous impact of neighbouring structures with heights in the range of 20 nm, were much unexpected. We assume that not only morphological hindrances are responsible for the reduced diffusion. Rather it is very likely that the diffusion length of the precursor molecules changes drastically on the deposited material and on the substrate. Consequently, this causes a distinct precursor coverage gradient throughout the rectangular pattern.

Since the precursor dynamics are highly sensitive, it turned out to be inevitable to avoid any hindrances for the diffusing precursor molecules while fabricating the pill array. This goal was met by introducing a line per line patterning strategy resulting in remarkable in-field height variations of ± 2 %. Nevertheless, small deviations from the desired pattern homogeneity could not be avoided due to the necessary splitting into single lines. However, from a FEBID point of view the fabrication of an array including 8800 pills with a remarkable constant height distribution, represents a major achievement towards quasi 2D plasmonic applications.

From a fundamental point of view, the correlation between the vertical and lateral growth rate in dependence of the refreshtime revealed crucial insights into the FEBID deposition behaviour. By increasing the refreshtime, a distinct trend towards thinner structure and hence towards the RRL regime was observed which brought us a significant step closer to determine the intrinsic resolution limit of FEBID.

After successfully transferring the deposits into highly pure and compact Au-structures, the plasmonic resonances were successfully verified. Yet, the sharpness and intensity of the resonances was less pronounced than predicted by the simulations. On the one hand, the plasmonic deviations can be attributed to the pill fabrication, namely the slightly distorted pill shape and the minor inhomogeneity across the pattern. On the other hand, the purification process provoked a delamination of the ITO layer causing a buckled substrate surface that potentially effects the optical validation in a sever manner. Nevertheless, these irregularities are generated by technical limitations and can be solved by a fully stabilized sample stage and improved substrates.

Overall, this thesis presents a major step towards fully understanding complex precursor dynamics. The strong accumulation in the proximity of morphological obstacles could be utilized by introducing precursor booster in order to actively control the FEBID working regime without changing beam parameters. Furthermore, a blueprint for fabricating large-scale arrays of structures with exceedingly small dimension was developed, which opens the door to apply FEBID for novel optical applications.

References

1. Pors, A., Nielsen, M. G. & Bozhevolnyi, S. I. Analog computing using reflective plasmonic metasurfaces. *Nano Lett.* **15,** 791–797 (2015).

2. Chizari, A., Abdollahramezani, S., Jamali, M. V. & Salehi, J. A. Analog optical computing based on a dielectric meta-reflect array. *Opt. Lett.* **41,** 3451 (2016).

3. Zhu, T. *et al.* Plasmonic computing of spatial differentiation. *Nat. Commun.* **8,** (2017).

4. Schuller, J. A. *et al.* Plasmonics for extreme light concentration and manipulation. *Nature Materials* **9,** 193–204 (2010).

5. Fang, N., Lee, H., Sun, C. & Zhang, X. Sub-Diffraction-Limited Optical Imaging with a Silver Superlens. *Science (80-.).* **308,** 534 LP-537 (2005).

6. Pendry, J. B., Schurig, D. & Smith, D. R. Controlling electromagnetic fields. *Science (80-.).* **312,** 1780–1782 (2006).

7. Dieing, T., Hollricher, O. & Toporski, J. *Confocal Raman Microscopy*. *Confocal Raman Microscopy* **158,** (2010).

8. van Dorp, W. F. Sub-10 nm writing: focused electron beam-induced deposition in perspective. *Appl. Phys. A Mater. Sci. Process.* **117,** 1615–1622 (2014).

9. Botman, A., Mulders, J. J. L., Weemaes, R. & Mentink, S. Purification of platinum and gold structures after electron-beam-induced deposition. *Nanotechnology* **17,** 3779–3785 (2006).

10. Geier, B. *et al.* Rapid and highly compact purification for focused electron beam induced deposits: A low temperature approach using electron stimulated H2O reactions. *J. Phys. Chem. C* **118,** 14009–14016 (2014).

11. Winkler, R. *et al.* Direct-Write 3D Nanoprinting of Plasmonic Structures. *ACS Appl. Mater. Interfaces* **9,** 8233–8240 (2017).

12. Giannuzzi, L. A. & Stevie, F. A. *Introduction to focused ion beams: Instrumentation, theory, techniques and practice*. *Introduction to Focused Ion Beams: Instrumentation, Theory, Techniques and Practice* (2005). doi:10.1007/b101190

13. Giannuzzi, L. A. & Stevie, F. A. A review of focused ion beam milling techniques for TEM specimen preparation. *Micron* **30,** 197–204 (1999).

14. Goldstein, J. *et al. Scanning Electron Microscopy and X-ray Microanalysis*. *Scanning Electron Microscopy and Xray Microanalysis* **44,** (2003).

15. Winkler, R. Courtesy of Dr.Robert Winkler, Institute for Electron Microscopy and Nanoanalysis, Graz University of Technology, Austria, 2018. (2018).

16. Flegler, Heckmann & Klomparens. *Elektronenmikroskopie: Grundlagen. Methoden. Anwendungen*. (Spektrum, 1995).

17. Plank, H. Courtesy of Ass.Prof. Dr. Harald Plank, Institute for Electron Microscopy and Nanoanalysis, Graz University of Technology, Austria, 2017.

18. Hecht, E. Optics 4th edition. *Optics 4th edition by Eugene Hecht Reading MA AddisonWesley*

Publishing Company 2001 **1,** 122 (2001).

19. L., R. & G., P. *Rasterelektronenmikroskopie*. (1977).

20. Satoh, H., Kawata, S., Nakane, H. & Adachi, H. Studies on the ZrO/W(100) surface by means of low-energy electron diffraction and X-ray photoelectron spectroscopy. *Surf. Sci.* (1998). doi:10.1016/S0039-6028(97)00896-0

21. Stokes, D. J. *Principles and Practice of Variable Pressure/Environmental Scanning Electron Microscopy (VP-ESEM)*. *Principles and Practice of Variable Pressure/Environmental Scanning Electron Microscopy (VP-ESEM)* (2008). doi:10.1002/9780470758731

22. AR., C., D., D. & R., G. CASINO V2.5.1. Monte Carlo simulation of electron trajectories in solids. (2017).

23. Chambost, E. de. Détecteur Everhart-Thornley. (2007). Available at: Wikimedia commons.

24. Huth, M. *et al.* Focused electron beam induced deposition: A perspective. *Beilstein Journal of Nanotechnology* **3,** 597–619 (2012).

25. Utke, I., Hoffmann, P. & Melngailis, J. Gas-assisted focused electron beam and ion beam processing and fabrication. *J. Vac. Sci. Technol. B Microelectron. Nanom. Struct.* **26,** 1197 (2008).

26. Botman, A., Mulders, J. J. L. & Hagen, C. W. Creating pure nanostructures from electron-beam-induced deposition using purification techniques: A technology perspective. *Nanotechnology* **20,** (2009).

27. Utke, I., Moshkalev, S. & Russell, P. Nanofabrication Using Focused Ion and Electron Beams: Principles and Applications. *Oxford Univ. Press* 410–435 (2012).

28. Van Dorp, W. F. & Hagen, C. W. A critical literature review of focused electron beam induced deposition. *J. Appl. Phys.* **104,** (2008).

29. LookChem. Available at: http://www.lookchem.com/cas-149/14951-50-9.html. (Accessed: 5th April 2018)

30. Winkler, R. *et al.* Direct-Write 3D-Nanoprinting of Plasmonic Structures. *ACS Appl. Mater. Interfaces* acsami.6b13062 (2016). doi:10.1021/acsami.6b13062

31. Engmann, S. *et al.* Absolute cross sections for dissociative electron attachment and dissociative ionization of cobalt tricarbonyl nitrosyl in the energy range from 0 eV to 140 eV. *J. Chem. Phys.* **138,** (2013).

32. Plank, H., Gspan, C., Dienstleder, M., Kothleitner, G. & Hofer, F. The influence of beam defocus on volume growth rates for electron beam induced platinum deposition. *Nanotechnology* **19,** (2008).

33. Lobo, C. J., Toth, M., Wagner, R., Thiel, B. L. & Lysaght, M. High resolution radially symmetric nanostructures from simultaneous electron beam induced etching and deposition. *Nanotechnology* **19,** (2008).

34. Utke, I., Friedli, V., Purrucker, M. & Michler, J. Resolution in focused electron- and ion-beam induced processing. *J. Vac. Sci. Technol. B Microelectron. Nanom. Struct.* **25,** 2219–2223 (2007).

35. Szkudlarek, A., Szmyt, W., Kapusta, C. & Utke, I. Lateral resolution in focused electron beam-induced deposition: scaling laws for pulsed and static exposure. *Appl. Phys. A Mater. Sci. Process.* **117,** 1715–1726 (2014).

36. Plank, H., Haber, T., Gspan, C., Kothleitner, G. & Hofer, F. Chemical tuning of PtC nanostructures fabricated via focused electron beam induced deposition. *Nanotechnology* **24,** (2013).

37. Plank, H., Smith, D. A., Haber, T., Rack, P. D. & Hofer, F. Fundamental proximity effects in focused electron beam induced deposition. *ACS Nano* **6,** 286–294 (2012).

38. Utke, I. *et al.* Focused electron beam induced deposition of gold. *J. Vac. Sci. Technol. B Microelectron. Nanom. Struct.* **18,** 3168 (2000).

39. Córdoba, R., Sharma, N., Kölling, S., Koenraad, P. M. & Koopmans, B. High-purity 3D nano-objects grown by focused-electron-beam induced deposition. *Nanotechnology* **27,** (2016).

40. Folch, A., Tejada, J., H. Peters, C. & Wrighton, M. *Electron beam deposition of gold nanostructures in a reactive environment*. *Applied Physics Letters* **66,** (1995).

41. Warneke, Z., Rohdenburg, M., Warneke, J., Kopyra, J. & Swiderek, P. Electron-driven and thermal chemistry during water-assisted purification of platinum nanomaterials generated by electron beam induced deposition. *Beilstein J. Nanotechnol.* **9,** 77–90 (2018).

42. Murray, W. A. & Barnes, W. L. Plasmonic materials. *Advanced Materials* **19,** 3771–3782 (2007).

43. Nehl, C. L., Liao, H. & Hafner, J. H. Optical properties of star-shaped gold nanoparticles. *Nano Lett.* **6,** 683–688 (2006).

44. Shumaker-Parry, J. S., Rochholz, H. & Kreiter, M. Fabrication of crescent-shaped optical antennas. *Adv. Mater.* **17,** 2131–2134 (2005).

45. Hammond, J. L., Bhalla, N., Rafiee, S. D. & Estrela, P. Localized surface plasmon resonance as a biosensing platform for developing countries. *Biosensors* **4,** 172–188 (2014).

46. Giessibl, F. J. AFM's path to atomic resolution. *Mater. Today* **8,** 32–41 (2005).

47. Bhushan, B. Handbook of Nanotechnology. in *Handbook of Nanotechnology* 278 (2010). doi:10.1007/3-540-29838-X

48. Fröch, J. Mechanical Properties of Free-Standing 3D Nanostructures Fabricated via Focused Electron Beam Induced Deposition. (2017).

49. Moreno-Herrero, F., Colchero, J., Gómez-Herrero, J. & Baro, A. M. Atomic force microscopy contact, tapping, and jumping modes for imaging biological samples in liquids. *Phys. Rev. E - Stat. Nonlinear, Soft Matter Phys.* **69,** (2004).

50. Binnig, G. Atomic force microscope and method for imaging surfaces with atomic resolution. *US Pat. 4,724,318* 1–8 (1988).

51. Haselmann, U. Direct-Write Fabrication of Pure Metal Structures for nano-probing and Plasmonic Applications. *Master thesis* (2016).

52. Radeschnig, U. Approaching Fundamental Resolution Limits during Focused Electron Beam

Induced Gold Deposition on Bulk Substrate. (2017).

53. Arnold, G. *et al.* Fundamental resolution limits during electron-induced direct-write synthesis. *ACS Appl. Mater. Interfaces* **6,** 7380–7387 (2014).

54. Winkler, R. Implication of Precursor Dynamics during Foused Electron Beam Induced Deposition. (Graz University of Technology, 2013).

55. Courjon, D. & Bainier, C. Near field microscopy and near field optics. *Reports on Progress in Physics* **57,** 989–1028 (1994).

56. van Oven, J. C., Berwald, F., Berggren, K. K., Kruit, P. & Hagen, C. W. Electron-beam-induced deposition of 3-nm-half-pitch patterns on bulk Si. *J. Vac. Sci. Technol. B, Nanotechnol. Microelectron. Mater. Process. Meas. Phenom.* **29,** 06F305 (2011).

57. Winkler, R. Implications of Precursor Dynamics on Nanostructures during Focused Electron Beam Induced Deposition. (2013).

58. X, D. & Fernández-Pacheco, A. Modelling focused electron beam induced deposition beyond Langmuir adsorption. *Beilstein J. Nanotechnol.* **8,** 2151–2161 (2017).

59. Friedli, V. & Utke, I. Optimized molecule supply from nozzle-based gas injection systems for focused electron- and ion-beam induced deposition and etching: Simulation and experiment. *J. Phys. D. Appl. Phys.* **42,** (2009).

60. Friedli, V. & Utke, I. http://www.empa.ch/GISsimulator.

61. You, E. A., Zhou, W., Suh, J. Y., Huntington, M. D. & Odom, T. W. Polarization-dependent multipolar plasmon resonances in anisotropic multiscale au particles. *ACS Nano* **6,** 1786–1794 (2012).

62. Winkler, R. *et al.* The Nanoscale Implications of a Molecular Gas Beam during Electron Beam Induced Deposition. *ACS Appl. Mater. Interfaces* **6,** 2987–2995 (2014).